MATTER AND DYNAMICS OF THE LOCAL VOLUME THROUGH TIP OF THE RED GIANT BRANCH DISTANCES

A DISSERTATION SUBMITTED TO THE GRADUATE DIVISION OF THE UNIVERSITY OF HAWAIʻI AT MĀNOA IN PARTIAL FULFILLMENT OF THE REQUIREMENTS FOR THE DEGREE OF

DOCTOR OF PHILOSOPHY

IN

ASTRONOMY

December 2012

By
Bradley A. Jacobs

Dissertation Committee:

R. Brent Tully, Chairperson
Fabio Bresolin
Rolf-Peter Kudritzki
John G. Learned
Michael C. Liu

© Copyright 2012
by
Bradley A. Jacobs
All Rights Reserved

Acknowledgements

Thanks foremost to my parents for their constant support and encouragement. I benefited from the insights and assistance from a number of people over the course of this project. In addition to my advisor Brent Tully and my dissertation committee, I collaborated closely with Luca Rizzi, Edward Shaya, and Kristin Chiboucas. Support for this project has come from Hubble Space Telescope Programs: AR-11285, GO-11584, and SNAP-12546.

Abstract

Studies at high redshift leverage look-back time to probe the history of the universe. These are complemented by detailed examinations of nearby objects and the clues they reveal about their past. The Hubble Space Telescope (HST) has opened the Local Volume (within 10 Mpc) to studies of resolved stellar populations, and a significant fraction of these $\sim 10^3$ local galaxies have been observed with either the Wide-Field Planetary Camera 2 or the Advanced Camera for Surveys. The observations reveal information about the galaxies' star formation histories as well as their distances, which are key to understanding their past interactions with other galaxies. Using a combination of searches of the HST archive and observations from my collaborators' programs, I have identified and run photometry on $\sim$300 local galaxies. The criteria for a set of observations' inclusion in the sample are that they are of sufficient depth and are taken in filters appropriate for measuring an accurate distance based on the Tip of the Red Giant Branch method. Color-magnitude diagrams and distance estimates from these observations are published online. I use these distances, along with spectroscopic radial velocities, in a numerical application of the Principle of Least Action to develop scenarios representing the galaxies' motion from early times, and use these scenarios to constrain the mass of the M81 group. The results suggest that the group may contain more dark matter than has been previously inferred. Next, in pursuing the other thread of the galaxies' histories, I synthesize the color-magnitude diagram of the nearby dwarf irregular UGC4879 to estimate its star formation rate over time, finding both young and ancient stars but no evidence for ones of intermediate age. Building upon the study of UGC4879, I examine the stellar content of $\sim$90 dwarf galaxies from the sample by focusing on the relative numbers and colors of the red and asymptotic giants observed in their diagrams. These tests show excellent discrimination by morphological type, as well as hint at intriguing trends in star formation and enrichment that merit further investigation.

Table of Contents

Acknowledgements iii

Abstract iv

List of Tables vii

List of Figures viii

Chapter 1: Introduction 1

1.1 Structure of Dissertation 4

Chapter 2: The Extragalactic Distance Database: Color–Magnitude Diagrams 8

2.1 Introduction 8

2.2 Data 9

2.3 CMDs/TRGB Catalog 10

2.4 Footprint Images 10

2.5 Observation Images 11

2.6 Analysis 12

2.7 Color-Magnitude Diagrams 12

2.8 TRGB Distances 13

Chapter 3: Numerical Action Analysis of the M81 Group of Galaxies 24

3.1 Introduction 24

3.2 Data 26

3.2.1 TRGB Distances 26

3.2.2 Radial Velocities 27

3.2.3 Luminosities 28

3.2.4 Morphology 28

3.2.5 Catalog 28

3.3 NAM . . . 29
3.4 Application of NAM . . . 31
3.4.1 Goodness of Fit . . . 32
3.4.2 Iterative Search of M/L Ratios . . . 35
3.5 M81 Group . . . 37
3.5.1 Masses . . . 37
3.5.2 Orbital History . . . 40
3.6 Summary and Conclusion . . . 43
Chapter 4: The Star Formation History of Isolated Dwarf UGC4879 . . . 57
4.1 Introduction . . . 57
4.2 ACS Data and Photometry . . . 58
4.3 TRGB Distance . . . 59
4.4 Metallicity . . . 59
4.5 Star Formation History . . . 60
4.5.1 CMD Regions . . . 61
4.5.2 Chemical Evolution History . . . 62
4.5.3 Spatially Resolved Star Formation . . . 63
4.6 Discussion . . . 64
4.6.1 Stellar Ages > 1 Gyr . . . 64
4.6.2 Stellar Ages < 1 Gyr . . . 66
4.6.3 UGC4879 In Context . . . 66
Chapter 5: Rough Estimates of Stellar Histories of Dwarfs from HST Photometry of the Red and Asymptotic Giant Branches . . . 81
5.1 Introduction . . . 81
5.2 Model Predictions . . . 82
5.2.1 Metallicity . . . 83
5.3 Measurements . . . 84
5.3.1 AGB and RGB counts . . . 84
5.3.2 Photometric Metallicities . . . 85
5.3.3 Luminosity and Morphology . . . 86
5.4 Analysis . . . 86

5.4.1 Luminosity Cut . . . 86
5.4.2 AGB/RGB Ratio versus RGB Color . . . 87
5.4.3 Errors in AGB/RGB Ratio . . . 87
5.5 Discussion . . . 88
Chapter 6: Discussion and Summary . . . 108
Appendix: TRGB Measurement and Publication Procedures . . . 113
A.1 Introduction . . . 113
A.2 Identifying and Obtaining HST Images . . . 113
A.2.1 File Extensions . . . 114
A.3 Photometry . . . 114
A.3.1 Preprocessing . . . 114
A.3.2 WFPC2 . . . 115
A.3.3 ACS . . . 117
A.4 Identifying the TRGB . . . 120
A.4.1 Configuring TRGBTOOL . . . 121
A.4.2 Running TRGBTOOL . . . 122
A.4.3 Spatial Masking to Identify the TRGB . . . 124
A.5 Measuring a TRGB Distance . . . 124
A.5.1 Reddening Estimates from Main Sequence . . . 126
A.6 Presenting Resulting Distances . . . 126
A.6.1 The Database File . . . 127
A.6.2 The Galaxy Webpages . . . 128

List of Tables

2.1 CMD/TRGB Database (Left) 17
2.2 CMD/TRGB Database (Right) 18
3.1 Background M/L Ratio Search 48
4.1 Star Formation Rates 70
5.1 Properties of Dwarf Galaxies 94
5.1 Properties of Dwarf Galaxies 95
5.1 Properties of Dwarf Galaxies 96
5.1 Properties of Dwarf Galaxies 97
A.1 TRGB Table Columns 128

List of Figures

2.1 HST footprints of NGC4163 and IC4662 19

2.2 Pseudo-color images of NGC4163 and IC4662 20

2.3 CMDs of NGC4163 and IC4662 21

2.4 Luminosity function and fits to the CMDs of NGC4163 and IC4662 22

2.5 Zoomed CMD of IC4662 23

3.1 Distribution of galaxies within 4.5 Mpc 49

3.2 Median ΔV vs. M/L; galaxies with $L_K > 10^{10}$ $L_\odot$; $\Omega_{\rm Smooth} = 0$ 50

3.3 Median ΔV vs. M/L; 17 test galaxies; $\Omega_{\rm Smooth} = 0$. 51

3.4 Median ΔV vs. M/L; 17 test galaxies; $\Omega_{\rm Smooth}$ adjusted 52

3.5 RMS(ΔV) vs. M/L; 17 test galaxies 53

3.6 Median ΔV vs. $M/L_{\rm M81M82}$; 8 tracers of M81 group mass 54

3.7 Example orbital paths of 8 tracers of M81 group mass 55

3.8 RMS(ΔV) vs. $M/L_{\rm M81M82}$; 8 tracers of M81 group mass 56

4.1 Psuedo-color image of UGC4879 70

4.2 CMD of UGC4879 71

4.3 Distribution of galaxies in and around Local Group 72

4.4 RGB of UGC4879 73

4.5 CMD regions used in comparison with simulated stars 74

4.6 Young simulated stars at given metallicity 75

4.7 Chemical evolution history of UGC4879 76

4.8 Star formation history of UGC4879 76

4.9 Comparison between observed and simulated CMDs 77

4.10 Spatial distribution of detected stars 77
4.11 Observed and simulated CMDs from inner region of UGC4879 78
4.12 Observed and simulated CMDs from outer region of UGC4879 78
4.13 Star formation history of inner region 79
4.14 Star formation history of outer region 79
4.15 Ratio of AGB to RGB for observed and simulated stars 80

5.1 Ratio of simulated AGB to RGB stars 98
5.2 CMDs of simulated stars at given metallicity 99
5.3 CMD of UGC8651 100
5.4 RGB of UGC8651 101
5.5 K_s-band luminosity vs. photometric metallicity 102
5.6 AGB/RGB ratio vs. photometric metallicity 103
5.7 CMD of F8D1 104
5.8 CMD of ESO269-37 105
5.9 CMD of KK197 106
5.10 CMD of UGC5336 107

Chapter 1

Introduction

Distances measurements add depth to our otherwise two-dimensional picture of the Universe. Without distances, luminosity and apparent brightness are degenerate, as are physical size and angular extent. This degeneracy must be broken in order to study the physical properties of the observed objects, a fact that has been known for hundreds of years. The earliest successful efforts to measure physical distances at astronomical scales involved measuring trigonometric parallaxes, with the foundation set by the parallax of Venus. Venus has a parallax of $\sim$1 arcmin for observers separated by baseline of 10^4 km. A number of factors, including the fact that this distance changes over the course of an orbit, complicate the measurement, so until fairly recently it was only possible to measure the parallax of Venus under special circumstances. These circumstances occurred recently in 2012, when Venus transited the Sun. The first parallaxes of Venus were measured in the pair of transits in 1761 and 1769, and refined with the transits in 1874 and 1882. Kepler's Laws allow extrapolation of the distance to Venus to the other distances of the Solar System, crucially the distance from the Earth to the Sun. The distances to any object beyond the Solar System are too great to be accessible to a parallax measurement that uses the diameter of the Earth as a baseline. However, Earth's motion around the Sun provides a dramatically longer baseline for measurements. Observations separated by six months (for a baseline of 2 AU), still require much more precise angular measurements than were required for the Venus observations, so stepping beyond the Solar System remained a challenge. It was not until 1838 that Friedrich Wilhelm Bessel measured a stellar parallax. He announced that 61 Cygni had a parallax of 0.3136 ± 0.0202 arcsec, and converted this to 657,700 AU or 10.3 ly (Bessel 1838). The modern value of the parallax is just outside Bessel's quoted error at 0.2868 arcsec (van Leeuwen 2007).

Geometric parallaxes remain a valuable source of distance information, and the number of objects with measured parallaxes is set to significantly increase with the launch of the Gaia satellite in 2013. However, the technique will be infeasible for megaparsec scales for the foreseeable future, though geometric distance measurements can be made in some rare cases, such as by following water masers motion around the active galactic nucleus in NGC4258 (Herrnstein et al. 1999). Most other distance measures depend on observing stars in a particular evolutionary phase, where knowledge of the physical processes occurring during the chosen stage permits an estimate of the star's luminosity. A luminosity estimate combined with an observation of apparent brightness yields a distance estimate. However, these luminosity estimates must be determined empirically through comparison with previously established distance estimates. The historic steps in this process, often referred to as the cosmic distance ladder, involved stepping from the parallax of Venus, to stellar parallaxes, to Cepheid variable stars. These stars are named after the prototype δ Cepheii, which was discovered to be variable in 1784. In 1912 Henrietta S. Leavitt determined that the pulsation period of the variables increases with luminosity (Leavitt & Pickering 1912), based on observations of 25 Cepheids in the Small Magellanic Cloud (and thus located at the same distance to reasonable approximation), taken from a catalog she built of more than one thousand variable stars (Leavitt 1908). Competing explanations for the observed variability were proposed, and Harlow Shapley argued that Cepheids are variable due to stellar pulsation (Shapley 1914), and later measured the distances to Cepheids located in several globular clusters (Shapley 1918). Many key astronomical discoveries are based on observations of Cepheids, and a vast amount of research benefits from the insights that came from their observation. Foremost among these are Edwin Hubble's observations of Cepheids in Andromeda, which established that it located outside the Milky Way (Hubble 1925), i.e., more distant than Shapley's globular clusters. Cepheids in this and other galaxies, when combined with spectroscopic radial velocities, revealed that galaxies' recession rate increases with distance (Hubble 1929).

Despite the innumerable advances that depend on observations of Cepheid variables made over the last century, other stars hold some advantages over Cepheids as standard candles. The predictable variability of Cepheids that is the source of their value as distance indicators is also a drawback for observational campaigns. Many observations of the same stars are needed in order to precisely measure the period of variability in order to determine their luminosity and distance. Moreover, stars in this phase of evolution are massive, and therefore have short lifetimes so they are

only found in environments where star formation has been relatively recent. A significant number of local galaxies stopped forming stars long enough ago that they contain no Cepheids. There are other variable stars, such as RR Lyraes that are longer-lived and useful for distance measurements, but the challenge of repeated monitoring (and in this case to fainter magnitudes) remains. Fortunately, other stars are available as standard candles that need only be observed once and are found in nearly all galaxies. These are the most luminous Red Giants. Red Giants fuse H into He in a shell around a degenerate core of He. This degeneracy is the key to the brightest Red Giants suitability as standard candles. As more He falls onto the core, the core temperature rises, but unlike non-degenerate matter that is supported by thermal pressure, it does not expand and cool. The increasing mass in the core also increases the rate of fusion in the shell surrounding it, and as a result the luminosity of a Red Giant increases as it evolves through this phase. Eventually, the degenerate core will reach temperatures of around 10^8 K, which is sufficient for He to fuse into C (Deupree & Wallace 1987), and this quickly breaks the degeneracy of the core and then lets the star settle into a He-burning phase on the Horizontal Branch. This rapid breaking of degeneracy places a sharp upper-limit on the luminosity of Red Giants, since it is regulated by the mass of the degenerate core.

The Tip of the Red Giant Branch (TRGB) method for measuring distances depends on precisely measuring the apparent brightness of many Red Giants because only the brightest ones serve as standard candles and they must be identified *before* the onset of He burning alters their luminosity and color. This technique differs from earlier methods for measuring distances in that earlier methods require detailed and usually repeated observations of individual stars, whereas the TRGB method arrives at a distance from the collective measurement of a large number of Red Giants (generally at least 100). Furthermore, a star can only be identified as a Red Giant through comparison with other stars in its galaxy in terms of both luminosity and color. Hence, each star in an image must be photometered and this process must be repeated with another image of the field taken through a different filter. This labor intensive process with photographic plates has yielded distance estimates to nearby galaxies dating from at least 1982 (Graham 1982). But the continued application of the TRGB method really depends on the use of automated measurements made possible through Charge Coupled Devices (CCDs), and that same year Hoessel & Mould (1982) published color-magnitude diagrams (CMDs) for the Pegasus Dwarf Irregular galaxy using CCD observations that included an identification of the TRGB. A decade later, following several more papers that included a TRGB measurement for a single galaxy, Lee et al. (1993) published a systematic study comparing distances

based on the TRGB with Cepheid and RR Lyrae measurements for 10 galaxies. This established it as reliable distance indicator.

CCD observations made TRGB distance measurements feasible for several local galaxies, but the smearing effects of the atmosphere generally limit ground-based measurements to galaxies within 2-3 Mpc (Mendez et al. 2002). Wider application of the method requires another technological advancement beyond CCDs: the Hubble Space Telescope (HST). The fine resolution available from space-based observations allow TRGB measurements from a single orbit of observations at distances up to 10 Mpc. Around a thousand galaxies are located in this the Local Volume, and it is the desire to map their locations that serves as the primary motivation for this dissertation.

1.1 Structure of Dissertation

Observations of nearby galaxies with HST that were suitable for TRGB measurements began in 1994 after the installation of the Wide-Field Planetary Camera 2 (WFPC2). A single orbit of observations in two filters with WFPC2 reaches $F814W \approx 25$ (in the HST version of I-band), which is sufficient to identify the TRGB at distances less than $\sim$4.5 Mpc. The installation of the Advanced Camera for Surveys (ACS) in 2002 expanded that capability to 10 Mpc. Between WFPC2 and ACS around 300 galaxies in the Local Volume have been observed to-date (using the filters necessary for a TRGB measurement). All HST observations become publicly available within a year of when they were taken. The first part of this dissertation project involved performing photometry to generate CMDs, using these to measure TRGB distances, and building a database to house these products for each of the local galaxies observed with HST. A description of the methods used to make these measurements, along with details of the contents of the publicly available database that houses them is given in Chapter 2. The chapters that follow all make use of these products in different ways. In addition to Chapter 2, the procedures used in the process: from obtaining images from the HST Archive through to publication of a CMD and TRGB distance in the database are described in Appendix A.

Over the years that HST has been in orbit observations of nearby galaxies have occupied a significant fraction of its time, and as the fraction grew a series of Snapshot surveys with WFPC2 were designed to fill in the gaps to cover all known galaxies within roughly 4 Mpc. This distance limit is set by the depth achieved by WFPC2 in two filter observations taken during a single orbit. All the galaxies in the Catalog of Neighboring Galaxies (Karachentsev et al. 2004) that have velocities that

are consistent with a distance around 4 Mpc or less have been observed with WFPC2 and/or ACS. It turns out that some of these galaxies have securely measured distances between 4 and 4.5 Mpc, so in fact the volume-limited sample is complete to 4.5 Mpc. This completeness is important for studies of galaxies' dynamics. Our first goal in analyzing the sample is to use the three-dimensional positions made available from consistently measured TRGB distances to reconstruct the paths of the galaxies that lead to the galaxies' current locations. If the galaxies' motions relative to one another were small at early times then it is possible to build possible orbital paths based on the Principle of Least Action. These depend on the masses of the galaxies, which we can estimate based on their luminosity. The relation between luminosity and mass can be constrained by observing the galaxies' current velocities with respect to the Milky Way and comparing these with the radial velocities predicted by the simulations. This process of relaxing galaxy orbital paths by minimizing their action and comparing the results with current velocities and/or positions is known as the Numerical Action Method (NAM). In Chapter 3 I estimate a general mass-to-light ratio for galaxies in a catalog where positions are determined through TRGB distances to the extent that is possible. Then using this mass ratio I adjust the mass of the M81 group and use differences between observed and simulated velocities of galaxies that are sensitive to the mass of this group in an attempt to develop a detailed constraint on the mass of the group. NAM studies of the Local Group are also ongoing (P.I. Edward Shaya), and M81 is the next logical target as the next nearest unobscured group of galaxies.

To this point my research has made use of only one piece of information from each galaxy, its distance, but this ignores a wealth of detail about the galaxy available from its CMD. The RGB is one of many phases of stellar evolution that are identifiable in the CMDs. Other phases that include bright stars that show up in nearly all the CMDs in the database include those on the Asymptotic Giant Branch (AGB), massive main sequence stars, red and blue supergiants, and blue-loop stars. The prevalence of these different stellar types depends on their mass, age, and metallicity. Hence, it is possible to constrain the star formation history (SFH) of a galaxy based on comparing predictions from stellar evolutionary tracks with the observations. This CMD synthesis method is a well-established way to interpret the history of galaxy. I describe these techniques and their results as applied to a case study of UGC4879 in Chapter 4. This dwarf irregular galaxy is of interest because it is located very close to the Local Group, but is still falling into it for the first time, so is

still quite isolated. The proximity and isolation of UGC4879 make it an example of a galaxy with 'pristine' star formation, the history of which can be studied in fine detail.

The analysis applied to the study of UGC4879 involves a fairly large time commitment. More importantly, most CMDs of nearby galaxies do not reach the same depth in absolute magnitude as was obtained for UGC4879, and thus their SFHs are less constrained. Nonetheless, all the CMDs do contain information about the galaxies' stellar populations that provide at least some clues to their SFHs. It is generally simple to determine if a galaxy has formed stars in the last 1 Gyr because the most massive products of the formation will be burning brightly on the main sequence, as supergiants, or on the blue loop. However, as time progresses these massive stars will end their lives as supernovae and disappear from the CMD. Long-lived, low-mass stars are generally too faint to be observed on the main sequence for any galaxies outside the Local Group. However, towards the end of the their lifetimes the lower mass stars increase their luminosity as red and asymptotic giants. The early AGB is generally indistinguishable from the more populated RGB, but the thermally-pulsing AGB extends to the bright side of the TRGB in I-band (Gallart et al. 2005). Stellar evolution models predict that the relative number of thermally pulsing AGB stars compared to the number of RGB stars depends on their age. Those on the AGB spend less time in this phase than those on the RGB, so the ratio of their numbers will fall as time passes from their formation. I used these model predictions to justify the estimate of age of the older stars in UGC4879 in Chapter 4. In Chapter 5 I measure the ratio of AGB to RGB stars for $\sim$90 other dwarf galaxies. The age dependence of this ratio is affected by the metallicity of these stars, and I examine this issue and use the color of the RGB as a proxy for metal content in the study. The results show excellent discrimination by morphological type, as well as some other intriguing trends that are discussed in the chapter.

Chapter 6 summarizes the research undertaken for this dissertation. This has included measuring HST photometry and generating CMDs for a sample of $\sim$300 galaxies. I first use these CMDs to measure TRGB distances to the target galaxies. I then use the distances, along with radial velocity measurements, to reconstruct the galaxies' orbital paths with NAM, and to estimate a background mass-to-light ratio for the sample. After setting a general mass ratio for the sample I focus on the M81 group and repeat the velocity matching techniques to estimate its mass. Then switching topics, I synthesize the CMD of UGC4879 in order to measure its SFH. Finally, using tools from my study of UGC4879, I study the red and asymptotic giant branches of $\sim$90 dwarf galaxies in the sample in order to obtain basic constraints on their stellar histories as revealed by these older stars.

References

Bessel, F. W. 1838, MNRAS, 4, 152

Deupree, R. G., & Wallace, R. K. 1987, ApJ, 317, 724

Gallart, C., Zoccali, M., Aparicio, A. 2005, ARAA 43, 387

Graham, J. A. 1982, ApJ, 252, 474

Hoessel, J. G., & Mould, J. R. 1982, ApJ, 254, 38

Hubble, E. P. 1925, The Observatory, 48, 139

Hubble, E. 1929, Proceedings of the National Academy of Science, 15, 168

Herrnstein, J. R., Moran, J. M., Greenhill, L. J., et al. 1999, Nature, 400, 539

Karachentsev, I. D., Karachentseva, V. E., Huchtmeier, W. K., & Makarov, D. I. 2004, AJ, 127, 2031

Leavitt, H. S., & Pickering, E. C. 1912, Harvard College Observatory Circular, 173, 1

Leavitt, H. S. 1908, Annals of Harvard College Observatory, 60, 87

Méndez, B., Davis, M., Moustakas, J., et al. 2002, AJ, 124, 213

Shapley, H. 1914, ApJ, 40, 448

Shapley, H. 1918, Contributions from the Mount Wilson Observatory / Carnegie Institution of Washington, 151, 1

van Leeuwen, F. 2007, A&A, 474, 653

Chapter 2

The Extragalactic Distance Database: Color–Magnitude Diagrams

Note: This chapter originally appeared as Jacobs et al. (2009), with co-authors Bradley A. Jacobs, Luca Rizzi, R. Brent Tully, Edward J. Shaya, Dmitry I. Makarov, and Lidia Makarova.

Abstract

The CMDs/TRGB (Color-Magnitude Diagrams/Tip of the Red Giant Branch) section of the Extragalactic Distance Database contains a compilation of observations of nearby galaxies from the Hubble Space Telescope. Approximately 300 (and increasing) galaxies in the Local Volume have CMDs and the stellar photometry tables used to produce them available through the web. Various stellar populations that make up a galaxy are visible in the CMDs, but our primary purpose for collecting and analyzing these galaxy images is to measure the TRGB in each. We can estimate the distance to a galaxy by using stars at the TRGB as standard candles. In this paper we describe the process of constructing the CMDs and make the results available to the public.

2.1 Introduction

One of the most productive means of measuring distances to nearby galaxies over the last 10-15 years has been to use stars at the Tip of the Red Giant Branch (TRGB) as standard candles. As the name implies, this technique requires accurate photometry of RGB stars in other galaxies, and the facility most suited to this purpose is the Hubble Space Telescope (HST). We have compiled

HST observations of ∼250 (and counting) nearby galaxies. These observations include imaging in two colors for each galaxy, and we present the resulting Color-Magnitude Diagrams (CMD) as part of the Extragalactic Distance Database[1] (Tully et al. 2009).

The CMDs/TRGB index page of the database lists each galaxy's PGC/LEDA number (Principal Galaxy Catalog/Lyon Meudon Extragalactic Database), common name, HST observing program number, and camera used. Each entry is indexed by its PGC/LEDA number rather than its common name in order to prevent a single galaxy from being listed twice in the database. The PGC/LEDA number and common name fields both serve as links to more detailed information about the galaxy. Each galaxy's CMD webpage is accessible by clicking its common name, while clicking the PGC/LEDA number sends one to a DSS2 image of the galaxy provided by HyperLEDA[2] (Paturel et al. 2003).

Though our primary purpose for producing these CMDs is to measure the apparent magnitude of each galaxy's TRGB, there is a great deal of information about stellar populations that can be gleaned from the figures and photometry tables from which they are derived. For example, a galaxy's metal abundance can be estimated by the color of the RGB (Da Costa & Armandroff 1990; Lee et al. 1993). Some of the HST observing programs from which we present our reductions were designed specifically for the purpose of measuring the TRGB in many galaxies, others came from case studies of a single galaxy, and we include observations from these and various other programs that happened to include observations in filters appropriate for locating the TRGB. The CMD database consists of as large a sample as available of galaxies within ∼10 Mpc, each analyzed in a consistent manner.

2.2 Data

The CMDs are produced by performing photometry on HST images taken with either the Wide Field-Planetary Camera 2 (WFPC2) or the Advanced Camera for Surveys (ACS). The HST flight filter most appropriate for locating the TRGB is $F814W$, which can be described as 'wide I.' In order to discriminate between the RGB and other star types we require observations in another filter. Either of the V-equivalent filters: $F606W$ and $F555W$ most commonly serve this purpose,

[1]Located at: http://edd.ifa.hawaii.edu/ under the Miscellaneous Distances:CMDs/TRGB tab.
[2]Located at: http://leda.univ-lyon1.fr/

but it is possible to use one of the B-like filters such as $F475W$ as well. All of the images used to produce CMDs are available to the public through the HST Archive.[3]

2.3 CMDs/TRGB Catalog

In addition to the general identification, linking, and observational information provided for each galaxy in the CMDs/TRGB Catalog, a subset of the galaxy entries contain data related to and including a TRGB distance measurement. The details of these measurements are described below in the section on TRGB Distances. The eventual goal is to publish this information for each galaxy in the catalog. An extraction of the catalog is given in Tables 2.1 & 2.2. The bulk of the columns in the catalog contain TRGB magnitude and color information. The first three columns of data list our best estimate of the $F814W$ magnitude of the TRGB, followed by low and high values representing the bounds of the 68% confidence interval. These magnitudes are followed by a measurement of the color of the TRGB in the HST flight filters, again with a best, low, and high value reported. In order to facilitate comparison to other datasets we also convert these values to Johnson-Cousins V and I, using the prescriptions from Dolphin (2000a) and Holtzman et al. (1995) for WFPC2, and Sirianni et al. (2005) for ACS. Next, we present an estimate of the foreground extinction based on the dust maps of Schlegel et al. (1998), and use this in our calculations of each galaxy's distance modulus, which we list after the extinction values along with their confidence bounds.

2.4 Footprint Images

The individual galaxy webpages linked from the catalog page each display the footprint of the HST observations used in our analysis. These images were obtained through the Hubble Legacy Archive.[4] We present them in order to put the observations into context. Where there are multiple observations of galaxies of large angular extent we prefer those located towards the edge of the galaxy as seen in the footprint image (taken from Digitized Sky Survey-2), since it is such regions where low-metallicity RGB stars most suitable for TRGB measurements are common and crowding is less of a problem than towards the core. Many galaxies in the sample have a small angular size that fits well within the field-of-view of ACS or WFPC2, and as such no attempt can be made to focus on the

[3]Located at: http://archive.stsci.edu/hst/
[4]Located at: http://hla.stsci.edu/

halo stars. See for example NGC4163 and IC4662 in Figure 2.1. The footprints of the observations used in our analysis are highlighted in yellow. The red boxes represent the footprints of other ACS observations in the field. Footprints of observations other than those used for the production of the galaxy's CMD often appear in these images, but those that are used are always highlighted in yellow. In order to reduce the clutter caused by the necessity of showing these unused observations we only show the footprints of one instrument on each image. So each CMD used with ACS data has one corresponding yellow ACS footprint, and any other ACS observations that happen to fall on the footprint image are shown in red, but no WFPC2 footprints are shown. The situation is similar for galaxies observed with WFPC2, except that non-used WFPC2 observations are shown in blue, and the ACS footprints are turned off. Each image in the database is set to a consistent zoom level corresponding to a field of view of $24' \times 24'$.

2.5 Observation Images

For a subset of galaxies in the database we combine the two-filter observations into psuedo-color images in order provide a sense of the galaxies appearance (we plan to eventually post these images for every galaxy in the catalog). We denote these images at pseudo-color because we lack three channel color information and map the shorter wavelength filter (typically $F606W$) to the blue channel and the $F814W$ image to the red channel. For the green channel we take an average of the two filters. The drizzled ACS images are suitable for this process, while WFPC2 images require additional processing. We use the 'hstmosaic' routine that is part of the HSTPHOT photometry package from Dolphin (2000) to align WFPC2's chips, and clean the image. Figure 2.2 shows the results for ACS observations of NGC4163 and IC4662. These galaxies were chosen in part for their differences in stellar populations even though both have a prominent RGB, which will be evident in their CMDs shown below. There are regions suggestive of active star formation in the image of IC4662 that are not apparent in NGC4163. Inspection of the images allows one to identify regions dominated by old, intermediate, and ongoing star formation. There is no rigor to the detailed color mapping.

2.6 Analysis

We perform photometry on the WFPC2 images using the HSTPHOT (Dolphin 2000) software package, which was developed specifically for observations of resolved stellar populations using this instrument. Dolphin expanded HSTPHOT into a more general photometry software program called DOLPHOT. This release includes an ACS module, and we use this package for analysis of images taken with ACS. Each CMD webpage in the database contains a link to the photometry file output from HSTPHOT or DOLPHOT. These tables hold information about the measurement of a single star per row. There are, among others, columns that describe a star's position on the image, and its apparent magnitude in both flight and ground-based filters, as well as several characterizations of the quality of the measurement. If there are several images per filter available then these values are displayed for each individual image as well as in combination. Hence it is not uncommon for the photometry table to contain more than fifty columns. Though the output is quite complex it breaks into simple sections that are described in detail in the HSTPHOT and DOLPHOT manuals. The column definitions vary between HSTPHOT (for WFPC2) and DOLPHOT (for ACS), so it is important to refer to the correct manual[5] when interpreting the photometry files. To facilitate this we list which camera was used in the observations on the CMDs/TRGB catalog page.

The full photometry files are available through the CMD webpage, but we do not plot every star in those files on their respective CMDs. We use a set of the data quality parameters to reject some measurements as unreliable. Each measurement has a χ value, Sharpness parameter, Object Type, and PSF parameter assigned to it. In order for the measurement to be accepted we require that it fall in the range of values recommended in the manuals, as well as have a Signal-to-Noise ratio: $S/N \geq 5$. Each star measurement that passes all these tests is plotted on the CMD shown on each galaxy's webpage.

2.7 Color-Magnitude Diagrams

Figure 2.3 shows example CMDs from ACS observations of NGC4163 and IC4662 in the $F814W$ and $F606W$ filters. The most prominent feature on the CMDs of these galaxies (and of most other galaxies in the database) is the RGB, seen here as solid wedges due to the high density of points.

[5]HSTPHOT Manual: http://americano.dolphinsim.com/hstphot/
DOLPHOT Manual: http://americano.dolphinsim.com/dolphot/

Other populations visible include the Main Sequence and Blue Loop stars that together form a vertical band seen between about $-0.4 < F606W - F814W < +0.4$. Above and redward of the TRGB are the Asymptotic Giant Branch stars, which are centered at about $F814W = 23$ and $F606W - F814W = +1.3$ for NGC4163 and $F814W = 22.6$ and $F606W - F814W = +1.5$ for IC4662. Each of these regions of the CMD hold a wealth of information about the stellar content and history of the galaxies, but here we focus our attention on the RGB and its tip, which we denote with broken horizontal lines at $F814W = 23.33$ for NGC4163 and $F814W = 23.07$ for IC4662. Note that although the stars that make up NGC4163 and IC4662 are clearly different in metallicity and likely age as well, the TRGB is prominent in both.

2.8 TRGB Distances

Red Giant stars burn hydrogen in shells around a degenerate helium core that has a temperature independent equation of state. While a star is in this phase the mass and temperature of the core continuously increase until the temperature reaches about 10^8 K, at which point triple-α helium burning ignites and sends the star off the RGB to the Horizontal Branch. The helium falling on the core from the outer shell drives this increase in temperature, and hence the degeneracy is broken when the core mass crosses the threshold for helium burning. This mass threshold, therefore, determines an upper limit to the luminosity of Red Giants. The flux from these stars is least sensitive to age and metallicity in I-band (Rizzi et al. 2007), thus our requirement that galaxies be observed in $F814W$.

Early attempts to use the TRGB as a distance indicator simply used by-eye estimates to measure its apparent magnitude. Over the years TRGB measurement methods have become more sophisticated and reproducible (e.g. Lee et al. 1993; Mendez et al. 2002; Makarov et al. 2006; Mager et al. 2008). We employ a program called TRGBTOOL that uses a maximum-likelihood method described by Makarov et al. (2006). This program fits a power-law with a step to a stellar luminosity function created from a portion of the CMD. We apply a color-cut in plotting the luminosity function, excluding stars blueward of the RGB with a limit of $F606W - F814W > +0.4$ used by default, but which can be adjusted such as in cases of significant reddening. The power-law fit is done because, as seen in Figure 2.3 (and indicated by a broken horizontal line), the TRGB appears as a discontinuity in the density of stars at a particular magnitude, decreasing from the tip location to slightly brighter magnitudes. This method also incorporates the results of artificial star tests performed on the

HST images using HSTPHOT or DOLPHOT. This fake photometry is used to account for how completeness, crowding, and color-spreading affect the reliability of the tip measurement. A large majority of the the galaxies in the database with TRGB distances have well populated RGBs, but as populations of stars in the one magnitude below the TRGB drops below 50 or the TRGB lies within one magnitude of the photometric limit there is a degradation in the determination of the TRGB as discussed by Makarov et al. (2006). Figure 2.4 shows the luminosity functions (blue) and fits (cyan and magenta) to the CMDs of NGC4163 and IC4662 taken from a screenshot of TRGBTOOL's interface. The green curve shows the first derivative of the stellar luminosity function. The magenta curve is the model luminosity function convolved with photometric errors and incompleteness. We take the location of the discontinuity in the cyan intrinsic luminosity function as the magnitude of the TRGB. For the galaxy NGC4163 the case for the TRGB to be located at $F814W = 23.33 \pm 0.02$ is clear. The best fit power-law discontinuity falls very close to the steepest part of the rise in the stellar luminosity function. This can be seen in Figure 2.4 where the peak of the derivative of the stellar luminosity function is marked by a green tick and the TRGB discontinuity is marked by a cyan tick. IC4662's fit at $F814W = 23.07 \pm 0.02$ is not so clear in Figure 2.3. The CMD is densely populated around the tip. This situation is clarified by plotting a zoomed-in version of the CMD, shown in Figure 2.5. The confidence intervals of the tip magnitudes are estimated using the likelihood function of the given stellar distribution, which includes photometric error modeling from the artificial star experiments.

Once we have determined the apparent magnitude of a particular galaxy's TRGB we are then able to calculate a distance modulus. The absolute magnitude of stars at the TRGB is $M_I \approx -4.0$ with only a weak dependence on age and metallicity in this wavelength range. Rizzi et al. (2007) present a zero-point calibration that is adjusted for metallicity as well as for the details of HST observations. We use their calibration of the absolute magnitude and correct for foreground extinction using values derived from the dust maps by Schlegel et al. (1998) to produce a distance modulus using the following equation:

$$DM = m_{TRGB} - A_I + 4.05 - 0.217[(V - I) - (A_V - A_I) - 1.6]$$

where m_{TRGB} is the apparent magnitude of the TRGB in I-band, $(V - I)$ is the color of the TRGB, and A_V and A_I are the respective foreground extinction terms. Rizzi et al. (2007) present analogous

formulae for calculating the distance modulus using HST flight filter magnitudes. Extinction within the target galaxies cannot be estimated with these observations. However, we note that the stars most amenable to TRGB distance measurements are old and low-metallicity, those that are preferentially found in the outer halo where dust obscuration is minimal, so when possible we focus on these regions. The uncertainty of TRGB distances we measure from galaxies with well-sampled CMDs (those with a tip at least 1.5 mag above the limit of the observations) typically hover around a three percent. For comparison the interval between tick marks in the vertical scale of the CMDs corresponds to 10% shifts in distance. Details of our procedures are described by Makarov et al. (2006) and Rizzi et al. (2007). But, briefly the likelihood fit from TRGBTOOL produces estimates of the TRGB magnitude and color as well as low and high 68% confidence limits. These values are listed in the catalog as best, low, and high values. The tip magnitude and color limits are propagated into limits on the distance modulus using formulae presented by Rizzi et al. (2007). Given that the RGB tilts to the red with increasing brightness, in applying the distance modulus equation we pair the lower (brighter) limit on tip magnitude with the upper (redder) limit on its color, and vice-versa. For galaxies with a TRGB measurement on the CMDs/TRGB webpage there is also a distance modulus. A portion of this webpage is reproduced in Tables 2.1 & 2.2.

References

Da Costa, G. S., Armandroff, T. E. 1990, AJ, 100, 162

Dolphin, A. E. 2000a, PASP, 112, 1397

—. 2000b, PASP, 112, 1383

Holtzman, J. A., Burrows, C. J., Casertano, S., Hester, J. J., Trauger, J. T., Watson, A. M., Worthey, G. 1995, PASP, 107, 1065

Jacobs, B. A., Rizzi, L., Tully, R. B., Shaya, E. J., Makarov, D. I., Makarova, L. 2009, AJ, 138, 332

Lee, M. G., Freedman, W. L., Madore, B. F. 1993, ApJ, 417, 553

Mager, V. A., Madore, B. F., Freedman, W. L. 2008, arXiv:0808.2180v2 [astro-ph]

Makarov, D., Makarova, L., Rizzi, L., Tully, R. B., Dolphin, A. E., Sakai, S., Shaya, E. J. 2006, AJ, 132, 2729

Mendez, B., Davis, M., Moustakas, J., Newman, J., Madore, B. F., Freedman, W. L. 2002, AJ, 124, 213

Paturel, G., Petit, C., Prugniel, P., Theureau, G., Rousseau, J., Brouty, M., Dubois, P., Cambrésy, L. 2003, A&A, 412, 45

Rizzi, L., Tully, R. B., Makarov, D., Makarova, L., Dolphin, A. E., Sakai, S., Shaya, E. J. 2007, ApJ, 661, 815

Schlegel, D. J., Finkbeiner, D. P., Davis, M. 1998, ApJ, 500, 525

Sirianni, M. et al. 2005, PASP, 117, 1049

Tully, R. B., Rizzi, I., Shaya, E. J., Courtois, H. M., Makarov, D., Jacobs, B. A. 2009

Table 2.1. CMD/TRGB Database (Left)

PGC	Name	Alt. Src.	Dist	GO#	Camera	T814	Lo	Hi	6-8	Lo	Hi	5-8	Lo	Hi
143	DDO221		0.98	6813	WFPC2	20.99	20.90	21.02				1.49	1.40	1.52
621	ESO349-031	ANGRRR	3.21	9771	ACS	23.47	23.43	23.50	1.08	1.08	1.10			
701	NGC24		7.26	12546	ACS	25.30	25.28	25.32	1.33	1.32	1.35			
930	NGC45		6.61	9774	ACS	25.04	24.96	25.11				1.49	1.47	1.52
1014	NGC55	ANGST	2.11	8697	WFPC2	22.66	22.63	22.68				1.68	1.66	1.70
1038	ESO410-005	ANGST	1.92	10503	ACS	22.37	22.33	22.40	1.13	1.12	1.14			
1305	IC10	LGSP	0.79	9683	ACS	22.01	21.99	22.02	2.21	2.19	2.23			
38881	NGC4163	ANGST	2.98	9771	ACS	23.33	23.31	23.35	1.14	1.13	1.14			
60849	IC4662	ANGRRR	2.51	9771	ACS	23.07	23.05	23.09	1.26	1.25	1.26			

Table 2.2. CMD/TRGB Database (Right)

PGC	Name	Tip I	Lo	Hi	V-I	Lo	Hi	E(B-V)$_1$	E(B-V)$_2$	A$_{814}$	M$_{814}$	D M	Lo	Hi
143	DDO221	20.95	20.86	20.98	1.51	1.42	1.54	0.036		0.070	-4.03	24.95	24.86	25.00
621	ESO349-031	23.47	23.44	23.51	1.42	1.41	1.43	0.012		0.023	-4.09	27.53	27.49	27.57
701	NGC24	25.31	25.29	25.33	1.72	1.71	1.74	0.020		0.038	-4.04	29.31	29.28	29.33
930	NGC45	25.05	24.98	25.12	1.38	1.36	1.40	0.020		0.039	-4.10	29.10	29.02	29.18
1014	NGC55	22.62	22.59	22.65	1.70	1.69	1.72	0.013		0.025	-4.00	26.62	26.59	26.65
1038	ESO410-005	22.38	22.33	22.40	1.48	1.46	1.49	0.014		0.027	-4.08	26.42	26.38	26.45
1305	IC10	22.07	22.06	22.09	2.72	2.70	2.74	1.306	0.780	1.519	-4.01	24.50	24.38	24.62
38881	NGC4163	23.34	23.32	23.36	1.48	1.48	1.49	0.020		0.039	-4.08	27.37	27.35	27.40
60849	IC4662	23.08	23.07	23.10	1.63	1.63	1.63	0.070		0.136	-4.07	27.00	26.98	27.02

Note. — Right columns from a portion of the CMD/TRGB database (Table 2.1 shows the left columns), the entire table lists the results for galaxies for which we have measured a tip and calculated a distance modulus. The first nine columns (starting with the left columns) list: PGC Number, Common Name, Alternate Source, Distance in Mpc, HST observing program number, camera used, and TRGB magnitude in $F814W$, followed by its 68% lower and upper limits. This pattern of best mag, lower limit mag, and upper limit mag continues for the rest of the table with the exception of the reddening columns E(B–V) and absolute magnitude of the TRGB M$_{F814W}$, and are presented in blocks of three. Following the $F814W$ TRGB magnitude block are the $F606W$–$F814W$ colors (listed as $6-8$), $F555W$–$F814W$ colors (listed as $5-8$). The blocks continue in the right half of the table (for clarity PGC and name are repeated here) with the converted I-band TRGB magnitudes, and the V–I colors. These are followed by reddening magnitude E(B–V) columns measured from Schlegel et al. (1998) in E(B–V)$_1$ and in some cases directly from the CMD as E(B–V)$_2$, absolute magnitude of the TRGB in $F814W$, and a block of distance moduli.

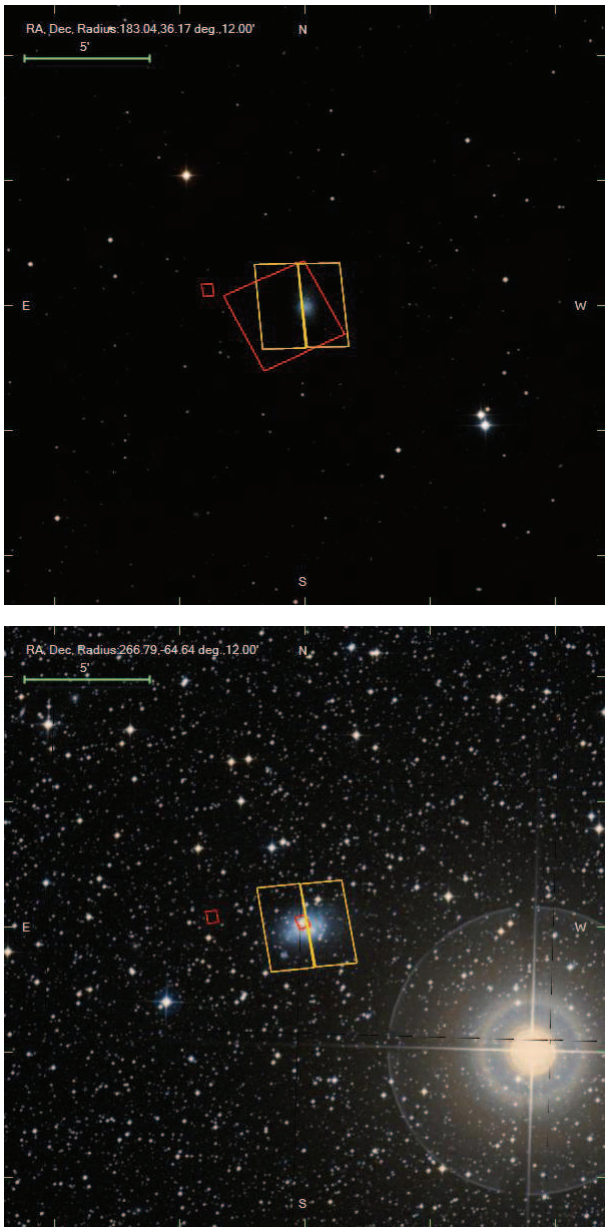

Figure 2.1 HST Footprints of the galaxies NGC4163 (upper) and IC4662 (lower) from ACS observations. The footprint of observations from program 9771 is shown in yellow. The red boxes denote the footprint from another ACS observation of the field.

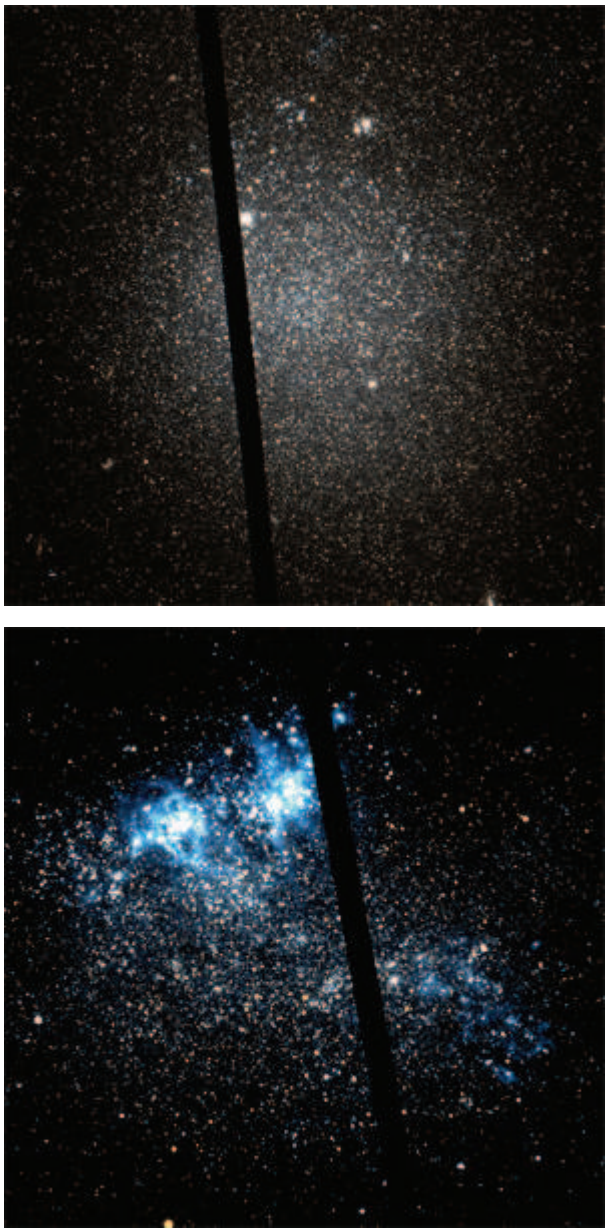

Figure 2.2 Pseudo-color images of NGC4163 (upper) and IC4662 (lower) produced from $F606W$ and $F814W$ filters.

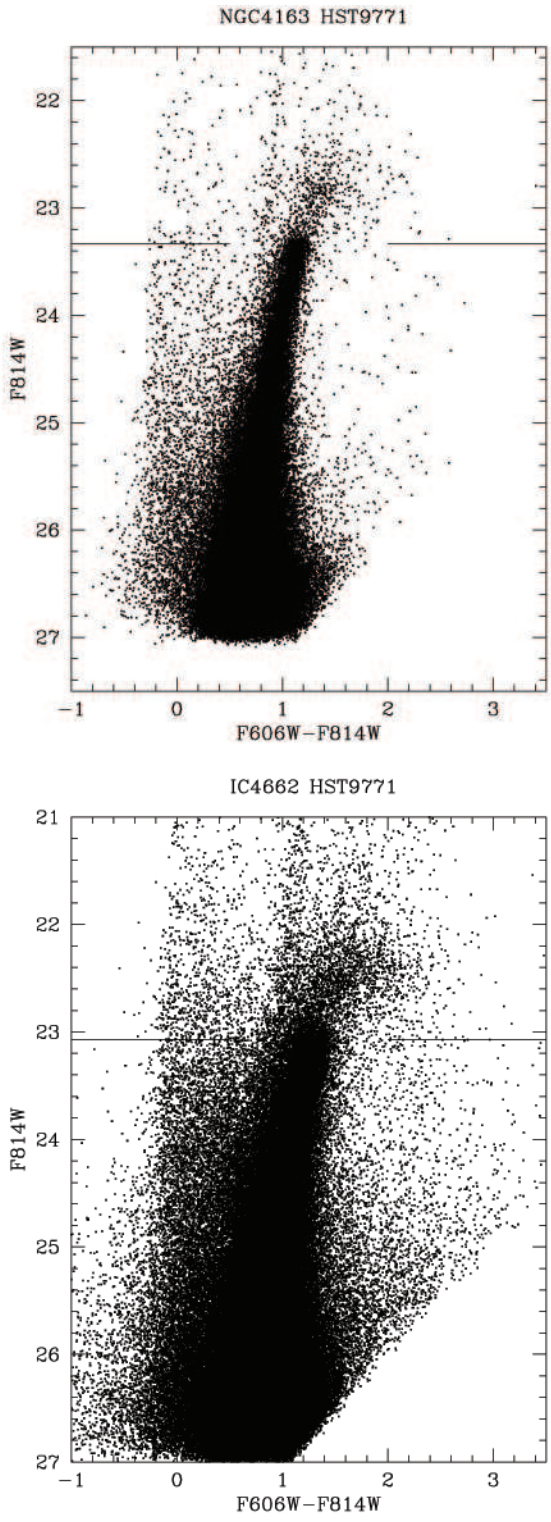

Figure 2.3 CMDs of the galaxies NGC4163 and IC4662 in $F606W - F814W$ versus $F814W$ constructed from ACS observations with HST observing program: 9771. The broken horizontal lines at $F814W = 23.33$ and $F814W = 23.07$ in NGC4163 and IC4662's respective CMDs mark the magnitude of their TRGB.

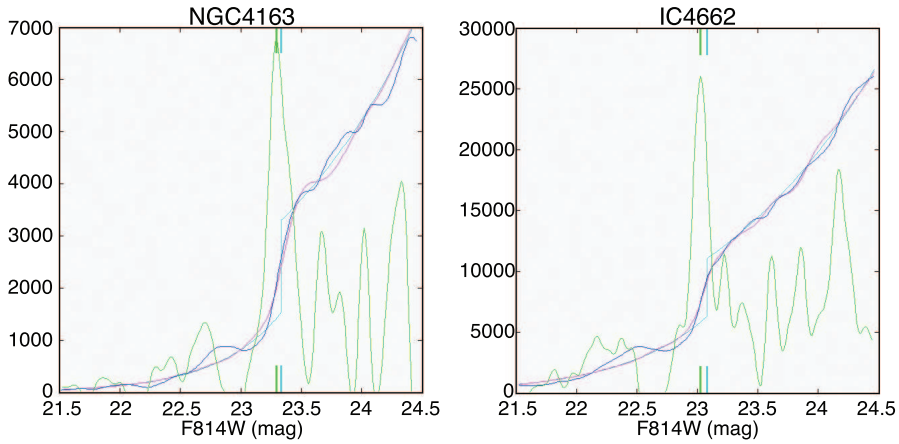

Figure 2.4 Histogram (blue) and fits to the CMDs of NGC4163 and IC4662 taken from a screenshot of TRGBTOOL's interface. The magenta curve is the model luminosity function convolved with photometric errors and incompleteness, from this the intrinsic luminosity function is computed and plotted in cyan. The green curve represents the first derivative of the histogram of the stellar luminosity function. The cyan tick on the $F814W$ axis marks the magnitude of the TRGB, and the green tick marks peak of the first derivative of the histogram. For NGC4163 the peak of the derivative and the TRGB are at$F814W = 23.30$ and $F814W = 23.33$, respectively, and are at $F814W = 23.02$ and $F814W = 23.07$ for IC4662.

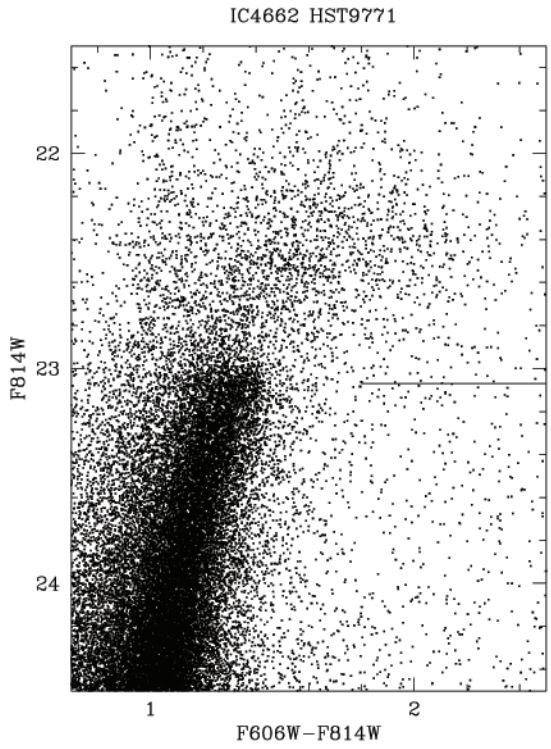

Figure 2.5 CMD of IC4662 in $F606W - F814W$ versus $F814W$ showing the same data as in Figure 2.3 zoomed to a smaller area of color-magnitude space. The line segment to the right of the RGB denotes the tip measurement of $F814W = 23.07$.

Chapter 3

Numerical Action Analysis of the M81 Group of Galaxies

3.1 Introduction

Estimates of dynamical masses of nearby spiral galaxies have historically been based on the gravitational motions of samples of the galaxies' member stars using methods based on the Virial Theorem (e.g. Rubin & Ford 1970; Rubin et al. 1980). These methods probe the mass located within some outermost relaxed orbit. In the context of a luminous galaxy embedded deeply within a larger dark matter halo the stellar motions may enclose only a small portion of the matter in the system. The volume enclosed by 'test particles' can be expanded through the use of the motions of satellite galaxies (e.g. Little & Tremaine 1987; Wilkinson & Evans 1999; Watkins et al. 2010). Care must be taken in this regime, however, to distinguish between galaxies that have relaxed orbits around the giant galaxy, which are relevant to Virial-based mass estimates and those that are in earlier stages of infall/first-passage, where the Virial Theorem is not applicable. We are, therefore, interested in employing a technique that makes use of galaxies that are falling into larger galaxies or groups since these are the systems that are likely to be located near or beyond the outer reaches of the dark matter halo. The numerical action method (NAM: Peebles 1989; Shaya et al. 1995; Peebles et al. 2001) method does not require that a system be relaxed or bound.

Each of these mass estimators require distance measurements to the objects in question, their positions on the sky, and some type of velocity estimate, which is nearly always a spectroscopic radial velocity. The combination of this information for a galaxy gives four of the six terms describing its

position in phase-space. Under NAM we include an additional assumption that a galaxy's peculiar velocity goes to zero at early times, as is required for galaxies forming out of a nearly uniform distribution of matter following the Big Bang. These conditions permit the application of the Principle of Least Action to reconstruct the orbital interactions between galaxies, which is a fully non-linear treatment and can make use of information from galaxies separated by large distances.

Previous studies of galaxy dynamics with NAM have used a variety of techniques to constrain distances of objects included in the input catalog. Those that depend on precise distances have so far been limited to studies of the Local Group (e.g. Peebles 2009, 2010). Others have used a transformed set of NAM equations, where distances rather than radial velocities are allowed to float (Shaya et al. 1995; Peebles et al. 2001; Phelps et al. 2006). In this paper, we introduce a new catalog where the bulk of the entries have distance estimates based on a consistent application of the Tip of the Red Giant Branch (TRGB) method to Hubble Space Telescope (HST) observations of galaxies in the Local Volume (within 10 Mpc). Roughly half of the galaxies listed in the Catalog of Neighboring Galaxies (Karachentsev et al. 2004) have been observed with either the Advanced Camera for Surveys (ACS) or the Wide Field Planetary Camera 2 (WFPC2) on HST, and this set includes nearly all the galaxies with radial velocity measurements that correspond to distances less than the single-orbit observational limit of 4.5 Mpc with WFPC2. This ensemble of galaxies makes up the most detailed strands of the Cosmic Web that are available for study. The distribution of the $\sim$150 galaxies located within this volume begins to show the filamentary nature of large scale structure, as seen in the concentration of galaxies at low supergalactic latitude in Figure 3.1. This plane of galaxies extends to the Virgo Cluster and its pull is causing the local galaxies to align along a filament (Tully et al. 2008).

The construction of this new catalog allows, for the first time a detailed study with NAM of the dynamics of galaxies beyond the Local Group. Our first target for this method is the M81 group. It is the nearest (large and unobscured) group of galaxies outside the Local Group, and recent studies with HST (Chiboucas et al. 2009) and in HI (Roychowdhury et al. 2012) have identified new members and measured their velocities. Also of interest are the interactions of M81 with M82 and NGC3077. The distribution of atomic hydrogen indicates that both M82 and NGC3077 underwent a close passage with M81 between 200 and 300 Myr ago (Yun et al. 1994; Yun 1999). Furthermore, there is some evidence for an uptick in the star formation rate in M81 due to the tidal stream created from these interactions based on its color-magnitude diagram (CMD) (Williams et al. 2009).

3.2 Data

Along with distances to obtain the three dimensional positions of the galaxies, we require measurements of their radial velocities with respect to the Milky Way. These velocities are collected largely through surveys of atomic hydrogen. Additionally, we use luminosities as an initial constraint on the relative masses of the sample. These are obtained, in most cases, from K_s-band observations from the Two Micron All-Sky Survey (2MASS: Skrutskie et al. 2006). We also consider the possibility that a galaxy's mass is correlated with its morphology, and collect morphological types from the Catalog of Neighboring Galaxies (Karachentsev et al. 2004).

3.2.1 TRGB Distances

Historically the favored technique for obtaining high precision distances to nearby galaxies has been to exploit the period-luminosity relation of Cepheid variable stars. However, since its establishment as a reliable distance indicator by Lee et al. (1993) the TRGB method, which depends on the limit to the luminosity of RGB stars that are just about to begin He burning, has proven to hold many advantages over the Cepheids. Both techniques have had success using imaging from HST, but the TRGB method can be used to measure an accurate distance with a single orbit of observations out to 4.5 Mpc with WFPC2 and 10 Mpc with ACS. In contrast, Cepheids require repeated monitoring in order to establish a period of variability. Moreover, TRGB distances can be obtained from all types of galaxies since they need only contain a population of stars older than 3 Gyr to assure the presence of a well-developed RGB, while Cepheids as short-lived massive stars are not found in all environments. Present TRGB procedures using HST CMDs have been shown to regularly achieve accuracies with errors at the 5% level (Rizzi et al. 2007).

The TRGB distances used in these simulations are derived from the CMD/TRGB database (Jacobs et al. 2009), which is part of the publicly available Extragalactic Distance Database (Tully et al. 2009). We carry out photometry of the HST images using the HSTPHOT and DOLPHOT software packages for WFPC2 (Dolphin 2000), and ACS[1], respectively. Both programs include modules to run artificial star tests on the images and we use these to account for photometric errors, completeness, and crowding. With a CMD and errors characterized with artificial star tests, we measure the magnitude and color of the TRGB using a maximum-likelihood method described in

[1]Available at: http://americano.dolphinsim.com/

Makarov et al. (2006). From these measurements we estimate the absolute magnitude of the TRGB using the zero-point calibrations of Rizzi et al. (2007) and account for foreground reddening using the dust maps of Schlegel et al. (1998). Internal reddening is not expected to be a major issue in most galaxies in the sample. However, when multiple fields of a galaxy have been observed (as is often the case with the largest, most heavily obscured galaxies), observations of the stellar halo, where RGB stars are common but dust is not, are preferred. A complete description of the procedures is given in Jacobs et al. (2009).

3.2.2 Radial Velocities

Radial velocities for the sample galaxies are generally available from large surveys of HI using the 21-cm line (e.g. Fisher & Tully 1981; Haynes et al. 1998; Huchtmeier et al. 2003). Some very low luminosity galaxies that are located within 4.5 Mpc are excluded from the sample because they have no detectable HI. Their exclusion is not expected to have much effect on the results since their low masses would not measurably perturb the motions of other, larger systems. The natural frame of reference for comparison of measured radial velocities with the NAM results is with respect to the galactic standard of rest. As such, we need to convert from measured heliocentric velocities V_h to V_{GSR}. We adopt the values used by van der Marel et al. (2012) in their study of the proper motion of M31. This conversion uses the fixed solar velocity components $U = 11.1$, $V = 12.2$, $W = 7.2$ km s^{-1} relative to the local standard of rest estimated by Schönrich et al. (2010). Studies of the supermassive black hole Sgr A* constrain R_0, the distance from the Sun to the galactic center (Ghez et al. 2008; Gillessen et al. 2009), to 8.33 ± 0.35 kpc, as well as the ratio of the solar velocity and distance as $(V_{circ} + V_{pec})/R_0 = 30.2 \pm 0.2$ km s^{-1} kpc^{-1} (Reid & Brunthaler 2004). Van der Marel et al. combine these estimates to generate a circular velocity of $V_{circ} = 239.3 \pm 10.3$ km s^{-1}. We use this velocity along with the Schönrich et al. (2010) motion to change the reference frame from the Sun to the Galaxy. The circular velocity of the local standard of rest is higher than the standard IAU value of 220 km s^{-1} but other implementations of NAM (Peebles 2010) have been shown to prefer values higher than the standard.

3.2.3 Luminosities

The luminosities of nearly all the galaxies in the sample are derived from 2MASS K_s fluxes. We choose this band in order to minimize issues related to obscuration of objects at low galactic latitudes, and 2MASS provides good homogeneity around the entire sky at $|b| > 5^\circ$ for high surface brightness galaxies. For very extended low surface brightness galaxies where 2MASS fluxes are unavailable, K_s-band luminosities are calculated using I-band or (if necessary) B-band observations and transformed using the relations in Tully et al. (1998). At the other end of the luminosity scale, we utilize fluxes from the 2MASS Large Galaxy Atlas (Jarrett et al. 2003) for the most luminous galaxies, with the remaining galaxy fluxes taken from the Extended Source Catalog (Jarrett et al. 2000). Each 2MASS magnitude is converted to a luminosity in units of $L_\odot$ using our measured distance.

Some entries in the catalog encompass multiple galaxies. These are groups and clusters located beyond 10 Mpc and are included to account for their contribution to the local gravitational tidal field. The criterion for listing these systems is described further below, and depends on luminosity. Groups and clusters are identified in Tully & Fisher (1987) and Crook et al. (2007) and assigned a total K_s luminosity that is corrected for completion with distance.

3.2.4 Morphology

The NAM simulations take input masses for all objects in the catalog. These are based on assigned mass-to-light (M/L, units of $M_\odot/L_\odot$) ratios. In order to allow for the possibility of variations based on the morphology of the objects, we include a numerical description of their morphological types. These are based on Karachentsev et al. (2004). In cases where there is more than one galaxy in a single catalog entry, the morphology of the most luminous galaxy in the group is taken to represent the group morphology.

3.2.5 Catalog

The galaxy sample is complete (or nearly so) out to 4.5 Mpc. This limit is from the maximum distance at which the magnitude of the TRGB can be securely measured in a set of observations from WFPC2 taken in a single orbit. Hence, we focus our analysis on the dynamics of galaxies within this volume. However, galaxies located at greater distances are included in the catalog since their gravitational effects on the <4.5 Mpc sample may be significant. Two criteria are used to build

the catalog. The first is that all individual galaxies with measured distances less than 6 Mpc (as well as measured velocities) are listed, with 189 entries. There are 38 galaxies in the catalog between 4.5 and 6 Mpc. Distances to 163 galaxies of the <6 Mpc subgroup are based on the TRGB. Those that meet the distance criterion and have distances based on other methods fall into three categories: they are located in the Local Group and have precise distances available from other techniques, they are located at low galactic latitude and obscuration makes measuring a TRGB distance difficult, or they are located at $4.5 < d < 6$ Mpc and do not yet have suitable HST observations.

The <6 Mpc galaxies make up the sample where we expect to reconstruct their detailed orbital motions, but the effects of larger more distant concentrations of mass on these galaxies cannot be ignored. Therefore, we apply an additional inclusion criterion for the galaxies, groups, and clusters that have significant local gravitational effects. The proxy for gravity used is the total K_s-band luminosity (corrected for completeness in multiple galaxy systems) divided by the square of the distance. We require that this factor be greater than 0.6×10^9 $L_\odot$ Mpc^{-2}. This criterion includes the major nearby clusters, notably: Virgo, Fornax, Centaurus, Norma, and Perseus. A total of 105 systems (most include more than one galaxy) meet this criterion. There are a total of 278 entries in the catalog; 21 meet both distance and gravitational proxy criteria.

3.3 NAM

Various models of NAM have been presented over the years. An early iteration described in Peebles (1989) focused on the motion of eight Local Group galaxies using linear combinations of smooth functions in time and used the Lagrangian form of the cosmological action, $S = \int dt(T - V)$, where T and V are kinetic and potential energy.

$$S = \int_0^{t_0} dt \left(\frac{a^2}{2} \sum m_i \, (\dot{x}_i^\alpha)^2 + \frac{G}{a} \sum_{i \neq j} \frac{m_i m_j}{|x_i^\alpha - x_i^\alpha|} - \frac{2}{3} \pi G \bar{\rho} a^2 \sum m_i (x_i^\alpha)^2 \right) \tag{3.1}$$

The path of the ith particle with mass m_i is x_i^α with α representing the three positional coordinates, and the dot signifies the derivative with respect to world time t in comoving coordinates. The mean background density is $\bar{\rho}$, G the gravitational constant, and a the scale factor. Peebles (1995) introduced a discrete approximation of the action. This approximation is better adapted to describing the more sharply bending orbits expected in tightly bound systems, and in addition

has significantly reduced computation times compared to the previous version. The discrete version is derived from a general expression of the action in terms of the Hamiltonian:

$$S = \int_0^{t_0} \left(\sum p_i^\alpha \dot{x}_i^\alpha - H(x, p, t) \right) dt \tag{3.2}$$

$$S = \int_0^{t_0} \sum p_i^\alpha dx_i^\alpha + H(x, p, t) dt \tag{3.3}$$

The sum is over the position components α and particles i. Equation 3.3 results from integrating Equation 3.2 by parts. The momentum and Hamiltonian are defined as:

$$p_i^\alpha = m_i a(t)^2 \dot{x}_i^\alpha(t) \tag{3.4}$$

$$H = \sum \frac{(p_i^\alpha)^2}{2 m_i a(t)^2} + V \tag{3.5}$$

Following Peebles (1995) this can be written in discrete form under the leapfrog approximation over n time steps as:

$$S = \sum_{n=1}^{N} \left[p_{i2n}^\alpha \left(x_{i2n+1}^\alpha - x_{i2n-1}^\alpha \right) \right] - \sum_{n=1}^{N} \left[\frac{\left(p_{i2n}^\alpha\right)^2}{2 m_i a_{2n}^2} \left(t_{2n+1} - t_{2n-1} \right) + V_{2n-1} \left(t_{2n} - t_{2n-2} \right) \right] \tag{3.6}$$

We are seeking stationary points in the action and by setting the derivative of the action with respect to momentum to zero Equation 3.6 reduces to:

$$S = \sum_{n=1}^{N} \left[\frac{m_i a_{2n}^2}{2} \frac{\left(x_{i2n+1}^\alpha - x_{i2n-1}^\alpha \right)^2}{\left(t_{2n+1} - t_{2n-1} \right)} - V_{2n-1} \left(t_{2n} - t_{2n-2} \right) \right] \tag{3.7}$$

While this equation forces $\partial S / \partial p = 0$, we are also interested in stationary points in the action with respect to the particle positions x_i^α. Specifically, we want to find the coordinate shift δx_i^α that brings the gradient of the action to a stationary point:

$$\frac{\partial S}{\partial x_i^\alpha} \left(x_i^\alpha + \delta x_i^\alpha \right) = 0 \tag{3.8}$$

For brevity, let x_a represent the coordinates of the orbit of particle i at time $t = 2n - 1$, and let the first and second derivatives of the action with respect to these coordinates be S_a and S_{ab}. The first

two terms of the Taylor expansion of the gradient of the action are:

$$0 = S_a\left(x_a + \delta x_a\right) = S_a + \sum_b S_{ab}\delta x_b \tag{3.9}$$

Thus, the coordinate shift is:

$$\delta x_a = -\epsilon \sum_b S_{ab}^{-1} S_b \tag{3.10}$$

where we introduce the parameter $\epsilon \leq 1$ to control the step size, and which can be adapted to the rate of descent. Unlike the simpler method of stepping down the gradient of the action, this formulation is also sensitive to saddle points in the action (Phelps 2000).

In order to find a quantitative measure of the approach to the stationary point, we calculate the square of the gradient of the action for particle i as $\Gamma_i = \sum (S_a)^2$. The coordinate shift reduces Γ_i if the constant ϵ is small enough. The procedure for relaxing a particle's orbit is to calculate its Γ_i and δx_a with an initial value for ϵ and to iteratively increase ϵ when the new coordinates result in a lower Γ_i, and vice versa. We start from random orbits with the positions x_a placed independently at random in the sphere that contains the mass of the system of objects in the background cosmological model. With $\Gamma = \sum_i \Gamma_i$, and the velocity unit 100 km s^{-1}, length unit 1 Mpc, and mass unit 1×10^{11} M$_\odot$, the square of the gradient of the action for the initial random orbits typically is $\Gamma \sim 10^8$ (Peebles et al. 2001). The goal is to construct a set of orbits that result in a decrease of several orders of magnitude in Γ to a point where continued changes in Γ do not result in appreciable changes in the galaxy orbits.

3.4 Application of NAM

In practice the process of iterating δx_a and Γ_i runs into a few obstacles. It can approach a point where Γ has a local but not a global minimum. Usually this occurs when Γ is dominated by a single object. To deal with this eventuality, in cases where $\Gamma_i > \Gamma/2$ for object i its orbit alone is relaxed without adjusting the orbits of the other particles until $\Gamma_i < \Gamma/100$ or to a maximum of 300 iterations. If particle i becomes the dominant contributor to Γ more than 100 times, then its orbit is recast with a new random orbit, and again the other orbits are held constant until $\Gamma_i < \Gamma/100$. For an initial inspection of the results we set a maximum value of $\Gamma = 10$ to consider a trial to be relaxed sufficiently for comparison with others. This value is not small enough to ensure that there

would be no appreciable difference in orbits from solutions with smaller Γ values, which in practice require a reduction of about ten orders of magnitude from the initial value (Phelps 2000). However, we first conduct a search for a set of global M/L ratios that result in orbits that best match the observed radial velocities. For this search we generate a set of 50 solutions for each M/L ratio, and in this regime the detailed orbits become less crucial as they are averaged out to develop a broader picture of how the fit varies with galaxy mass.

We hold a number of parameters constant between each NAM trial. These include the cosmological parameters $\Omega_m = 0.24$ and $H_0 = 74$ km s^{-1} Mpc^{-1} in a flat universe. The Hubble expansion need not be identical to the universal value on small scales, and this is the rate of expansion measured locally (Tully et al. 2008). The orbits constructed trace the galaxies' motion back to $z = 4$ across 400 discrete time steps. The computation time for inverting the matrix describing the second derivative of the action goes as the cube of the number of time steps times the three spatial coordinates $(3N_t)^3$. So the initial time and number of steps are balanced to allow fitting of complex orbits while keeping the computation time reasonable.

As mentioned above, the main parameter that we adjust in searching for viable orbits is the mass. Each galaxy or system of galaxies in the catalog is assigned a M/L ratio and a solution is generated by iteratively adjusting the galaxy's initial random orbit until Γ is reduced to some set value. While adjusting the M/L ratios, another parameter is required to ensure that the overall mass density of the Universe remains fixed between trials. We call this parameter $\Omega_{\rm Smooth}$ and adjust it empirically, based on the difference between the galaxies' rate of expansion in a particular trial and the measured local value of H_0.

3.4.1 Goodness of Fit

The simulated orbits from a trial based on a given set of galaxy masses are assessed by comparing the radial component of the galaxies' velocities at the final time step in the simulations with their observed radial velocities. The details of how the velocity match is assessed affect which M/L ratios are favored. A first inclination for defining this parameter might be to calculate χ^2 for each particle in the catalog. The measured velocities have some uncertainty, but the fractional uncertainty in velocity tends to be significantly lower than the uncertainty in distance. The distance uncertainty is certain to influence the quality of the velocity match, but it is not obvious that the uncertainties in distance and velocity are Gaussian and thus can be added in quadrature. One option is to ignore the

distance uncertainties and calculate the RMS of the differences between the simulated and measured velocities ($\Delta V = V_{\rm sim} - V_{\rm obs}$, not to be confused with the potential energy V in the action equations above). A downside to this approach is that RMS(ΔV) is only meaningful in comparison with other trials where the parameter is calculated in the same way. Therefore, the chances of finding a local but not global minimum are increased because we do not have an absolute measure of the goodness of fit.

A similar issue arises when deciding exactly which galaxies to include in the velocity match parameter. NAM, and specifically the Γ parameter when reduced without intervention, favors the simplest orbits where the galaxies are nearly always still on their first approach to their neighbors at present times. It is safe to assume that this is the case between the most massive local galaxies, e.g. the Milky Way and M31 are approaching each other for the first time. However the dwarf satellites of these giant galaxies may have already completed several orbits around their 'host' galaxies. As such, a match or lack of one, in ΔV for most galaxies in the sample will not be informative in the search for reasonable M/L ratios. Thus, in evaluating a particular trial we only consider the velocities of the most massive (i.e. most luminous) nearby galaxies. The one or two dominant galaxies in each nearby group have K_s-band luminosities greater than 10^{10} $L_\odot$. Meanwhile, galaxies such as the Large Magellanic Cloud and M33, with K_s luminosities of 2.5×10^9 and 4.0×10^9 $L_\odot$, may have already completed their first approaches to the Milky Way and M31 respectively. They therefore, may have orbits that are more complex than what would be modeled in an initial run of NAM. Hence, for the purposes of searching for an appropriate M/L ratio we consider the velocities of only those galaxies with $L_K > 10^{10}$ $L_\odot$.

It is also necessary to impose a distance limit on the galaxies used in this search. The obvious choice is at 10 Mpc, since this is the limit out to which accurate distances from the TRGB are available. The sample is incomplete beyond 4.5 Mpc, but it is expected that the most massive systems that meaningfully contribute to the motion of the local galaxies are included. So we run many trials at various M/L ratios and compared the observed and simulated radial velocities for the 26 galaxies (excluding the Milky Way) with $L_K > 10^{10}$ $L_\odot$ and $d < 10$ Mpc.

While considering a wide range of possible M/L ratios for the galaxies in the sample, we want to remain within the framework of standard concordance cosmology, where the total matter content of the universe is fixed. We achieve this, as mentioned above, with the inclusion of parameter $\Omega_{\rm Smooth}$ to account for any matter that is not included in the putative galaxy masses used in a given trial,

i.e. trials with low mass ratios will have higher values of $\Omega_{\rm Smooth}$. We set the precise values of this parameter empirically by requiring that the mean of the differences between the observed and simulated velocities for the test galaxies be consistent with zero. Thus if a given set of trials has a net outflow (beyond the expansion rate of 74 km s^{-1} Mpc^{-1}), we run a new set of trials with an increased $\Omega_{\rm Smooth}$. Hence, while maintaining the mean of the velocity match ΔV at zero we search for a minimum in RMS(ΔV) from the 26 most luminous galaxies in the Local Volume.

As we searched this parameter space, we noticed that most of the 26 galaxies (not counting the Milky Way) with $L_K > 10^{10}$ L$_\odot$ and $d \lesssim 10$ Mpc, followed a general trend in their velocities over various input masses, but that some differed from this trend. This can be illustrated by plotting the median value of ΔV from a set of 50 trials at a given M/L for these 26 galaxies across a range of input M/L ratios. In principle the $\Omega_{\rm Smooth}$ factor needs to be decreased as M/L increases, so that the total mass in the system remains constant. However, it can be instructive to see what trends are apparent when $\Omega_{\rm Smooth}$ is not varied. Figure 3.2 shows this relation with $\Omega_{\rm Smooth}$ set to zero. Under this scenario the majority of the galaxies have median ΔV values that are positive at low M/L and decrease smoothly with increasing M/L. This behavior is expected, when $\Omega_{\rm Smooth} = 0$. At high mass-to-light ratios (regardless of the value chosen for $\Omega_{\rm Smooth}$) the galaxies' strong mutual attraction will result in radial velocities that show a net in-fall compared to their observed velocities (which include the local expansion rate). At lower ratios (when not compensating with $\Omega_{\rm Smooth}$) the mutual gravitational forces are reduced and they will be insufficient to retard the expansion rate to match the observations, resulting in positive ΔV's. Of the 26 galaxies sampled, 17 of these follow this trend. Three galaxies: M66, M104, and most notably M82, have median ΔV values that *increase* with increasing mass. Another four galaxies: Cen A, NGC4945, M64, and NGC5195 have median velocities that are virtually constant across the range of input ratios. There are a couple of likely causes of these two behaviors. One comes from the influence of neighbors. M82, as mentioned above, is influenced by M81, and similarly: M66 is part of the Leo Quartet, NGC4945 is in the halo of Cen A, and NGC5195 is the companion of NGC5194. Secondly, both M104 and M64 are in the Virgo infall region and are therefore less sensitive to local masses. Two other galaxies: M101 and NGC2784 follow the general downward trend in ΔV as masses are increased, but at least at higher ratios, their values are offset by around 100-200 km s^{-1} above the other galaxies that follow the expected trend. M101 is evacuating the Local Void, while NGC2784 is located well below the Supergalactic Plane, and both are more sensitive to large scale void influences than rest of the

sample which generally lie close to the plane. We exclude these 9 cases from further consideration in determining a general mass-to-light ratio for the catalog. The median ΔV values for the remaining 17 galaxies are shown in Figure 3.3. These galaxies are: M31, NGC253, M81, Maffei 1, IC342, Maffei 2, Circinus, M94, M83, NGC6946, M106, NGC2683, M51, NGC2903, M63, NGC891, and NGC1023. Of these galaxies only Maffei 1 and NGC1023 have early morphological types, so while it is possible that mass-to-light ratios depend on morphology, we are insensitive to this here, and therefore apply one ratio across the entire catalog.

We adjust $\Omega_{\rm Smooth}$ so that the mean ΔV of the 17 sample galaxies is consistent with zero for a given input mass ratio, up to a limit of $M/L = 60$. For $M/L \geq 70$ we set $\Omega_{\rm Smooth} = 0$, because even at this level the mean ΔV for the sample is negative, which is evocative of an upper limit on M/L. These values, along with several other measures of from the set of 50 trials run at a given ratio are listed in Table 3.1. Figure 3.4 shows the median ΔV from each set for the 17 test galaxies. One might hope to see a "pinch" in this plot, where the values approach zero at a particular ratio. The variance among the ΔV values does fall from the largest spread seen at $M/L = 10$ or 20, and since higher masses result in significant negative velocities relative to observations, these are also disfavored. Therefore, the preferred ratio is likely somewhere in the middle, but it is not obvious from this plot where exactly this might be. For that we return to the RMS(ΔV) parameter.

3.4.2 Iterative Search of M/L Ratios

Each input M/L ratio is tested with a set of 50 trials. The necessity of many trials per ratio comes from the variance in the results due to differing initial random orbits for otherwise identical initial conditions. The obvious way to evaluate the results of the trials is to calculate the mean of the match between the velocities of the 17 test galaxies, RMS(ΔV), for each input M/L. However, by taking the mean we are giving equal weight to the poorest and best matching trials in a given set. In the course of comparing each set of trials it became clear that the mean is not necessarily sensitive to the best matching trials. This is because the amount of variance between trials in a given set is highly correlated with the input M/L. At low M/L the gravitational forces between the galaxies are weaker than at higher ratios and the overall motion will remain simpler, and thus less variable between trials. Meanwhile, at high ratios the stronger gravitational forces induce more extreme motion, and as a result more variability between trials. One option would be to consider only the minimum RMS(ΔV) from each set, but it is difficult to assign an uncertainty to this single value.

Thus, we also consider a compromise between taking the mean of all trials from a set or taking the single best value from that set: the mean of the 10 best matching trials from the set of 50.

The representations of RMS(ΔV) (calculated from the 17 test galaxies) against M/L are plotted in Figure 3.5. The means across each set of 50 trials are shown as squares and have a minimum at $M/L = 40$ or 50. The means of the best matching 10 trials out of the 50 are displayed as triangles, while the best matching trials from each set are shown as small circles. The mean of the best 10 and single best RMS(ΔV) values track each other much more closely than the means from all 50 trials, and they have a broad minimum at $M/L = 50$ to 70. The divergence between the best matching trial and the mean across all trials increases with M/L, and this increasing variance introduces a bias such that the full mean has a minimum at lower ratios that what is observed using the best matching trial or the mean of the 10 best matching trials.

The fact that a fairly wide of range mass-to-light ratios, $M/L = 60 \pm 10$, are consistent with the best matching cases, might have been predicted by the lack of a "pinch" in the median ΔV values shown in Figure 3.4. This is also reflected in the value of RMS(ΔV) which is around 40 km s^{-1} for the best matching trials at these ratios. There are a few different sources of this imperfect match. These fall into four categories: issues with the data, issues with how the inputs to the simulations are chosen, issues with the simulations themselves, and issues with how the results are interpreted. The data are, as always, incomplete and uncertain and any number of factors will result in a deterioration in the agreement between the simulations and observations. The biggest factor here is most likely that the finite size of the catalog means that the true motion of the test galaxies cannot be reproduced in the simulations because large scale issues such as a full sample of the periphery of the Local Void are missing. Uncertainties in the distances, and to a lesser extent velocities of the galaxies that are included in the catalog also increase RMS(ΔV). In terms of the inputs, there are many factors that can be adjusted, but the single most important one is how the masses are defined. We have assigned a single M/L ratio for the entire catalog, though there is no reason to expect that a 'universal' ratio exists. The simulations would accept individually adjusted masses for each entry in the catalog, but it is prohibitively expensive to search for a match when varying the masses of more than just a few galaxies. We therefore, need to define a background M/L for all the galaxies that will not receive special attention. This is what we are attempting to do here, but it is clearly not an ideal solution. With the simulations, the orbits are based on the Principle of Least Action, and in practice this means that the resulting orbital paths are nearly

radial, even in dense environments where there is strong evidence for complex interactions. We will touch upon this point again, but simple paths preferred by NAM relate to the final category of problems: comparing the simulations with observations. The real question in comparing observed and simulated velocities involves choosing exactly which galaxies to use in this comparison. We have chosen to use 17 massive nearby galaxies that have simulated velocities that vary with mass as we expect (and are likely to be following fairly simple orbits). But there is no guarantee that this particular group represents the ideal sample for determining a background mass-to-light ratio for the catalog. Nonetheless, given these caveats, going forward we use an estimate of $M/L = 60 \pm 10$ for most galaxies while we probe the M81 group in more detail.

3.5 M81 Group

3.5.1 Masses

In order to obtain an estimate for the mass of the M81 group we conduct a process similar to the one used to determine a background M/L ratio, which first involves choosing test galaxies. The galaxies that are useful as probes of the mass of the M81 group are those that are near enough to it that they are significantly perturbed by it, yet are not likely to be undergoing complicated orbits in or around the core of the group. As before, we judge which galaxies meet these criteria empirically by running new sets of trials and examining the resulting apparent radial velocities. For these new trials we set a ratio for M81 and M82, $M/L_{\rm M81M82}$, and define $M/L_{\rm Others}$ for all other galaxies. Initially, we hold $M/L_{\rm Others} = 60$, and run various trials with different values for $M/L_{\rm M81M82}$. M81 and M82 have K_s-band luminosities of $8.26{\times}10^{10}$ and $3.68{\times}10^{10}$ $L_\odot$, respectively, while the next most luminous member of the *core* of the group is NGC3077 at $3.10{\times}10^{9}$ $L_\odot$. Since NGC3077 is less than 10% the luminosity of the two largest members, and our search for a background mass-to-light ratio shows that we are unlikely to be sensitive to differences in mass at the 10% level, we do not vary the M/L ratios of NGC3077 or the other less luminous members of the group. Hence, $M/L_{\rm M81M82}$ serves as our proxy for the mass of the M81 group.

We identify galaxies that serve as tracers of the M81 group mass by examining their median ΔV's taken from sets of trials run at various $M/L_{\rm M81M82}$. Galaxies that are distant from the M81 group have velocities that are constant as $M/L_{\rm M81M82}$ varies, while nearer galaxies are sensitive to this variation, and those nearest the core of the group will have complicated trends in their ΔV values.

It is fairly easy to identify galaxies that are insensitive to M81 and M82 and eliminate these from consideration as we step closer to the group. Ideally the galaxies that trace the group mass would have median ΔV measurements that vary monotonically with the mass of M81 and M82 (as the test galaxies used to determine the background M/L ratio had ΔV values that decreased monotonically). Four galaxies on the periphery of the group meet this criterion: NGC4236, UGC6456, UGC8201, and UGC7242. All these galaxies are located behind the core of the group and above the Supergalactic Plane, in which the group is situated. As such, they all show a similar behavior in their ΔV values: as the mass of M81 and M82 increases ΔV decreases because some of the additional gravitational pull is in the direction of the Milky Way, see Figure 3.6. It is useful then, to consider galaxies that are approaching M81 from a different perspective, i.e. those between it and the Milky Way. NGC2403 and the galaxies around it: NGC2366, UGC4305, and UGC4459, form a sub-group that is approaching M81 from the near-side. The positions of all these galaxies are shown in Figure 3.7, while their median ΔV's are plotted in Figure 3.6. Unlike the far-side tracers, these galaxies' medians do not vary monotonically with M/L_{M81M82}, which is mostly due to their interactions with each other. Nonetheless, they do follow a general trend of increasing ΔV with increasing M81/M82 mass. We also consider other galaxies to trace the M81 group mass, but the nearest galaxy to M81 that we have considered so far, UGC4459, is about 0.5 Mpc distant from it. This is just outside the estimated radius of second turnaround for the group (Tully 2010), so it is increasingly likely that galaxies that are farther in towards the core are following complex orbits that are unlikely to be predicted with NAM. As such we take the 8 galaxies discussed here to be tracers of the M81 group mass.

The opposite trends in median ΔV of the near- and far-side tracer galaxies make sense given their positions relative to the main M81 group. As previously described, the more distant galaxies have radial velocities that from our perspective are slowed due to the gravitational attraction to the M81 group. The opposite effect is seen with the galaxies located between us and M81, increasing the mass of M81 and M82 increases their simulated apparent radial velocities. Thus, we would hope to find a mass ratio that causes both the near- and far-side tracers to have ΔV values that approach zero from the negative and positive sides, respectively. Unfortunately, the far-side galaxies go into negative territory while the near-side galaxies are negative as well, so there is no ratio where ΔV for the 8 tracer galaxies is consistent with zero. This is seen in a plot of RMS(ΔV) for these galaxies, shown in Figure 3.8 as triangles. In this case we have chosen to only plot the mean of the 10 lowest

RMS(ΔV) trials calculated for the 8 tracer galaxies from each set of 50 as our statistic of choice. There is a general downward trend in the values as we approach $M/L_{\rm M81M82} \sim 100$ from either side. However, this trend is not completely smooth, so the there is some question about how significant it is that there is a minimum at $M/L_{\rm M81M82} = 90$. This choppiness is due to the lack of monotonicity in ΔV among the galaxies in the NGC2403 subgroup. One option to reduce this issue is to consider only the velocity of NGC2403 as representative of the motion of the subgroup. However, this would leave an imbalance where we use the velocities of 4 galaxies located behind M81 and only one galaxy in the foreground. To rectify this, we also plot the (best 10) RMS(ΔV) statistic using only NGC2403, NGC4236, and UGC6456, displayed as stars in Figure 3.8. We eliminate UGC8201 and UGC7242 because they are significantly more distant from M81 than either NGC4236 or UGC6456, which are about 1.1 Mpc from M81 (and from each other). This trio of galaxies does have a smoothly varying relation between $M/L_{\rm M81M82}$ and RMS(ΔV), and a minimum at $M/L_{\rm M81M82} = 90$.

These tests are performed while holding $M/L_{\rm Others}$ at 60. We have conducted more limited searches at $M/L_{\rm Others} = 50$ and 70, and observed similar minima around $M/L_{\rm M81M82} = 90$. So there are indications that the mass of the M81 group is higher than our background value. However, the range of possible M/L ratios that produce results that are similar to what is seen from the best matching trials is fairly wide. Moreover, the uncertainty in $M/L_{\rm M81M82}$ is related to the uncertainty in $M/L_{\rm Others}$, so one cannot simply add their uncertainties in quadrature (even if these uncertainties were rigorously defined, which they are not). We can claim that our simulations prefer a value of $M/L_{\rm M81M82}$ around 90, and note that this corresponds to masses of $1.1{\times}10^{13}$ $M_\odot$ for the pair. Though, depending on which galaxies are designated as tracers, the uncertainty in $M/L_{\rm M81M82}$ could be around ± 20, if we take the best 10 RMS statistic to be the best measure of agreement between observed and simulated velocities (also not a given). Hence, it is probably somewhat of an over-reach to claim that the mass ratio found for M81 and M82 is statistically significantly higher than the background ratio. It is nonetheless intriguing that the simulations prefer masses for M81 and M82 that equate to a mass-to-light ratio as high as 90.

Previous estimates of the mass of the M81 group, such as those based on the Virial Theorem and from estimating the distance to the zero-velocity surface from M81 put the mass of the group at around $2{\times}10^{12}$ $M_\odot$ (Karachentsev et al. 2002). Taken at face value $M/L_{\rm M81M82} = 90$ implies a group mass of $\sim 1 \times 10^{13}$ $M_\odot$. This large discrepancy may be evidence that the masses inferred from NAM are inflated due to the issues previously discussed, and are not reliable at factors tighter than a few.

It is possible that there is a substantial amount of matter outside the Virialized region of the group, though probably not enough to cover the difference. We also note that each of these mass estimates are based on extrapolations from apparent radial velocities and distances. That is certainly true of NAM, except that the simulations also generate predictions about the transverse motions of the galaxies. We find relatively good matches with the observed radial velocities of the galaxies on the periphery of the group when $M/L_{\mathrm{M81M82}} = 90$, but the simulations also provide velocity estimates in the other two dimensions. For example, the near-side tracer galaxies are located below the main group in Supergalactic Z and those on the far-side are located above it. In the simulations both sets of galaxies have substantial velocities directed towards the Supergalactic Plane, where the main group is located. The vector of this motion is nearly perpendicular to our line of sight. The estimate of the group mass based on identifying the zero-velocity surface depends on the radial velocities of many galaxies around the periphery of the group. So while it does probe mass outside the Virial region, it will tend to underestimate mass if transverse velocities contribute systematically to these galaxies' motion relative to the group center. Admittedly, a factor of five difference is a wide gap and rapid transverse velocities would likely only explain a portion of it, so we return to the uncertainties from the simulations as an important factor. The wide minima seen when trying to determine the M/L ratios allow quite a bit of variation in the masses that are consistent with these minima. That said, even at $M/L = 60$ the combined mass of M81 and M82 would be about $7{\times}10^{12}$ $\mathrm{M}_{\odot}$. The NAM results prefer large galaxy masses, and while they are highly dependent on which galaxies' velocities we choose as representative, these choices would have to be way off to have resulted in missing the 'true' M/L ratio around 20, which is what is required for M81 and M82 to have a combined mass of about $2{\times}10^{12}$ $\mathrm{M}_{\odot}$.

3.5.2 Orbital History

A mass estimate for the M81 group has always been the primary motivator for this work, but the NAM simulations' primary function is to generate orbital solutions for galaxies using given input masses. Up to this point we have considered only the radial component of the velocity from the final time-step of the orbital path of the selected galaxies. Therefore, it behooves us to examine the galaxies' simulated paths more fully. Focusing again on M81 and M82 we find that when NAM is run without intervention, there is a remarkable consistency among the paths generated by NAM. In particular, the general form of these paths does not change, even when using significantly different

M/L ratios. In these simulations M81 and M82 follow paths that are close to linear but that gently curve towards each other as they reach their present day positions. As such, one can simply characterize these paths using the Supergalactic Cartesian coordinates of the initial position, which is defined to be at redshift $z = 4$. As an example, we compare the sets of trials where $M/L_{\rm M81M82} = 90$ and 30 ($M/L_{\rm Others} = 60$), and for M81 find that these initial positions are $SGX_0 = 7.5 \pm 0.2$ Mpc and $SGY_0 = -1.8 \pm 0.1$ for *both* sets of trials. The situation in SGZ_0 is only slightly more complex, where most trials in both sets start at -1.2 ± 0.2 Mpc, but roughly 20-30% of the trials of both sets have M81 starting at 1.1 ± 0.3 Mpc. M82 follows similar trends, except that there is a bit more variation between the trials at $M/L_{\rm M81M82} = 90$ and those at 30. It has an initial position $SGX_0 = 6.0 \pm 0.1$ Mpc for the mass ratio at 90 that shifts to 6.5 ± 0.2 Mpc for a mass input of 30. Similarly, with SGY_0 it is -2.7 ± 0.2 and -2.4 ± 0.3 Mpc, for $M/L_{\rm M81M82}$=90 and 30, respectively. In terms of SGZ_0 M82 mirrors M81: in most trials M81 starts off below the Supergalactic Plane and in those trials M82 starts off above it, and the converse is also true. These positions are either $SGZ_0 = 3.0 \pm 0.1$ or -2.8 ± 0.2 Mpc when the input masses of M81 and M82 are 90, or 2.3 ± 0.3 or -2.0 ± 0.2 Mpc for the input at 30. In summary, the NAM simulations consistently predict that M81 and M82 are separated by about 3 to 5 Mpc at $z = 4$, most of which is due to separation in SGZ that closes over time as the both approach the Supergalactic Plane. Their paths in SGX and SGY are dominated by motion towards Virgo, but they do attract each other along these coordinates as well.

We have not studied the paths of other galaxies in as much detail as with M81 and M82, but it is generally true that other galaxies have simulated paths that are consistent across a wide range of mass inputs. Depending on one's perspective, this consistency can either be a virtue or a detriment for NAM. On one hand, it would be difficult to interpret results that had orbital paths that were qualitatively different from trial to trial and ratio to ratio. On the other hand, if one has reason to doubt that the true orbits are similar to those preferred by NAM, then it can be difficult to find trials that might fit these other constraints. One of the developers of NAM, Ed Shaya, has built a technique known as backtracking to address this issue. Under this technique the user takes the results from a particular trial and chooses a galaxy that will be given a new orbital path by having that galaxy follow the gravitational field defined by holding the paths of all the other galaxies constant. There are of course many possible paths that the galaxy could follow, but these can be specified by defining an initial direction for the galaxy's velocity vector at the first time step. So by

examining how these orbital paths vary depending on the initial pointing, along with Γ_i the sum-of-squares measure of the galaxy's action, it is possible to generate stable paths with multiple orbit crossings in NAM (which otherwise do not appear spontaneously). The caveat to this is that if the backtracked orbit significantly alters the paths of neighboring galaxies, the results will be unstable. Thus the technique works best for the lower mass galaxies in the sample.

The galaxies in the central part of the M81 group, within say 0.4 Mpc of M81, have observed radial velocities that diverge substantially from the results of the simulations when we use ratios near the preferred values of $M/L_{\rm Others} = 60$ and $M/L_{\rm M81M82} = 90$. Furthermore, the tidal debris that is observed among these galaxies suggests that one or more close interactions have taken place between M81, M82 and NGC3077 in the past. Since the nominal orbital paths from NAM do not include these types of orbit crossings, application of the backtracking technique would appear to be in order. Unfortunately, backtracking the orbits of M81 and/or M82 is problematic because of their high masses/luminosities compared to the other galaxies in the group. Any change in their motion will leave the group's orbits completely unsettled, so without prior knowledge of the orbits of M81 and M82 with respect to each other, it is unlikely that we will happen upon a stable result where their observed and simulated radial velocities agree.

One alternative to consider is that the orbits of M81 and M82 do actually resemble those predicted by NAM. As described above, these paths are substantially similar for $M/L_{\rm M81M82} = 90$ and 30. The sets of trials run with the ratio at 30 happen to produce results that have fairly good agreement with their observed radial velocities (and much better than at 90, where the proper motions are large). However, as is seen in Figures 3.6 and 3.8, the velocities of our tracer galaxies that are expected to have orbits that are well reproduced by NAM do not match at these low ratios. In addition, we fail to find stable results from backtracking the orbits of the other main members of the central part of the group: NGC3077, NGC2976, and IC2574. Moreover, the trend in the simulated ΔV values for M81 and M82 varies smoothly with their mass ratio (since their orbital paths remain nearly the same), so it may just be a coincidence that they happen to line up best at around 30. Finally, also recall that the ΔV values calculated for M82 increased with M/L, which holds true when we vary $M/L_{\rm M81M82}$ with $M/L_{\rm Others}$ constant, and this reversal of the expected relation is suggestive of a complex orbit. Thus, we find it more plausible that the group contains large amounts of matter and that the galaxies, including M81 and M82, have already gone through interactions with each other, than this scenario where there is less matter in the group, but that NAM reproduces the simple

orbital paths of M81 and M82, which do not fit with observations that show strong evidence of tidal interactions in the group.

3.6 Summary and Conclusion

Using our newly constructed catalog of local galaxy distances measured via the TRGB method applied to observations with HST, we run simulations that attempt to reconstruct the motion of these galaxies from early times, based on a numerical formulation of the Principle of Least Action. Our main goal here is to use these simulations as a tool to estimate the total dynamical masses of galaxies/groups selected from the sample. We achieve this by running many trials using a range of input masses, as defined by mass-to-light ratios, and comparing the predicted present-day velocities with respect to the Milky Way with observations. The data for these comparisons are K_s-band luminosities which are nearly all based on 2MASS fluxes, along with spectroscopic velocities that are mostly derived from surveys of HI gas.

In this paper, we have focused on estimating the mass of the M81 group, but prior to this it is necessary to define a M/L ratio or ratios for all the other galaxies in the catalog. Using 17 galaxies that we have chosen as representative, we find that a general ratio at $M/L_{\rm Others} = 60 \pm 10$ minimizes the difference between simulated and observed radial velocities. While defining such a ratio implies that we have a dynamical mass estimate for each galaxy in the sample, we do not claim that a 'universal' mass ratio exists as such, only that this ratio serves as a foundation for further investigation. In the case of M81, we find evidence that it and M82 have mass-to-light ratios around 90. We base this inference on the motion of galaxies that are expected to be in or near the edge of the in-fall zone of the group. The uncertainty in the mass ratio for M81 and M82 is coupled with the uncertainty in the background ratio, and is itself uncertain. Thus, we cannot rule out the possibility that the combination of these mass ratios includes some systematic biases, and therefore refrain from stating an explicit uncertainty range for M/L of M81 and M82. Nevertheless, if this estimate can be taken at face value, or at least if the estimate is statistically significantly higher than the broader average, then it would imply the presence of a large amount of dark matter in the group that has not been previously detected.

One way to bolster the claim that our mass estimates for M81 and M82 are reasonable would be to use these estimates in a reconstruction of the dynamical state of the group. The reconstruction

would be assessed in terms of the quality of the radial velocity matches of the central members, as well as whether the orbital paths that are generated are consistent with the tidal debris observed in the group. Up to this point, we have not succeeded in developing a picture of the M81 group core that is a good match with the observations. This is due to our lack of knowledge about the details of the interactions between M81 and M82. In contrast, the NAM orbit reconstructions have been more successful in the Local Group, where we know that the Milky Way and M31 are approaching each other for the first time. A potential avenue for improving this situation would be to focus on modeling the interactions of M81 and M82 as an N-body simulation, such as with the gravitational encounter software Identikit (Barnes & Hibbard 2009; Barnes 2011), and then using these results to narrow the range of possible orbital paths obtained through the backtracking technique in NAM. These or similar steps will be necessary to complete the picture of the mass and dynamical state of the M81 group.

References

Barnes, J. E., & Hibbard, J. E. 2009, AJ, 137, 3071

Barnes, J. E. 2011, MNRAS, 413, 2860

Chiboucas, K., Karachentsev, I. D., & Tully, R. B. 2009, AJ, 137, 3009

Crook, A. C., Huchra, J. P., Martimbeau, N., et al. 2007, ApJ, 655, 790

Dolphin, A. E. 2000, PASP, 112, 1383

Fisher, J. R., Tully, R. B. 1981, ApJS, 47, 139

Ghez, A. M., Salim, S., Weinberg, N. N., et al. 2008, ApJ, 689, 1044

Gillessen, S., Eisenhauer, F., Trippe, S., et al. 2009, ApJ, 692, 1075

Haynes, M. P., van Zee, L., Hogg, D. E., Roberts, M. S., Maddalena, R. J. 1998, AJ, 115, 62

Huchtmeier, W. K., Karachentsev, I. D., Karachentseva, V. E. 2003, A&A, 401, 483

Jacobs, B. A., Rizzi, L., Tully, R. B., Shaya, E. J., Makarov, D. I., Makarova, L. 2009, AJ, 138, 332

Jarrett, T. H., Chester, T., Cutri, R., et al. 2000, AJ, 119, 2498

Jarrett, T. H., Chester, T., Cutri, R., Schneider, S. E., & Huchra, J. P. 2003, AJ, 125, 525

Karachentsev, I. D., Dolphin, A. E., Geisler, D., et al. 2002, A&A, 383, 125

Karachentsev, I. D., et al. 2003, A&A, 398, 479

Karachentsev, I. D., Karachentseva, V. E., Huchtmeier, W. K., Makarov, D. I. 2004, AJ, 127, 2031

Karachentsev, I. D., Kashibadze, O. G., Makarov, D. I., Tully, R. B. 2009, MNRAS, 393, 1265

Lee, M. G., Freedman, W. L., Madore, B. F. 1993, ApJ, 417, 553

Little, B., & Tremaine, S. 1987, ApJ, 320, 493

Makarov, D., Makarova, L., Rizzi, L., Tully, R. B., Dolphin, A. E., Sakai, S., Shaya, E. J. 2006, AJ, 132, 2729

Peebles, P. J. E. 1989, ApJ, 344, L53

Peebles, P. J. E. 1995, ApJ, 449, 52

Peebles, P. J. E., Phelps, S. D., Shaya, E. J., Tully, R. B. 2001, ApJ, 554, 104

Peebles, P. J. E. 2009, arXiv:0907.5207

Peebles, P. J. E. 2010, arXiv:1009.0496

Phelps, S. D. 2000, Ph.D. Thesis, Princeton Univ.

Phelps, S. D., Desjacques, V., Nusser, A., & Shaya, E. J. 2006, MNRAS, 370, 1361

Reid, M. J., & Brunthaler, A. 2004, ApJ, 616, 872

Rizzi, L., Tully, R. B., Makarov, D., Makarova, L., Dolphin, A. E., Sakai, S., Shaya, E. J. 2007, ApJ, 661, 815

Roychowdhury, S., Chengalur, J. N., Chiboucas, K., et al. 2012, MNRAS, 426, 665

Rubin, V. C., & Ford, W. K., Jr. 1970, ApJ, 159, 379

Rubin, V. C., Ford, W. K. J., & . Thonnard, N. 1980, ApJ, 238, 471

Shaya, E. J., Peebles, P. J. E., Tully, R. B. 1995, ApJ, 454, 15

Schlegel, D. J., Finkbeiner, D. P., Davis, M. 1998, ApJ, 500, 525

Schönrich, R., Binney, J., & Dehnen, W. 2010, MNRAS, 403, 1829

Skrutskie, M. F., Cutri, R. M., Stiening, R., et al. 2006, AJ, 131, 1163

Tully, R. B., & Fisher, J. R. 1987, Atlas of Nearby Galaxies, (Cambridge, UK: Cambridge University Press)

Tully, R. B., Pierce, M. J., Huang, J.-S., et al. 1998, AJ, 115, 2264

Tully, R. B., Shaya, E. J., Karachentsev, I. D., Courtois, H. M., Kocevski, D. D., Rizzi, L., Peel, A. 2008 ApJ, 676, 184

Tully, R. B., Rizzi, I., Shaya, E. J., Courtois, H. M., Makarov, D., Jacobs, B. A. 2009 AJ, 138, 323

Tully, R. B. 2010, arXiv:1010.3787

van der Marel, R. P., Fardal, M., Besla, G., et al. 2012, ApJ, 753, 8

Watkins, L. L., Evans, N. W., & An, J. H. 2010, MNRAS, 406, 264

Williams, B. F. et al. 2009, AJ, 137, 419

Wilkinson, M. I., & Evans, N. W. 1999, MNRAS, 310, 645

Yun, M. S., Ho, P. T. P., Lo, K. Y. 1994, Nature, 372, 530

Yun, M. S. 1999, in IAU Symp. 186, Galaxy Interactions at Low and High Redshift, eds. J. E. Barnes & D. B. Sanders (Dordrecht: Kluwer), 81

Table 3.1. Background M/L Ratio Search

M/L	$\Omega_{\rm Smooth}$	Full <RMS(ΔV)>	Best 10 <RMS(ΔV)>	Best RMS(ΔV)	Best 10 <ΔV>
10	0.43	61.8±0.1	61.0±0.1	60.8	0.18±0.18
20	0.30	53.2±0.2	52.0±0.1	51.6	-0.33±0.32
30	0.19	49.1±0.2	47.1±0.1	46.9	-0.26±0.32
40	0.092	47.1±0.3	43.7±0.1	43.4	0.78±0.60
50	0.030	47.0±0.7	41.5±0.3	40.1	-0.55±1.0
60	0.005	50.5±1.1	41.9±0.4	40.5	-0.52±1.1
70	0	52.7±1.7	41.9±0.2	41.2	-9.34±1.3
80	0	61.0±2.3	47.7±0.3	46.0	-20.4±1.3
90	0	73.2±2.7	55.2±0.8	51.2	-31.6±1.2

Note. — Sets of trials run at the specified mass-to-light ratios M/L, using the $\Omega_{\rm Smooth}$ matter density parameter, result in three different measures of RMS(ΔV) in km s^{-1} calculated from 17 representative galaxies described in the text: mean across all 50 trials, "Full <RMS(ΔV)>", mean of the 10 best matching trials, "Best 10 <RMS(ΔV)>", and the minimum from the set, "Best RMS(ΔV)". Following these is the mean ΔV of the galaxies, calculated within a trial and then averaged across the 10 trials that have the lowest RMS(ΔV): "Best 10 <ΔV>." This statistic is used to adjust $\Omega_{\rm Smooth}$.

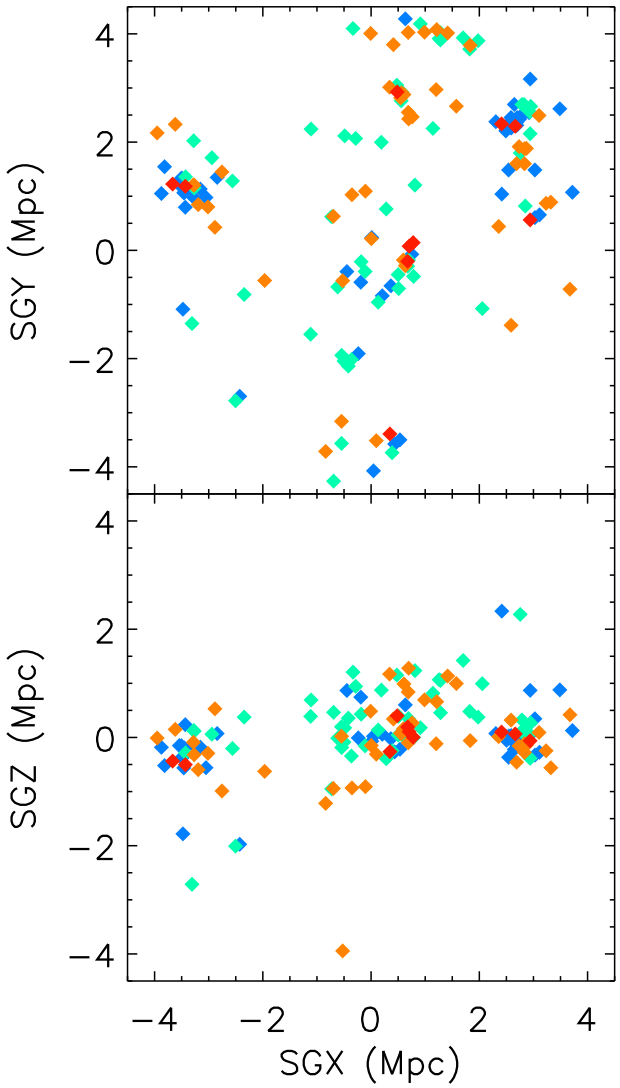

Figure 3.1 Two views of the distribution of galaxies within 4.5 Mpc in Supergalactic Cartesian coordinates. Colors represent the galaxies' peculiar velocities, Red: >100 km s^{-1}, Orange: 0 to 100 km s^{-1}, Cyan: −100 to 0 km s^{-1}, Blue: <−100 km s^{-1}.

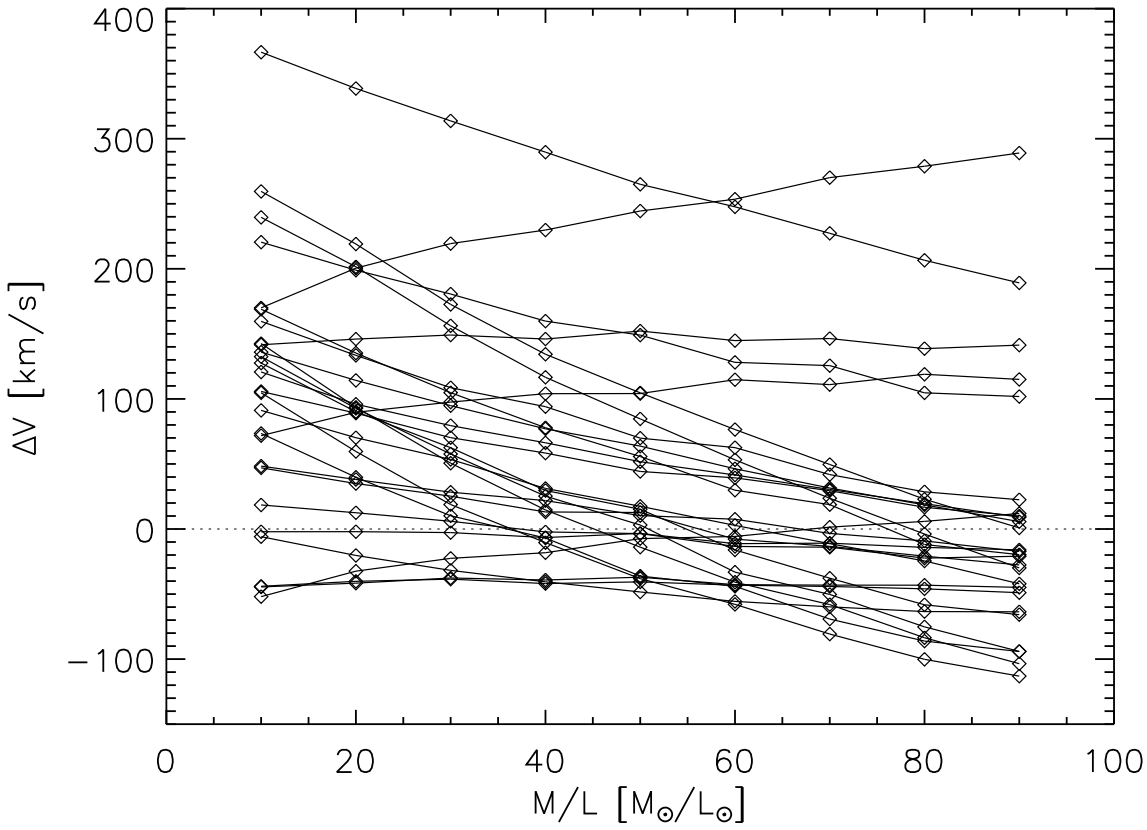

Figure 3.2 The median $\Delta V = V_{\rm Sim} - V_{\rm Obs}$ from a set of 50 trials for the 26 galaxies with $L_K > 10^{10}$ $L_\odot$ and $d < 10$ Mpc, versus input M/L. The empirical factor $\Omega_{\rm Smooth}$ is set to zero for all trials.

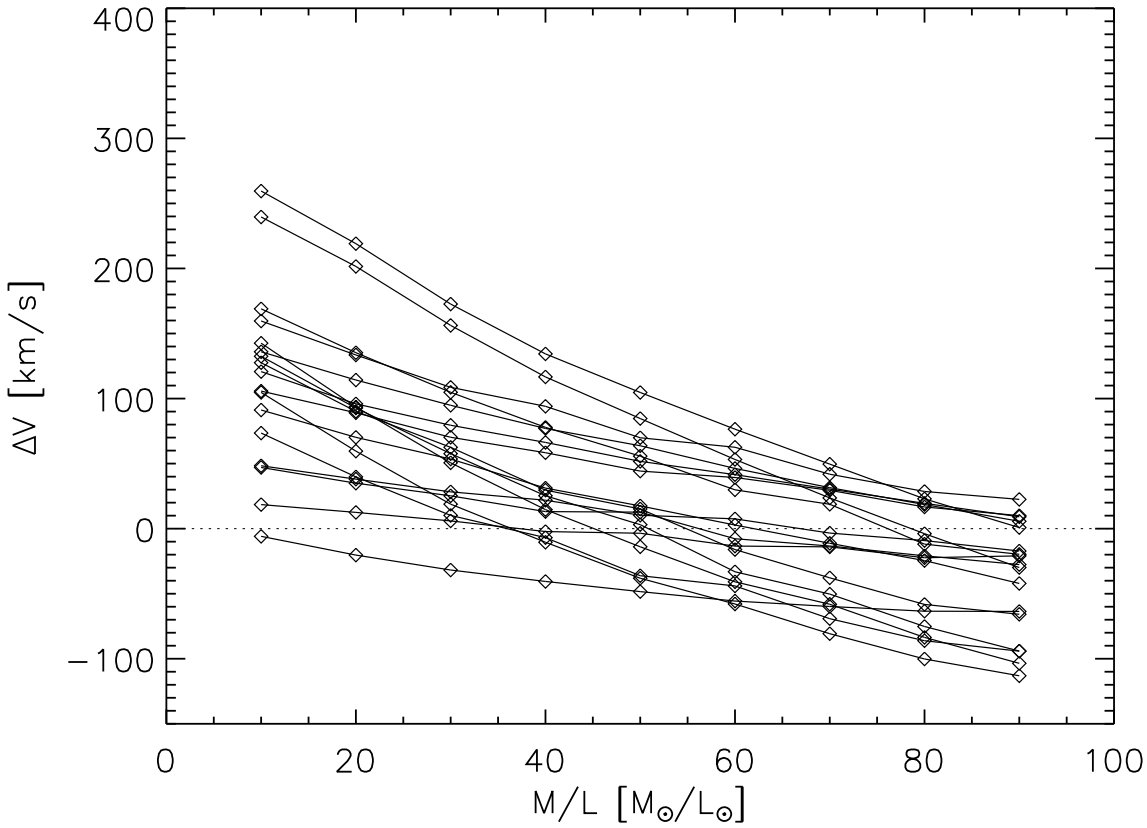

Figure 3.3 Same as Figure 3.2 except that galaxies, with rising, flat, or outlying ΔV values are excluded. The 17 galaxies that are plotted here are: M31, NGC253, M81, Maffei 1, IC342, Maffei 2, Circinus, M94, M83, NGC6946, M106, NGC2683, M51 NGC2903, M63, NGC891, and NGC1023.

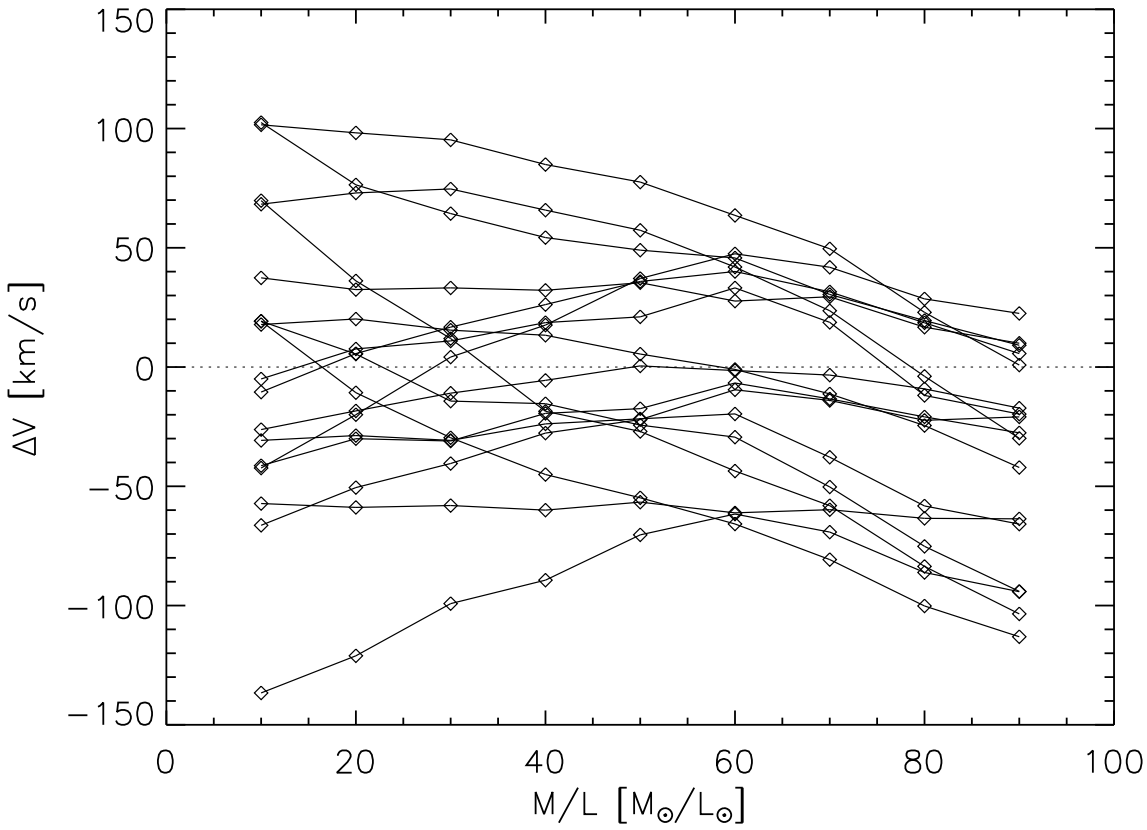

Figure 3.4 Same as Figure 3.3 except that $\Omega_{\rm Smooth}$ has been iteratively adjusted so that the mean ΔV from the 17 test galaxies is consistent with zero.

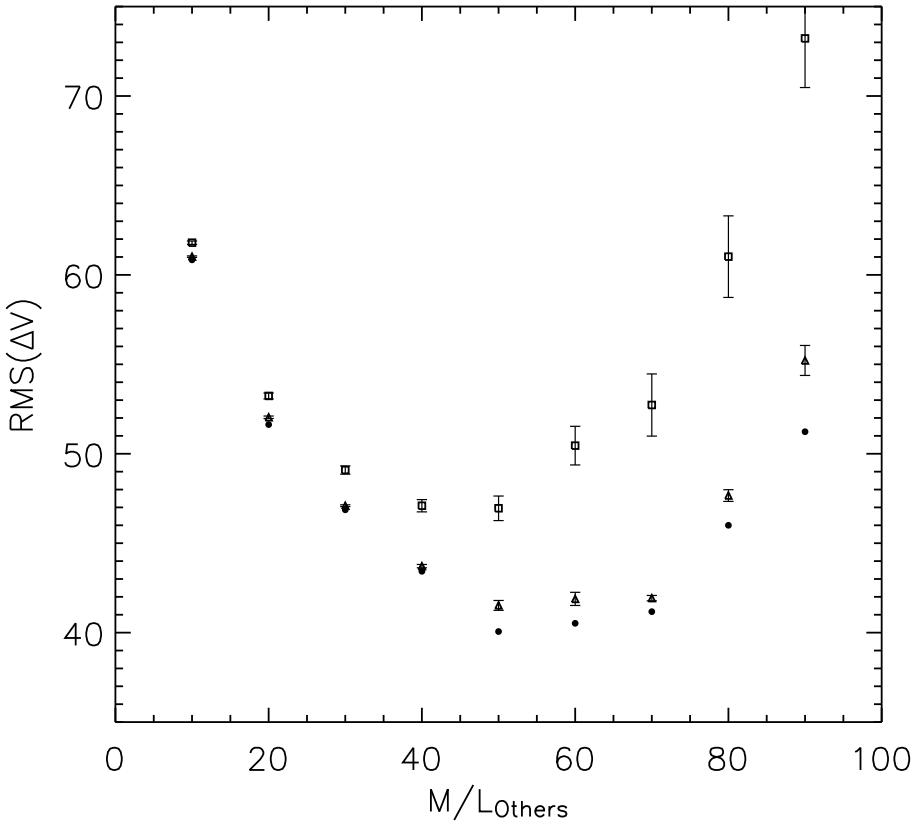

Figure 3.5 Three representations of RMS(ΔV) of the 17 test galaxies versus input mass-to-light ratio. The dots represent the minimum RMS(ΔV) taken from a set of 50 trials, the triangles represent the mean of the 10 best matching RMS(ΔV) values from those sets, while the squares represent the mean across all 50 trials.

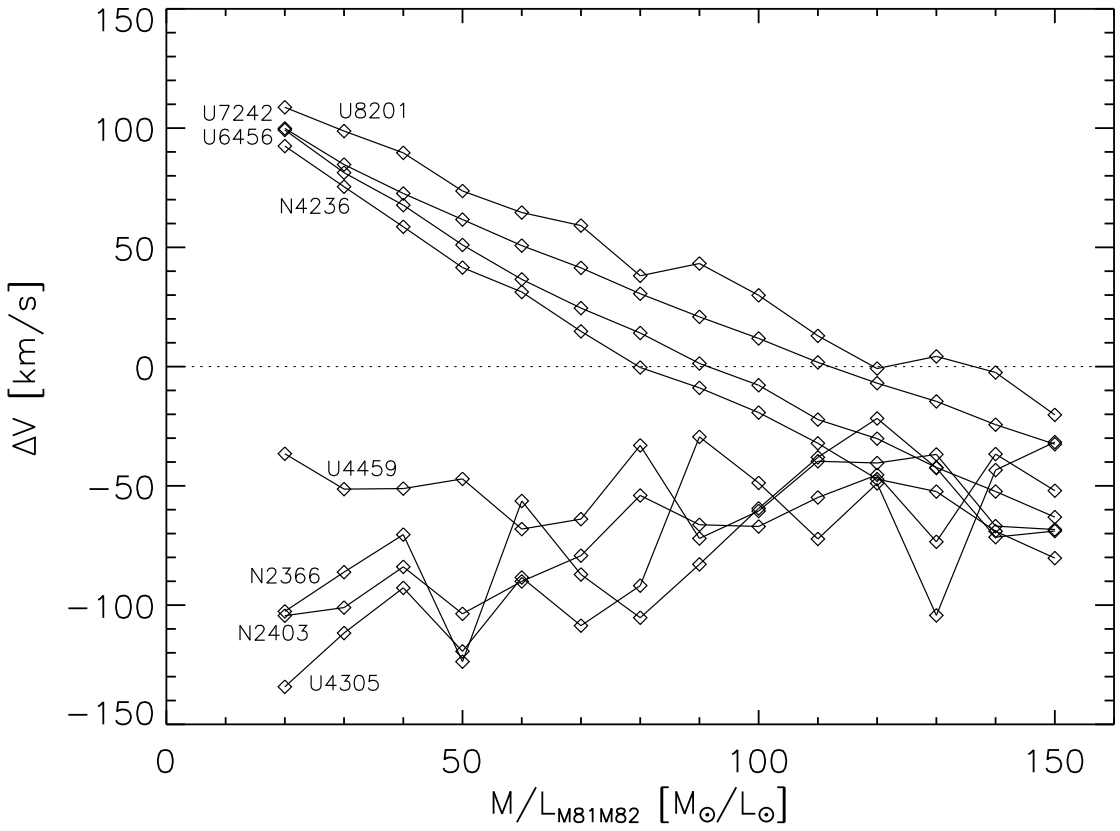

Figure 3.6 The median $\Delta V = V_{\rm Sim} - V_{\rm Obs}$ versus input $M/L_{\rm M81M82}$ from a set of 50 trials for the galaxies: NGC4236, UGC6456, UGC8201, UGC7242, NGC2403, NGC2366, UGC4305, and UGC4459.

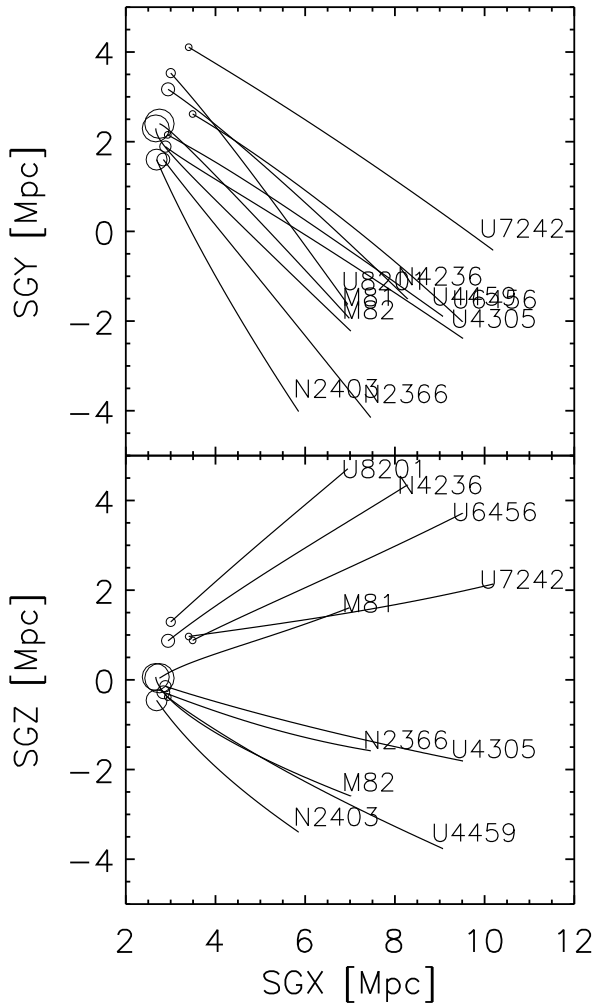

Figure 3.7 Example orbital paths, showing the current positions of M81 and the galaxies chosen to trace the mass of the M81 group: NGC4236, UGC6456, UGC8201, UGC7242, NGC2403, NGC2366, UGC4305, and UGC4459 in Supergalactic Cartesian coordinates.

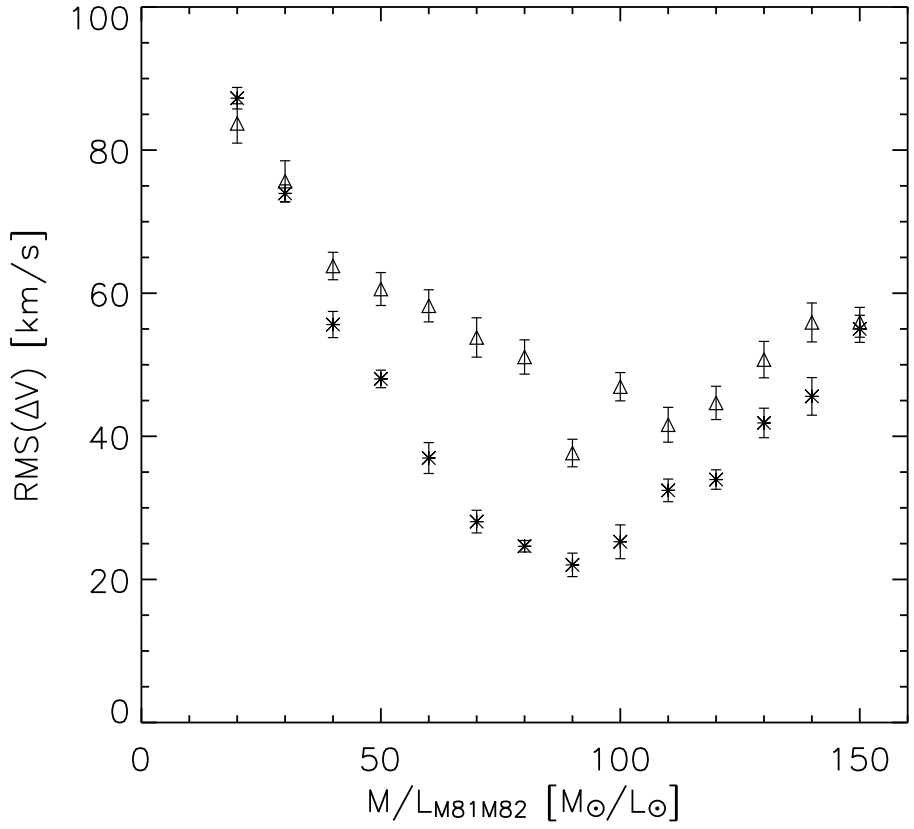

Figure 3.8 RMS(ΔV) of galaxies used to trace M81 group mass versus input mass-to-light ratio of M81 and M82 (all other galaxies have a fixed value of $M/L_{\rm Others} = 60$). These values are calculated by taking the mean of the 10 lowest RMS(ΔV) from a set of 50 trials at a particular mass ratio, using the following tracer galaxies: triangles use NGC4236, UGC6456, UGC8201, UGC7242, NGC2403, NGC2366, UGC4305, and UGC4459, while the stars use NGC4236, UGC6456, and NGC2403.

Chapter 4

The Star Formation History of Isolated Dwarf UGC4879

Note: This chapter originally appeared as Jacobs et al. (2011), with co-authors Bradley A. Jacobs, R. Brent Tully, Luca Rizzi, Igor D. Karachentsev, Kristin Chiboucas, and Enrico V. Held.

Abstract

Recent observations of UGC4879 with the Advanced Camera for Surveys on the Hubble Space Telescope confirm that it is a nearby isolated dwarf irregular galaxy. We measure a distance of 1.36 ± 0.03 Mpc using the Tip of the Red Giant Branch method. This distance puts UGC4879 beyond the radius of first turnaround of the Local Group and $\sim$700 kpc from its nearest neighbor Leo A. This isolation makes this galaxy an ideal laboratory for studying pristine star formation uncomplicated by interactions with other galaxies. We present the star formation history of UGC4879 derived from simulated color-magnitude diagrams.

4.1 Introduction

The terms used to describe the environmental influence on the gas in a modest-sized galaxy found in a cluster invoke an existence that is permeated by violence. A galaxy might lose gas through stripping, harassment, strangulation, or a combination of these or other forces. Even the relatively quiet neighborhood of the Local Group "is a dangerous place for dwarf galaxies" (Mateo 1998) and processes involving gas must, in many cases, be studied in the context of galaxy-galaxy interactions.

These interactions add to the complexity of a galaxy's star formation history (SFH). Regardless of whether tidal interactions are a concern, nearly all Local Group dwarfs have been the subject of SFH studies (e.g. Tolstoy et al. 2009, and references therein) since their proximity makes it possible to resolve stellar populations inaccessible at greater distance. The proximity and relative isolation of UGC4879 (VV124) make it an extremely attractive target for this type of study. Here we present new observations of UGC4879 with the Advanced Camera for Surveys (ACS) on the Hubble Space Telescope and use these to construct its SFH.

Kopylov et al. (2008) resolved stars in UGC4879 from ground-based observations and concluded that it is on the periphery of the Local Group. Before that, distance estimates were based on radial velocity information and tended to be erroneously high due to a value of $v_h = 600 \pm 100$ km s^{-1} assigned to it in Huchra et al. (1983). As a result, UGC4879 did not receive much attention until recently. In a followup to their 2008 paper the team in Russia extend their analysis to include spectroscopy of the unresolved stellar population and diffuse gas to confirm their measurement of $v_h = -70 \pm 15$ km s^{-1} (Tikhonov et al. 2010). Observations of HI with the Westerbrok Synthesis Radio Telescope measure a gas velocity of $v_h = -27 \pm 2$ km s^{-1} (Oosterloo, private communication). We use our ACS observations of UGC4879 to extend the analysis of this galaxy. In the next section we describe the data and reduction procedures. From these data we derive a new distance measurement, and metallicity estimate. Incorporating these results, we simulate the observed color-magnitude diagram (CMD) in order to reconstruct the SFH of UGC4879. The process used to obtain the SFH is described in §5 and our interpretation is given in §6.

4.2 ACS Data and Photometry

Observations of UGC4879 were carried out with ACS on February 21, 2010 in the $F606W$ and $F814W$ filters with exposures totaling 1140 s in each. A psuedo-color image of the central portion of the ACS image created from the combined $F606W$ and $F814W$ observations is displayed in Figure 4.1. We generate a stellar photometry catalog from the procedures described in Jacobs et al. (2009). In brief, we use the ACS module of the DOLPHOT software package[1] to photometer the images as well as run artificial star tests to characterize the completeness and uncertainty in the measurements. From the results of these analyses we plot the CMD in $F606W - F814W$ vs. $F814W$, see Figure

[1]By Andrew Dolphin, http://purcell.as.arizona.edu/dolphot

4.2. This diagram and all the analyses that follow are based on data within the aperture of the green circle shown in Figure 4.1, which is applied to reduce contamination from foreground stars.

4.3 TRGB Distance

We use a maximum-likelihood method from Makarov et al. (2006) to measure the magnitude of the Tip of the Red Giant Branch (TRGB) in UGC4879, and find $F814W_{\rm TRGB} = 21.63 \pm 0.03$. Following the zero-point calibration of the absolute magnitude of the TRGB developed by Rizzi et al. (2007), we calculate $M_{814}^{\rm TRGB} = -4.07 \pm 0.03$. Using these values and accounting for foreground reddening of $E(B-V) = 0.015$ from Schlegel et al. (1998) we measure a distance of $(m-M)_0 = 25.67 \pm 0.04$ or 1.36 ± 0.03 Mpc. Further details of this distance measurement technique are available in Jacobs et al. (2009). Using this distance modulus with the apparent magnitude of UGC4879 of $B = 13.68$ (Taylor et al. 2005) gives a (reddening corrected) luminosity of $M_B = -12.06$.

This distance is somewhat greater than the TRGB distance calculated from ground-based observations by Kopylov et al. (2008), and puts UGC4879 just beyond the in-fall region of the Local Group rather than just within it, as they suggested. The location of UGC4879 is plotted in Supergalactic Cartesian coordinates with reference to other nearby galaxies in Figure 4.3. It is about equidistant from the Milky Way and M31 (1.38 Mpc), while more distant from other large nearby galaxies IC342 and M81 at 1.5 and 2.4 Mpc, respectively. The galaxy closest to UGC4879 is Leo A, which at a separation of about 700 kpc is located on the other side of the Local Group zero-velocity surface. This isolation indicates that its existence has been free of the type of interactions with other galaxies that could affect its SFH.

4.4 Metallicity

In addition to its usefulness as a distance indicator, the RGB can be used to estimate metallicity. Our technique is based on comparing the color of the RGB stars in UGC4879 with the fiducial loci of the RGBs of the galactic globular clusters (GGCs) from Da Costa & Armandroff (1990). Figure 4.4 shows the RGB of UGC4879 in $(V-I)_0$ vs M_I plot with the Da Costa & Armandroff loci. After correcting for foreground reddening we calculate the mean color difference between the RGB stars and the loci of the GGCs. We then fit a quadratic function to these resulting color differences versus

the GGC metallicities. The best fitting relation is:

$$[\mathrm{Fe/H}] = -4.93 \times \delta(\mathrm{V-I})_0^2 - 5.34 \times \delta(\mathrm{V-I})_0 - 1.79 \tag{4.1}$$

with an rms of 0.05, so we take the mean metallicity of the RGB to be [Fe/H]$=-1.79 \pm 0.05$. Metallicity estimates based on a sample of GGCs require that the observed population have ages comparable to the clusters, i.e. ancient stars. In order to test this assumption with UGC4879 we generate a series of test SFHs using the methods described below, and a variety of metallicities ranging [Fe/H]=-2.0 to -0.5 and find that they consistently include large numbers of stars with ages greater than 10 Gyr. Moreover, a star's position on the RGB is more sensitive to metallicity than age, for example an age difference of several Gyr is needed for two stars to occupy the same space on the RGB when they have a metallicity difference of order 0.1 dex (e.g. Held et al. 2010).

The GGC based value is in agreement with a metallicity estimate that depends on the I-band magnitude of the red clump and the distance to UGC4879 using the technique of Udalski (2000), which uses the LMC for calibration. Both measurements of the magnitude of stars in the RGB or in the red clump will be sensitive to old stars that are likely to have lower metallicities than younger generations of stars in the galaxy. Hence the metallicity value quoted here should be considered an estimate of the initial metallicity rather than a global average. In fact, as is discussed below, for the case of UGC4879 the presence of blue-loop stars on the CMD indicate recent star formation activity which is best fit with metallicities up to one dex higher than the RGB value quoted here.

4.5 Star Formation History

We attempt to reconstruct the SFH of UGC4879 by simulating a CMD that matches the populations visible in the observed diagram. The technique we use is based on the Padova evolutionary tracks (Bertelli et al. 1994; Girardi et al. 2000) and takes a number of quantities, including the initial mass function, the galaxy distance, and the reddening as input parameters. The chemical evolution history (CEH), which is also taken as an input, is adjusted iteratively between runs to match the observed CMD as well as the metallicity information described above. Within a single run these inputs are used to generate a set of single-age synthetic stellar populations (age bins with widths between 0.5 and 4 Gyr) using the isochrones. Photometric errors and completeness functions are

applied to the synthetic stellar populations using the results of artificial star tests produced with DOLPHOT. We then produce a single multi-epoch CMD designed to match the observed CMD by drawing varying numbers of these degraded stars from the set of single-age populations. The relative number of stars taken from the different age bins to match the observed CMD in turn yields the SFH.

The method for choosing how many simulated stars are needed from each age bin to recreate the observed CMD involves minimizing the differences in star counts between the observed and the simulated CMDs within pre-defined regions on the diagrams. This minimization procedure is multidimensional and utilizes an Amoeba-style algorithm. In order to increase the efficiency of this procedure and to reduce the likelihood that the resulting SFH represents a local minimum, the initial mix of stars is user-defined. In practice, we find that the final SFH produced from a given set of input parameters converges fairly robustly even when starting from significantly divergent conditions such as a constant, continually increasing, or continuously decreasing star formation rate. Furthermore, even a somewhat cursory look at a CMD yields information about the presence of young and old populations, so the job of the algorithm is to refine an initial mix that will usually be quite close to the final solution.

The errors in the SFH are measured in two ways. A first estimate is given by the minimization algorithm itself, and is based on the 99% confidence level of the minimum. This is a lower limit to the actual errors, because it does not take into account the effect of the many random extractions that are part of the procedure. The error contribution due to differences between subsets of synthetic stars drawn from a population that includes variations due to stellar evolution, photometric errors, and completeness limits, among others, can be quite large. This issue becomes particularly important when matching populations of stars that exist in very low numbers on the observed CMD, such as the upper main sequence. To measure these effects, we also perform a bootstrap procedure that involves repeating the entire procedure 100 times. The final SFH is the average of the 100 repetitions, and the error is the rms of the star formation rate within each bin. It is always the case that the bootstrap error is much larger than the minimization error.

4.5.1 CMD Regions

The predefined regions used in the minimization algorithm are selected by hand to encompass stars in various evolutionary phases. Figure 4.5 shows the observed CMD in $(V - I)$ vs V with the

regions plotted as boxes. Boxes 1-4 mark the the main sequence stars and we attempt to include a statistically significant number of stars in each box. Boxes 5 and 6 encapsulate samples of RGB stars. Since the RGB includes stars of a wide range of ages, the large sample of the RGB helps to normalize the overall star formation within the galaxy. Box 7 encloses the region where the Asymptotic Giant Branch (AGB) would be located. The relatively low number of stars observed in this region serves to constrain the number of intermediate aged stars produced in our simulations. Finally, in Box 8 we note the presence of blue-loop stars, which along with the high-luminosity main sequence are tracers of recent star formation.

4.5.2 Chemical Evolution History

As an initial guess at the CEH of UGC4879 we simulate its SFH using a constant value of [Fe/H]$= -1.8$ and note which age bins show star formation activity. From this first step we refine the CEH by requiring that eras that show significant star formation rates have a parallel increase in metallicity. We take the RGB metallicity as measured above to be near the initial value for the galaxy. For an endpoint metallicity at recent times we find that the location of the blue-loop stars provides a constraint. The distribution of lower luminosity blue-loop stars between the RGB and main sequence varies as a function of metallicity. Figure 4.6 shows a series of simulated CMDs of young (<500 Myr) stars where metallicity is fixed in a given panel but varies between panels. The distribution of these lower luminosity blue-loop stars in UGC4879 (see Figure 4.5) appears to fall between those with [Fe/H]$= -1.0$ and [Fe/H]$= -0.5$ (lower panels of Figure 4.6), hence we take the metallicity of young stars in UGC4879 to be [Fe/H]≈ -0.7.

With constraints on the endpoint metallicities of the CEH, the next area of focus becomes the nature of the increase in metallicity between these ancient and recent values. The width of the RGB provides some information about this increase. Although the RGB may be populated by stars of many ages, the simulations that best represent the observed CMD tend to have RGBs that are dominated by old stars. If this is the case then the metallicity of UGC4879 must increase relatively rapidly at early times in order to account for the intrinsic width of the RGB. Unfortunately, these data do not allow us to resolve the details of this initial star formation activity, and we note only that our simulations consistently fit the data best when we include a significant amount of star formation in the first 4 Gyr following the Big Bang. These old stars would make up the dominant population

of the RGB, and its intrinsic width is best matched with a range of metallicities of around 0.6 dex in extent.

Accounting for each of these constraints, we utilize the CEH in Figure 4.7 to study the SFH of UGC4879. The best fitting SFH using this CEH is shown in Figure 4.8 and the resulting simulated CMD is shown in comparison with the observed CMD in Figure 4.9. We work iteratively to find a CEH and SFH that are consistent with each other and together produce a simulated CMD that matches the observed. The best matches consistently involve a CEH with (Age, [Fe/H]) at around (14 Gyr, -1.8), (10 Gyr, -1.2), and (0 Gyr, -0.7), unfortunately beyond these three estimates we lack constraints on the CEH. One possible scenario would be that the metallicity remains flat from 10 until 1 Gyr ago, followed by a rapid increase in the last Gyr. At the opposite extreme would be a steadily increasing metallicity between 10 Gyr and today. Neither of these CEHs produce good matches with the data, but the CEH shown in Figure 4.7, which is intermediate between these extremes yields results that fit the data well. Beyond this, the exact details of the CEH that we assign for ages 1-10 Gyr are not crucial because our observations are not sensitive to stars of these ages.

4.5.3 Spatially Resolved Star Formation

While we are interested in the SFH of UGC4879 as a whole, it shows signs of spatial variation in recent star formation. Inspection of the distribution of stars in Figure 4.1 shows that bright main sequence stars (bluish in this psuedo-color image) are highly localized. This distribution is shown in Figure 4.10 where the locations of upper main sequence stars ($I < 24$) are shown as blue triangles and the locations of upper RGB stars are shown as red dots. The vast majority of the young stars, as denoted by the blue triangles, are located in a region enclosed by a set of line segments in the plot. The areas of the regions within and outside these lines are 1603, and 3424 arcsec^2 respectively, which at a distance of 1.36 Mpc correspond to physical areas of 7.0×10^4, and 1.5×10^5 pc^2. The left panels in Figures 4.11 & 4.12 show the CMDs of stars in the inner and outer regions. Blue-loop and upper main sequence stars are nearly lacking from the CMD of the outer region, indicating that recent star formation has been weak or nonexistent here. In contrast, the CMD of the inner region contains all the populations that are seen in UGC4879 as a whole. The right panels of these figures display the simulated CMDs generated in the process of developing separate SFHs for these regions. These SFH diagrams for the inner and outer regions are presented in Figures 4.13 & 4.14. The star

formation rates presented in these diagrams, as well as those measured for the entire galaxy (Figure 4.8) are listed in Table 4.1.

4.6 Discussion

The observed CMD of UGC4879 is characterized by two distinct populations, old stars that populate the RGB with a small representation in the AGB, and young stars that make up the main sequence, blue loop, as well as contribute to the RGB, red clump and AGB. Just how old the older stars are remains somewhat uncertain, because we do not observe the main sequence turnoff, hence cannot claim to detect an unequivocally ancient population. The best matching SFHs consistently show significant star formation in the first 4 Gyr after the Big Bang and then a relative lull for 9 Gyr until 1 Gyr ago after which star formation is measurable again.

4.6.1 Stellar Ages > 1 Gyr

A question is: how significant is the 9 Gyr lull in star formation? As mentioned above, the minimization algorithm used to define the SFH in UGC4879 takes an initial input that is user-defined. Therefore, one way to test the significance of the relative lack of star formation at intermediate ages is to insert a star formation rate at these ages and see how things change. Of course, doing so increases the total number of simulated stars on the CMD, so an insertion of intermediate age stars must be matched by a decrease in the star formation rate at a different age, in this case that decrease would occur in the 10-14 Gyr bin. The results from the minimization algorithm are robust under this scenario. Any insertion of stellar populations with ages between 1 and 9 Gyr gets adjusted by the algorithm to give a star formation rate at these times that is consistent with zero. This is because the number of simulated and observed stars in the various boxes on the CMD shown in Figure 4.5 is matched more closely when the star formation is shifted away from these ages and into the 10-14 Gyr bin. While it is comforting that our routine consistently reaches the same minimum, this is not an entirely satisfactory justification for the lull in star formation. How exactly does the match improve with the exclusion of intermediate aged stars? The key distinction comes from the number of AGB stars produced in the simulated CMD.

At the depth of our observations there are only two stellar types distinguishable for stars with ages over 1 Gyr, those that make up the RGB and the AGB. The relative numbers of these stars are

sensitive to age, as the AGB stars evolve more quickly than those on the RGB. In Figure 4.15 we plot the ratio of the number of AGB to RGB stars (requiring RGB stars to be within 2 magnitudes of the TRGB to avoid confusion with other populations) versus age for simulated stars in 2 Gyr age bins. The ratio calculated from the CMD of UGC4879 is shown as a horizontal line[2] for an AGB to RGB ratio of 0.047 ± 0.005. As is expected, the general trend is that the ratio increases with time and depends fairly weakly on metallicity. The various symbols in Figure 4.15 represent fixed metallicities at [Fe/H]$= -2.0, -1.5, -1.0$, as well as the value of -1.8 based on the comparison of UGC4879 with GGCs (shown as filled diamonds). At any given time the AGB/RGB ratio is generally higher for lower metallicities, though in many cases the values are statistically indistinguishable. We take the measured metallicity of the RGB in UGC4879 to be valid for comparing these populations. If this is the case, then the SFH measured at ages of 10-14 Gyr is justified by the match in AGB/RGB ratios at these times. This scenario is of course an over simplification, since for instance we see evidence for a range of metallicities in the intrinsic width of the RGB of UGC4879. Nonetheless, the clear age evolution of the AGB/RGB ratio for fixed metallicities explains why the match to the simulations requires an early epoch of strong star formation followed by a long period of low-to-negligible star formation in UGC4879.

Figure 4.15 also shows that the AGB/RGB ratio for stars older than 10 Gyr with a metallicity of [Fe/H]$= -1.8$ is consistent with the value observed in UGC4879. This metallicity corresponds to what was measured in the RGB of UGC4879 by comparing these stars with those in GGCs. We present our SFH results in a combined 10-14 Gyr bin because these observations and simulations lack the resolution needed to distinguish between multiple short bursts or moderate continuous star formation at these early times.

Though the AGB and RGB provide the bulk of the information on older populations observed in UGC4879, another aged population, the Horizontal Branch (HB) falls above the detection limits. As shown in the upper panels of the zoomed CMDs in Figures 4.9, 4.11, & 4.12 there is a high number of stars with $M_V \sim 0.5$ and $(V-I)_0 \sim 1.0$ observed in UGC4879. This location corresponds to the magnitude of the HB and red clump, and most likely a mix of the two is contributing to the over-density in points, with the red clump stars extending to slightly brighter magnitudes. The

[2]For UGC4879 $I_{\rm TRGB} = 21.64$, so we require $I < 21.64$ for AGB stars and $21.64 \leq I < 23.64$ for RGB stars included in the ratio. In addition we apply color cuts based on visual inspection: for the AGB we require $(V-I) > 1.1$ and for the RGB we use linear limits, which when written as functions have the form: $I < -4.444 \times (V-I) + 27.444$ and $I > -4.444 \times (V-I) + 29.889$.

lower panels of these zoomed CMDs show the distribution of the simulated stars that make up the HB and red clump. The simulated HB stars extend blue-ward to about $(V-I)_0 \sim 0.4$, while the corresponding stars in the observed CMD appear to have a more limited color range. We have not been able to find a completely satisfactory match between the observed and simulated stars at these magnitudes. We expect that the lack of a good match here is due to photometric errors and completeness starting to play a role in the detections, as well as that the SFH codes are unable to provide a complete picture of the HB, which represents an extremely complex stage of stellar evolution. Despite some clear differences, the CMDs of the observed and simulated stars at these magnitudes are *not* wildly discrepant, and thus, while we are unable to glean additional information about the SFH here, the interpretations of other populations hold.

4.6.2 Stellar Ages < 1 Gyr

The situation is clearer at recent times. The bright main sequence and blue-loop stars observed in UGC4879 formed within the last 500 Myr. The simulations also favor star formation between 500 and 1000 Myr ago, which apparently serves to populate the red clump. The most recent star formation activity is confined to the central region of the galaxy as demonstrated by the difference in star formation rates in the 0-0.5 Gyr bin of Figures 4.13 & 4.14. Recent studies of the SFH of nearby dwarfs have analyzed recent star formation in much finer resolution than 500 Myr (e.g. McQuinn et al. 2010), but we find that the coarser 500 Myr bins are sufficient for our purposes of localizing the area of active star formation in UGC4879. We note also, that UGC4879 has been detected in Hα, which yields an current star formation rate of 40 ± 20 M$_\odot$ Myr^{-1} (James et al. 2004). HI observations of UGC4879, infer a gas mass of 1.07×10^6 M$_\odot$ (Oosterloo, private communication) and the peak of the HI emission overlaps with this region of active star formation.

4.6.3 UGC4879 In Context

As would be expected for an isolated galaxy UGC4879 has not been stripped of its gas through interactions. Its gravitational potential well is also apparently deep enough to prevent losses due to galactic winds. This is not a forgone conclusion, as evidenced by KKR25 (LEDA 2801026), which is another fairly isolated galaxy at a distance of 1.91 ± 0.06 Mpc (see Figure 4.3) with a B-band

absolute magnitude of $M_B = -10.0$ (Karachentsev et al. 2004), but has a CMD[3] that shows no signs of recent star formation. Begum & Chengalur (2005) do not detect KKR25 in HI and list a 5σ upper limit mass of $<8 \times 10^4$ $M_\odot$. This mass limit is consistent with other properties that point toward classifying KKR25 as a dwarf spheroidal galaxy (Grebel et al. 2003). So it could be that it lost its gas through galactic winds, which has been suggested as the key mechanism in other isolated dwarf spheroidals (e.g. Young et al. 2007). Another example of a nearby isolated dwarf without recent star formation is Tucana[4], which is located at a distance of 920 kpc from the Milky Way, has a luminosity $M_B = -9.25$ (Karachentsev et al. 2004), and no detected HI (Oosterloo et al. 1996). Bernard et al. (2008) observe ancient (> 10 Gyr) populations in Tucana and find no evidence for star formation in the last $\sim$8 Gyr. It and KKR25 have SFHs that resemble that of UGC4879, except that they have no recent episodes of star formation. Both KKR25 and Tucana are less luminous than UGC4879, but some of this difference is due to their lack of young massive stars. Neither Tucana, KKR25 nor UGC4879 have close neighbors so the differences between their SFHs should be independent of environment. UGC4879 would resemble the other two except, presumably, a higher mass has allowed UGC4879 to retain its gas and continue forming stars.

Unlike in Tucana and KKR25, HI is securely detected in UGC4879 and the contours extend well beyond the optical extent of the galaxy, possibly indicating that some gas outflow may have occurred. Tikhonov et al. (2010) also express the possibility that the HI gas is a 'primodial cloud' interacting with UGC4879. The abrupt edge to the region of star formation running from eight o'clock to two o'clock in Figure 4.1 is suggestive of a galaxy scale compressive event. If this is the case then this event would likely be the cause of the recent star formation. However, if the relatively high metal content estimated in these young stars is accurate then it is doubtful that primordial gas could be the trigger for their formation. Nevertheless, a galaxy as isolated as UGC4879 could accrete gas during its lifetime. It is possible that much of the gas involved in the current star formation could be native to UGC4879 and enriched and the compression from an external cloud might act as a trigger for the collapse of this gas. The exact nature of the large scale gas dynamics and its affect on star formation in UGC4879 remains to be clarified. While a lack of galaxy-galaxy interactions frees UGC4879 from some of the manifold factors that can influence SFHs, the galaxy itself contributes ample complexity to the problem.

[3]The CMD of KKR25 is available through the Extragalactic Distance Database (Jacobs et al. 2009), see: http://edd.ifa.hawaii.edu/LV/KKR25/2801026info.html

[4]For CMD of Tucana see: http://edd.ifa.hawaii.edu/LV/Tucana/69519info.html

References

Begum, A., Chengalur, J. N. 2005 MNRAS, 362, 609

Bernard, E. J., et al. 2008, ApJ, 678, L21

Bertelli, G., Bressan, A., Chiosi, C., Fagotto, F., Nasi, E. 1994, AAPS, 106, 275

Da Costa, G. S., Armandroff, T. E. 1990, AJ, 100, 162

Girardi, L., Bressan, A., Bertelli, G., Chiosi, C. 2000, AAPS, 141, 371

Grebel, E. K., Gallagher, J. S., Harbeck, D., 2003, AJ, 125, 1926

Held, E. V., Gullieuszik, M., Rizzi, L., Girardi, L., Marigo, P., Saviane, I. 2010 MNRAS, 404, 1475

Huchra, J., Davis, M., Latham, D., Tonry, J. 1983 ApJS, 52, 89

Huchtmeier, W. K., Karachentsev, I. D., Karachentseva, V. E. 2003, A&A, 401, 483

Jacobs, B. A., Rizzi, L., Tully, R. B., Shaya, E. J., Makarov, D. I., Makarova, L. 2009, AJ, 138, 332

Jacobs, B. A., Tully, R. B., Rizzi, L., Karachentsev, I. D., Chiboucas, K., Held, E. V. 2011, AJ, 141, 106

James, P. A., et al. 2004, A&A, 414, 23

Karachentsev, I. D., Karachentseva, V. E., Huchtmeier, W. K., Makarov, D. I. 2004, AJ, 127, 2031

Kopylov, A. I., Tikhonov, N. A., Fabrika, S., Drozdovsky, I., Valeev, A. F. 2008, MNRAS, 387, L45

Makarov, D., Makarova, L., Rizzi, L., Tully, R. B., Dolphin, A. E., Sakai, S., Shaya, E. J. 2006, AJ, 132, 2729

Mateo, M. 1998, ARA&A, 36, 435

McQuinn, K. B. W., et al. 2010 arXiv/1008.1589

Oosterloo, T., Da Costa, G. S., Staveley-Smith, L. 1996, AJ, 112, 1969

Rizzi, L., Tully, R. B., Makarov, D., Makarova, L., Dolphin, A. E., Sakai, S., Shaya, E. J. 2007, ApJ, 661, 815

Schlegel, D. J., Finkbeiner, D. P., Davis, M. 1998, ApJ, 500, 525

Taylor, V. A., Jansen, R. A., Windhorst, R. A., Odewahn, S. C., Hibbard, J. E. 2005, ApJ, 630, 784

Tolstoy, E., Hill, V., Tosi, M. 2009, ARA&A, 47, 371

Tikhonov, N. A., Fabrika, S. N., Sholukhova, O. N., Kopylov, A. I. 2010, AstL, 36, 309

Udalski, A. 2000 Acta Astron., 50, 279

Young, L. M., Skillman, E. D., Weisz, D. R., Dolphin, A. E. 2007, ApJ, 659, 331

Table 4.1. Star Formation Rates

Age Bins (Gyr)	Full Aperture	Inner Region	Outer Region
0−0.5	303±23	220±20	44±10
0.5−1	1290±92	456±55	579±64
1−2	0+69	0+45	0+50
2−4	0+70	7+47	0+46
4−6	0+103	4+81	16+86
6−8	0+197	0+112	2+127
8−10	0+211	12+152	32+183
10−14	2640±139	1054±89	1438±103

Note. — The absolute star formation rates in $M_\odot$ Myr^{-1} presented in Figures 4.8, 4.13, & 4.14 for the full aperture (Figure 4.1) and for the inner and outer regions (Figure 4.10) of UGC4879. The areas of the full, inner, and outer regions are 5027, 1603, and 3424 $arcsec^2$, respectively and correspond to physical areas of 2.2×10^5, 7.0×10^4, and 1.5×10^5 pc^2. In age bins where the star formation rate is consistent with zero we present the upper limits and denote these as e.g. 0+69.

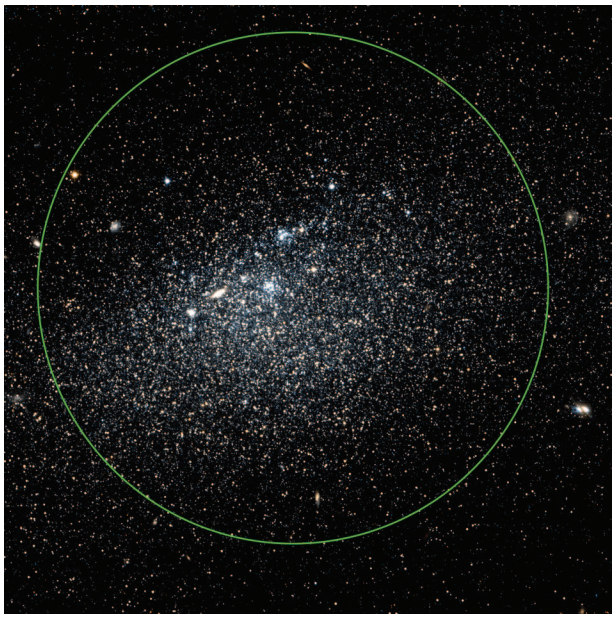

Figure 4.1 Pseudo-color image of UGC4879 produced from $F606W$ and $F814W$ filters. The green circle denotes the aperture within which stars were treated as members of UGC4879 for the purposes of comparison with simulated CMDs.

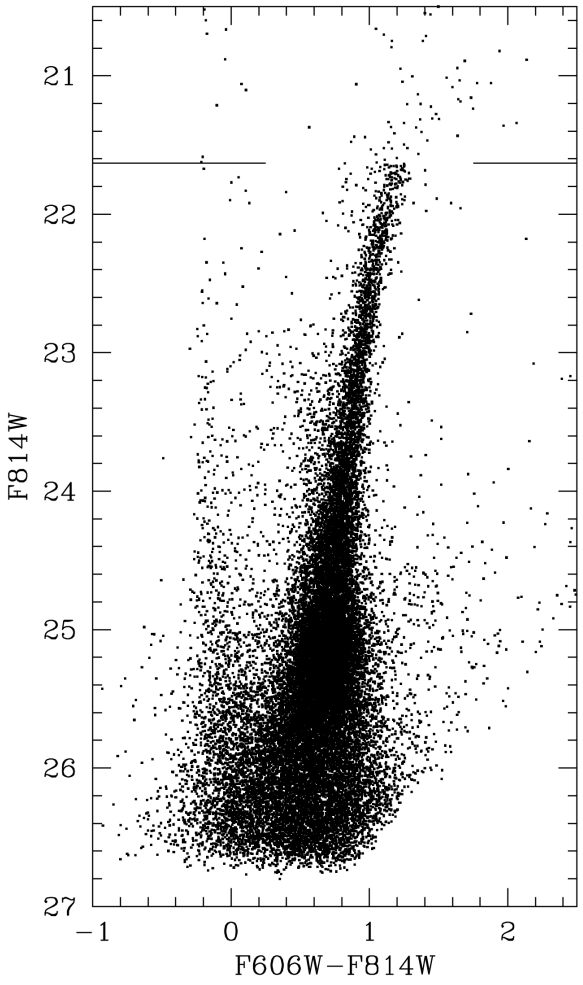

Figure 4.2 CMD of UGC4879 in $F606W - F814W$ versus $F814W$ constructed from ACS observations. The broken horizontal line at $F814W = 21.63$ marks the magnitude of the TRGB.

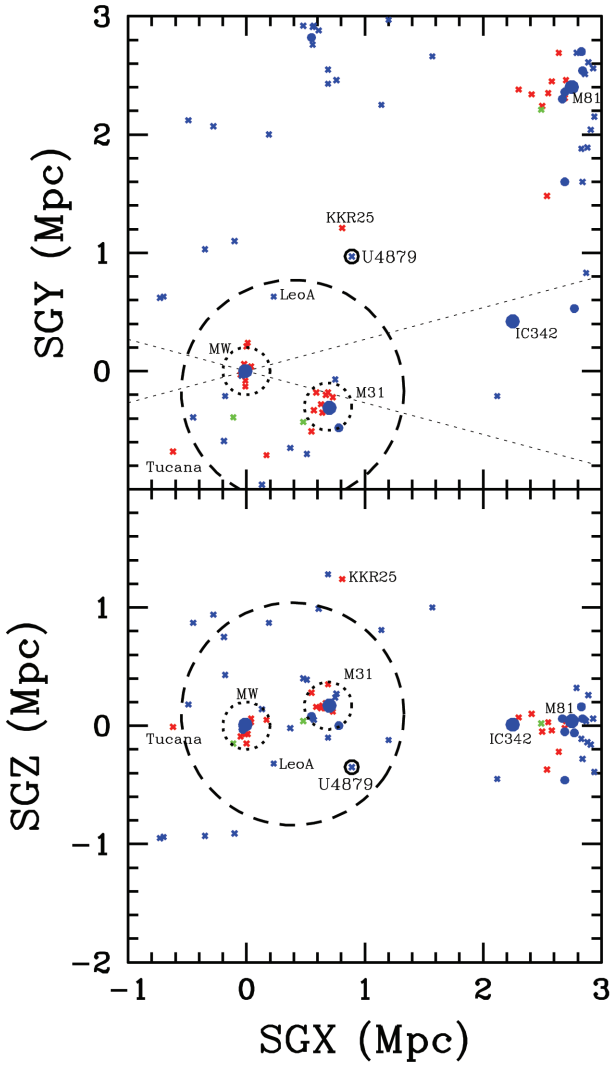

Figure 4.3 Distribution of nearby galaxies in Supergalactic Cartesian coordinates in Mpc. The galaxy symbols used depend on morphology and luminosity: morphological type $T < 1$ shown in red, $T \geq 1$ in blue, and transitional Irr/dE in green; luminosity $M_B < -19.5$ shown as large circles, $-19.5 < M_B < -17$ as small circles, and $M_B > -17$ as x's. UGC4879, located at (0.89, 0.97, -0.35), is circled and labeled. The large dashed circle represents the zero velocity surface of the Local Group, 940 kpc in radius, the dotted circles enclose a region 200 kpc in radius around the Milky Way and M31, and the dashed lines form a wedge at galactic latitude $|b| = 15°$.

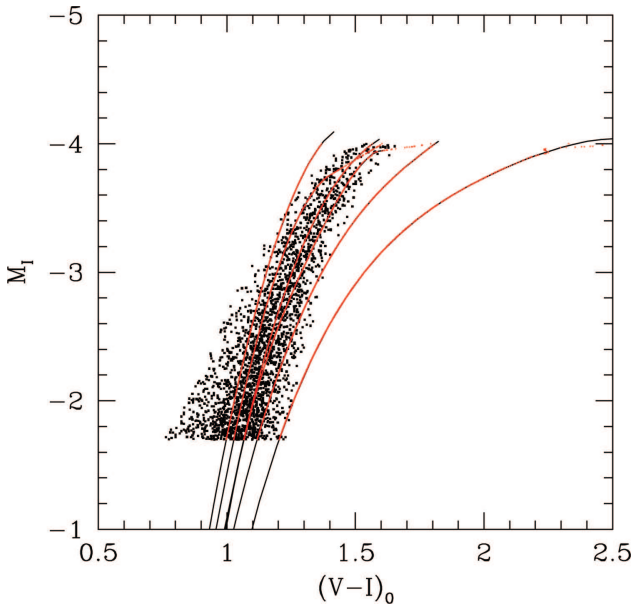

Figure 4.4 CMD of the RGB in UGC4879 in $(V-I)_0$ versus M_I selected to compare with the fiducial loci of the RGB of GGCs from Da Costa & Armandroff (1990) which are shown as curves. The metallicities of the GGCs used to produce these curves are: [Fe/H]= −2.17, −1.91, −1.58, −1.54, −1.29, and −0.71.

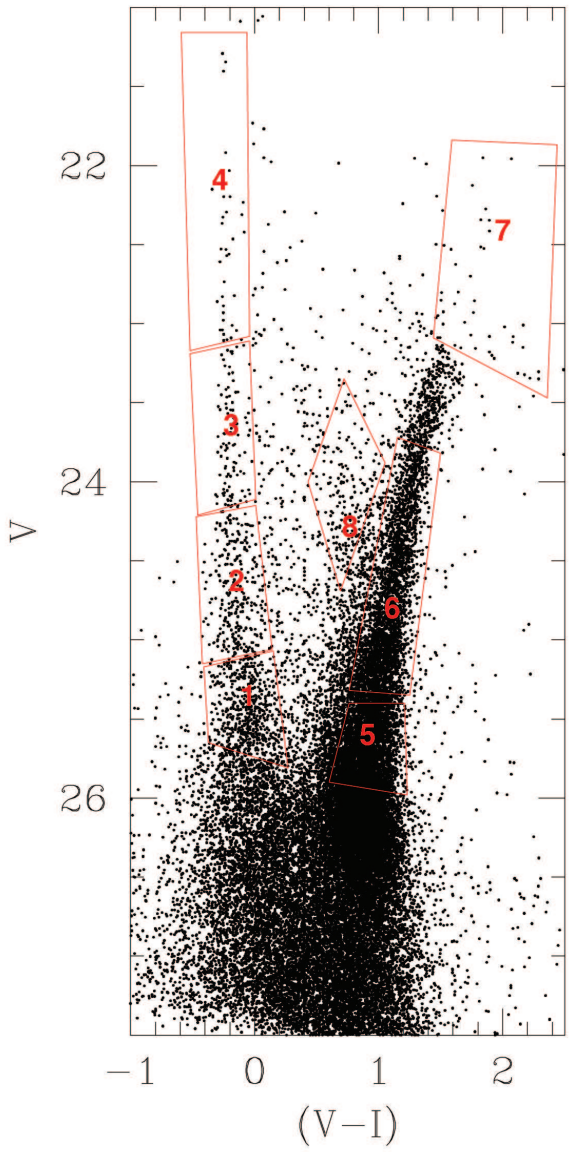

Figure 4.5 CMD of UGC4879 in $(V - I)$ versus V. The boxes enclose regions on the diagram that constrain the match between the observed and simulated CMDs.

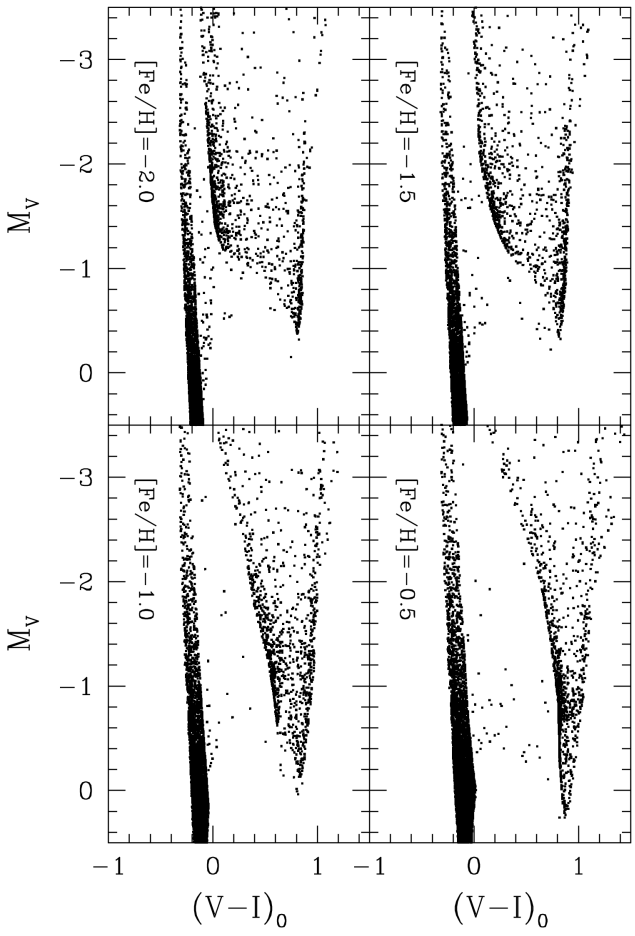

Figure 4.6 Simulated CMDs in $(V-I)_0$ versus M_V of stars with ages <500 Myr and fixed metallicity. The metallicities of the stars in the panels (reading left to right) are [Fe/H]= −2.0, −1.5, −1.0, and −0.5.

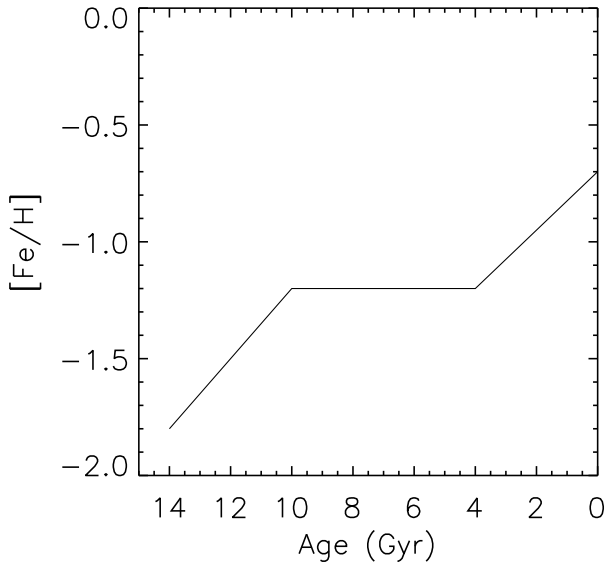

Figure 4.7 CEH of UGC4879 used as input for constructing its SFH.

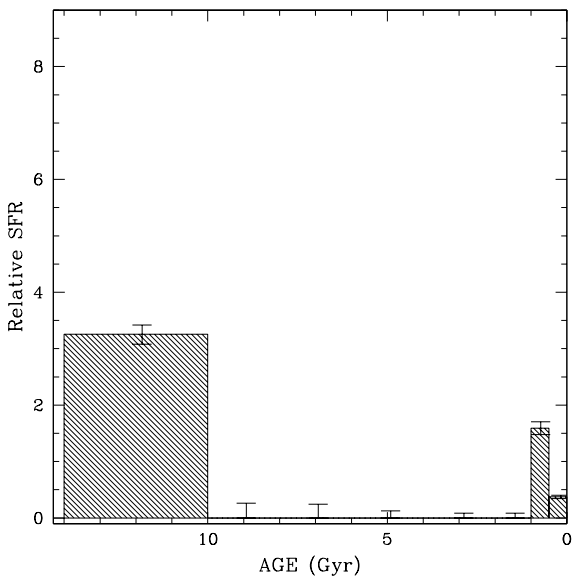

Figure 4.8 SFH of UGC4879. The relative star formation rate is normalized to 811 $M_{\odot}$ Myr^{-1}.

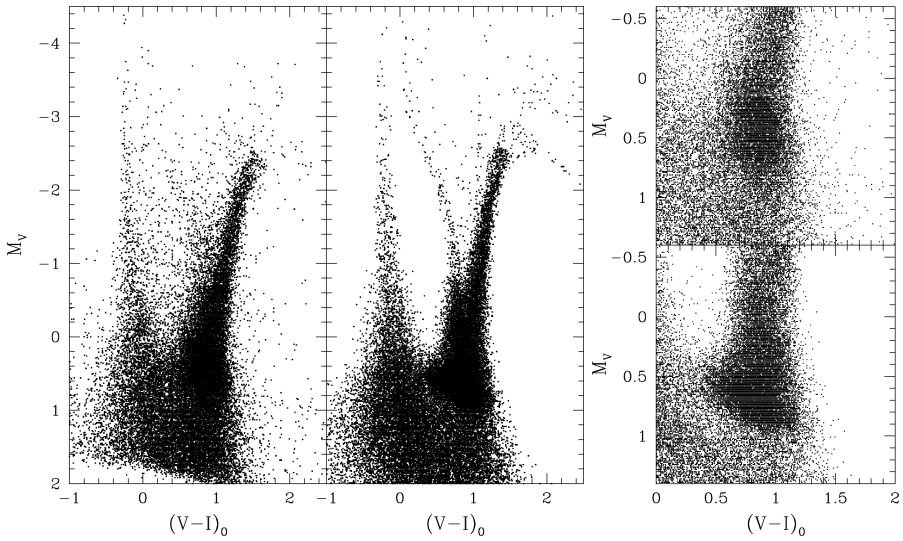

Figure 4.9 CMDs in $(V-I)_0$ vs M_V of UGC4879; the left panel consists of observed data, while the center panel consists of simulated data meant to reproduce the observed CMD based on the SFH shown in Figure 4.8. The right panel shows a magnified region of the CMD where the density of stars is highest. The observed data are shown above the simulated data in this zoomed panel.

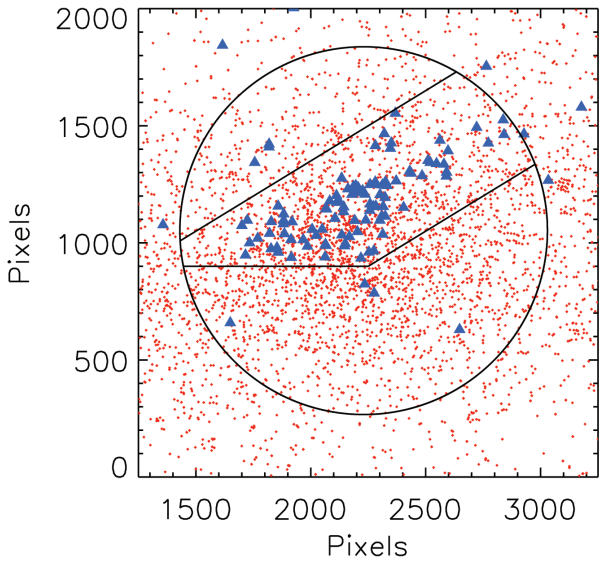

Figure 4.10 Distribution of stars on the image in Figure 4.1 with $I > 24$. Main sequence stars are plotted as blue triangles and RGB stars as red dots. The circle denotes the aperture limit applied to the data to reduce foreground contamination. The black lines denote the limits of the 'inner' and 'outer' regions of the galaxy for the purposes of comparing areas of active and inactive star formation.

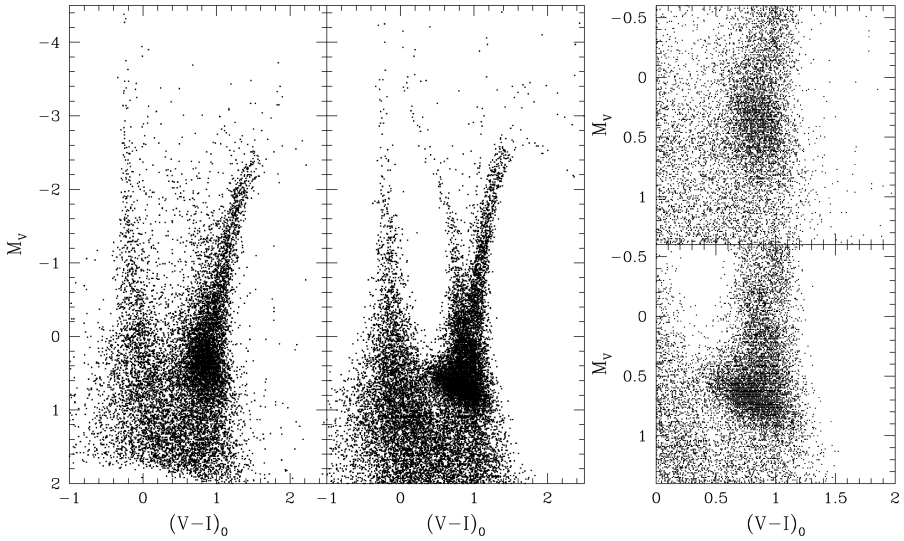

Figure 4.11 CMDs in $(V-I)_0$ vs M_V of the inner region of UGC4879 shown within the lines of Figure 4.10; the left panel consists of observed data, while the center panel consists of simulated data meant to reproduce the observed CMD based on the SFH shown in Figure 4.13. The right panel shows a magnified region of the CMD where the density of stars is highest. The observed data are shown above the simulated data in this zoomed panel.

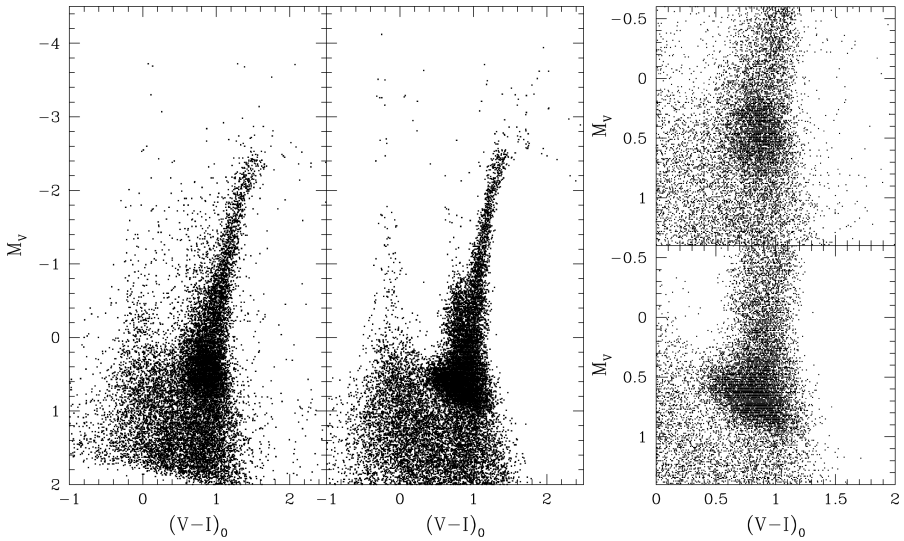

Figure 4.12 CMDs in $(V-I)_0$ vs M_V of the outer region of UGC4879 shown outside the lines of Figure 4.10; the left panel consists of observed data, while the center panel consists of simulated data meant to reproduce the observed CMD based on the SFH shown in Figure 4.14. The right panel shows a magnified region of the CMD where the density of stars is highest. The observed data are shown above the simulated data in this zoomed panel.

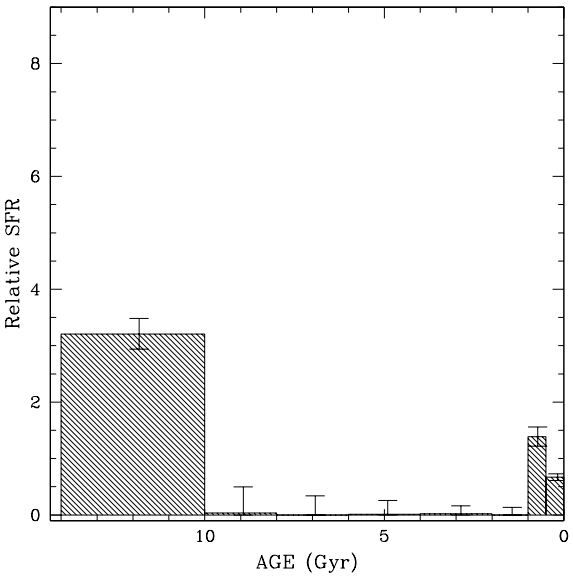

Figure 4.13 SFH of the inner region of UGC4879 shown within the lines of Figure 4.10. The relative star formation rate is normalized to 329 $M_\odot$ Myr^{-1}.

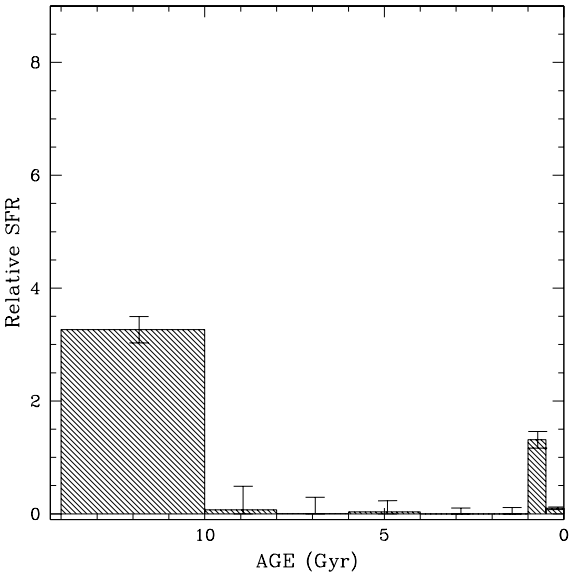

Figure 4.14 SFH of the outer region of UGC4879 shown outside the lines of Figure 4.10. The relative star formation rate is normalized to 440 $M_\odot$ Myr^{-1}.

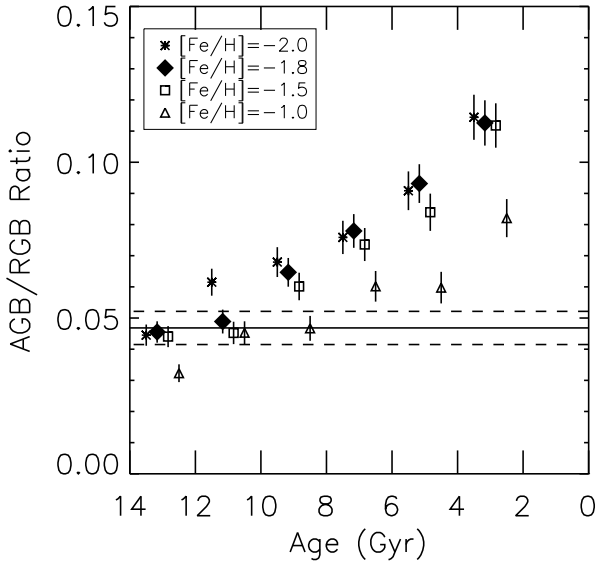

Figure 4.15 Ratio of the number of AGB to RGB stars (within the upper 2 magnitudes of the RGB) versus age in 2 Gyr bins (the horizontal offset of the symbols within bins is for clarity only). The asterisks, squares, and triangles represent fixed metallicities at [Fe/H]= -2.0, -1.5, and -1.0, respectively, while simulated stars with the measured RGB metallicity of [Fe/H]= -1.8 are shown as filled diamonds. The AGB/RGB ratio measured from observations of UGC4879 to be 0.047 ± 0.005 is plotted with horizontal lines (dashed lines indicate this uncertainty range). The ratio is omitted in the most recent age bin because other populations provide stronger constraints on the SFH as well as add complexity to the problem of defining an RGB or AGB star on the simulated CMDs.

Chapter 5

Rough Estimates of Stellar Histories of Dwarfs from HST Photometry of the Red and Asymptotic Giant Branches

5.1 Introduction

The several hundred color-magnitude diagrams (CMDs) that are available through the Extragalactic Distance Database (EDD) contain a wealth of information about the stellar content of the target galaxies. The various stellar populations that make up a CMD provide a picture of the current state of stellar evolution in a galaxy, and by matching these populations with simulations it is possible to develop a picture of the star formation history (SFH) of the galaxy. This CMD synthesis method has been applied to ∼100 galaxies, including most of the galaxies of the Local Group (e.g. Tolstoy et al. 2009, and references therein), as well as most galaxies beyond the Local Group and within ∼3 Mpc (e.g. Weisz et al. 2011; Williams et al. 2011). The deep data needed to synthesize a CMD to reproduce a galaxy's SFH limits the sample size to which these techniques can be applied. Many of the observations in our database were not geared towards measuring SFHs, so the depth of the data may be insufficient to merit CMD synthesis. In these cases a less detailed interpretation of each CMD can be used to distinguish between galaxies with young populations represented by, for example, bright main sequence and blue-loop stars, and those with only intermediate or old populations, such as those of the red and asymptotic giant branches (RGB, AGB).

We focus here on these older stars and how their ages are constrained by the ratio of number stars occupying the AGB and RGB. In addition to age, the metal content of these populations also influences their relative numbers at a given time. It is possible to estimate the metallicity of stars on the RGB from their colors, and thus the combination of color of the RGB and the AGB/RGB ratio have the potential to provide first order estimates of their age and metallicity. We present measurements for a sample of Local Volume galaxies observed with the Hubble Space Telescope (HST) and consider the results in the context of such factors as luminosity, morphology, and environment. In addition, we examine some systematic issues that arise in the application of these techniques. These issues will have increasing relevance as the census of Local Volume galaxies observed with HST pushes to greater distances and the variety of observable stellar populations in these newly observed galaxies becomes more limited.

5.2 Model Predictions

SFH studies that attempt to reconstruct a galaxy's observed CMD with simulated stars rely on model stellar evolutionary tracks combined with an initial mass function and usually build a chemical evolution history through iterative comparisons between the observed and simulated CMDs. Other issues, such as reddening and the relative numbers of binaries and multiple star systems must be considered in the matching effort. Once these issues are settled the match between the CMDs is evaluated quantitatively by comparing the number of stars in a given region of magnitude and color space. These regions can be chosen by hand to highlight the different stellar populations observed, as in our previous work on UGC4879 (Jacobs et al. 2011), or by applying a grid across the CMD in the form of a Hess diagram (e.g. Weisz et al. 2011). It is possible then, to step back in this matching process and ask about the relative numbers of stars that are predicted by the models for a range of ages and metallicities.

We count the relative numbers of AGB and RGB stars based on stellar evolutionary models from Bertelli et al. (1994) and Girardi et al. (2000), along with a Salpeter (1955) initial mass function. As can be seen in Figure 5.1 these models predict that for a population of stars of a given metallicity the AGB/RGB ratio will fall monotonically as the stars age. This evolution in the ratio is also visible in the sequence of simulated CMDs in Johnson-Cousins $(V-I)_0$ vs M_I for stars at [Fe/H]$= -2.0$ in Figure 5.2. The low luminosity limit of the AGB is taken to be the magnitude of the tip of the red

giant branch (TRGB), where for the artificial stars we use the zero-point calibration of the absolute magnitude of the TRGB as defined by Rizzi et al. (2007):

$$M_I^{TRGB} = -4.05 + 0.217[(V - I) - 1.6] \tag{5.1}$$

This calibration is displayed as a line across the CMDs in Figure 5.2. The RGB stars are included in the count if they are within two magnitudes to the faint side of the TRGB. At fainter magnitudes the simulated stars appear as two branches. The blue branch actually consists of early stage AGB stars, while the RGB proper is located to the red of these stars. In practice it is usually impossible to distinguish between these two populations in actual observations and the AGB are much less numerous ∼15% (Gallart et al. 2005) so they are collectively referred to as the RGB. The AGB stars are characterized by He burning in an inner shell and H burning in an outer shell. He burning dominates in early AGB stars, but when the H shell is re-ignited the shells alternate as the main source of energy and the stars pulsate thermally (Gallart et al. 2005). The AGB stars brighter than the TRGB are in this thermally pulsing phase. Therefore the AGB to RGB ratio is technically shorthand for the thermally pulsing AGB to early AGB plus RGB ratio.

5.2.1 Metallicity

For a given metallicity, a younger population of stars is expected to have more AGB stars than an older one, though metallicity does play a role. The models suggest that two equal age populations will have different ratios if their metallicities differ. Generally, lower metallicity equates to a higher AGB/RGB ratio among stars of the same age. Similarly, the sensitivity of the ratio to age appears to decrease with increasing metallicity. The models shown in Figure 5.1 are all taken at low metallicity, and this is because the trends seen here become less apparent at higher abundances.

The metal content of stars influences the numbers that are observed in the bright thermally pulsing AGB phase relative to those on the RGB. It is therefore desirable to measure these abundances. There are ongoing efforts to obtain spectra of individual red giants located in galaxies in and around the Local Group (e.g. Kirby et al. 2011, 2012; Lemasle et al. 2012), but the relatively large investment of observational resources required makes this technique infeasible for use in galaxies outside the periphery of the Local Group. We must then consider metallicity estimates based on photometry. A medium-band filter centered on the Ca H and K lines included with Wide-

Field Camera 3 (WFC3) with HST, $F390M$, holds promise for use in generating fairly accurate metallicity estimates. However, observations with such a filter that is sensitive to light that is well away from the peak of the spectral energy distribution of an RGB star requires a significant time commitment for even the nearest galaxies. So the question becomes: what information does the broadband photometry hold in terms of metallicity? The colors of stars on the RGB are sensitive to both metallicity and age, so this degeneracy can limit the accuracy of color-based measurements. Nevertheless, a star's position on the RGB is more sensitive to metallicity than age. An age difference of several Gyr is needed for two stars to occupy the same space on the RGB when they have a metallicity difference of order 0.1 dex (Held et al. 2010).

A common method for converting from color to metallicity is by comparison with the color of the RGB observed in galactic globular clusters of known metallicity. Here, we are comparing ancient stars in globular clusters with extragalactic populations that may include significantly younger stars. Additionally, the differences between the color of the RGB among the template clusters are fairly small, so any error in the color measurement of the stars in a target galaxy will result in a magnified error in metallicity with this method. A measurement of absolute metallicity based on broadband colors should be used with caution. However, the metallicities are useful in comparison with other galaxies in the sample, as described further below.

5.3 Measurements

The observations that make up the sample are housed in the CMDs/TRGB section of the Extragalactic Distance Database (Tully et al. 2009). Each CMD is constructed using images from the Advanced Camera for Surveys (ACS) or Wide-Field Planetary Camera 2 (WFPC2) on HST taken in $F814W$ and either $F555W$ or $F606W$. Photometry is measured using the Dolphot and HSTphot software packages (Dolphin 2000), and each galaxy's distance is measured through identification of the TRGB. The full procedures are described in Jacobs et al. (2009).

5.3.1 AGB and RGB counts

In order to isolate the AGB and RGB from other populations observed in a galaxy's CMD we define the regions containing them through visual inspection. The blue and red edges of the RGB, along with an upper envelope of the AGB are defined by clicking a series of points on the diagram, which

are then used to generate spline fits to divide up the CMD. The AGB is divided from the RGB at the magnitude of the TRGB. Figure 5.3 shows the CMD of UGC8651 and the stars defined to be on the RGB are colored red, while those expected to on the AGB are colored blue. There are 249 points designated as AGB stars, and 4750 points (with $F814W < (TRGB + 2) = 25.37$) designated as RGB stars, for a ratio of 0.052 ± 0.003, where the uncertainty is taken to be Poisson noise.

5.3.2 Photometric Metallicities

As described above, a rough estimate of the metal content of the RGB stars observed in nearby galaxies can be obtained by comparing their colors with those of RGB stars in galactic globular clusters. For this we take the RGB stars as identified by the procedures given in the previous subsection and measure the color difference between each star and each cluster's fiducial locus of color of the RGB. These define a mean color difference between the target galaxy and each of the calibrating clusters, and a quadratic fit to the these mean differences produces an estimate of the galaxy's metallicity. Figure 5.4 shows the RGB of UGC8651 in $(V-I)_0$ vs M_I plot with the fiducial color loci of clusters with spectroscopic metallicities observed by Da Costa & Armandroff (1990). The quadratic fit to the mean color difference between the RGB stars and the loci ($< \delta VI >$) is:

$$[\mathrm{Fe/H}] = -5.86 < \delta VI >^2 -6.99 < \delta VI > -2.38 \tag{5.2}$$

the metallicity of UGC8651 is taken to be [Fe/H]=-2.38. The RMS uncertainty of this fit is 0.04, but this is not expected to be representative of the overall uncertainty due to systematic issues related to comparing broadband colors of the RGB between galaxies and the ancient stars in globular clusters. Furthermore, these fits require a distance estimate (which we take from the TRGB), an estimate of reddening, and a conversion from HST flight filters to Johnson-Cousins magnitudes. The reddening estimates are the same as those used in estimating the TRGB distance, and usually are taken from Schlegel et al. (1998) dust maps. Uncertainties in reddening within the target galaxies may represent a significant source of error, but this may be mitigated somewhat by focusing on lower luminosity systems where internal extinction will be less extreme than in massive systems. The luminosity cuts that we impose are discussed in more detail below. Finally, the observations of the globular clusters are in Johnson-Cousins V and I, so we use the internal conversions to these filters that are included in the Dolphot/HSTphot output and are based on Sirianni et al. (2005).

5.3.3 Luminosity and Morphology

For the majority of the sample we estimate their luminosities based on their K_s-band fluxes as measured in the 2 Micron All-Sky Survey (2MASS: Skrutskie et al. 2006). We choose this filter over more traditional ones, such as B to minimize sensitivity to recent star formation, as well as sensitivity to reddening. These fluxes are calculated based on magnitudes published in the 2MASS Extended Source Catalog. For very extended low surface brightness galaxies where 2MASS fluxes are unavailable, K_s-band luminosities are calculated using I-band or (if necessary) B-band observations from Karachentsev et al. (2004) and transformed using the relations in Tully et al. (1998). We convert the K_s-band magnitudes to luminosities using our TRGB distances.

The morphological types of the galaxies in the sample are collected from Karachentsev et al. (2004), where they are assigned to a numerical Hubble stage. The most common type in the sample is +10, corresponding to a dwarf irregular galaxy. These morphological types, along with distances, AGB/RGB ratios, and photometric metallicities are listed in Table 5.1. Figure 5.5 shows the K_s-band luminosity and photometric metallicity of the galaxies listed.

5.4 Analysis

5.4.1 Luminosity Cut

The challenges in measuring the AGB/RGB ratio, and a RGB-color based metallicity become increasingly difficult as the luminosity of the target galaxy increases. Complex star formation histories at various metallicities makes distinguishing between AGB and RGB stars not necessarily straight-forward. Similarly, the metallicity estimates use ancient low-metallicity stars of globular clusters as their metric, and these need not resemble the stars found in giant galaxies where the SFH has been and usually remains much more active. Therefore, the more luminous members of the Local Volume are excluded from the analysis.

A related issue involves the galaxies' extent on the sky. Most nearby dwarf galaxies main stellar components fit well within the field of view of ACS or WFPC2, while the giant galaxies do not. Due to the the risk of double-counting stars in overlapping images and the often heterogeneous nature of HST observations of different fields of the same galaxy, all our CMDs are produced from a single pointing per galaxy. In examining the sample, we found that nearly all galaxies with K_s luminosities

less than 10^8 $L_\odot$ fit within the HST cameras view, and had easily differentiable RGBs and AGBs, while those above this luminosity start to have more complicated CMDs and/or extend beyond the cameras' field-of-view. There are 87 galaxies in EDD with HST observations deep enough to measure an AGB/RGB ratio with K_s-band luminosities less than 10^8 $L_\odot$, and their properties are listed in Table 5.1.

Since angular size depends on distance some Local Group galaxies, not otherwise excluded by luminosity, extend off the images from HST. Ten of the 87 galaxies in the sample are located at distances less than 1.1 Mpc. The most luminous example is WLM/DDO221, and has an angular diameter of 11.5 arcminutes (Karachentsev et al. 2004), corresponding to between 3 and 4 ACS/WFPC2 fields-of-view. Thus, there is some risk of biased results from sampling only a portion of the stars in this galaxy and other Local Group galaxies. However, for our current purposes this is a minor concern, since AGB stars tend to exist in the same regions as RGB stars in a galaxy and other uncertainties in the measurements are likely to overwhelm those due to under sampling. Therefore, we leave the Local Group dwarfs in the sample.

5.4.2 AGB/RGB Ratio versus RGB Color

We compare the observed AGB/RGB ratios of the target galaxies with their putative mean metallicities computed from the color of the RGB in Figure 5.6. Galaxies with morphological type $T \geq 0$ are plotted as blue triangles and those with $T < 0$ as red circles. This amounts to a division between dwarf irregulars and dwarf ellipticals/spheroidals. The dSph/dE tend to have higher metallicities and lower AGB/RGB ratios than the dIrr, though there is a continuum and substantial scatter.

5.4.3 Errors in AGB/RGB Ratio

Errors in the measurement of the AGB/RGB ratio stem from several factors, most of which have to do with misidentified stars. In nearly all cases the RGB is the dominant feature of the CMD, so it is rarely difficult to identify it and count the stars that are within 2 magnitudes below the TRGB. Some galaxies have significant populations to the blue of their RGB such as blue loop and main sequence stars that can obscure the edge of the RGB. However, this is mostly a problem in fairly luminous galaxies, and the fewer stars that make up the dwarfs that are considered here tend to have

clearly discernible blue edges (any stars found to the red of the RGB can generally be considered contaminants). The galaxies in the sample have more than ten stars on the upper RGB for every AGB star, so any interlopers counted as part of the AGB will have a greater affect on the results than they would if counted as RGB stars. A source of extraneous counts to the AGB from within the target galaxy are red super giants (a.k.a. red helium burners) that appear as a vertical sequence above the RGB, and slightly to the blue of the AGB and RGB. Luckily, the red super giants occupy a narrow color range, so can be distinguished from the AGB. More of a concern are contaminants from outside the target galaxy, generally Milky Way stars. The AGB plume on the CMD occupies a fairly large area of color/magnitude space at relatively low density, and particularly in observations at low galactic latitude, objects outside the target galaxy may appear on the CMD at comparable densities. In cases where many foreground stars are visible we attempt to mitigate their influence by identifying the edge of the target galaxy on the HST image based on the pixel location of the stars that make up the CMD, and exclude those that are located off this edge, effectively clipping the image. Another issue comes from RGB stars identified as AGB stars and vice versa. We split the AGB and RGB at the magnitude of the TRGB. There is some inherent uncertainty in the TRGB measurement that will result in a given star falling in one region or the other on the CMD. Most of this issue is due photometric error, which will scatter not only the AGB and RGB but any star into and out of the regions defining the AGB, and RGB. Again, while a component of this effect is random and covered by shot noise, the greater numbers of RGB stars available for scattering into the AGB compared to AGB stars to scatter out will tend to inflate the AGB count. These issues make it somewhat risky to make quantitative predictions based on the AGB/RGB ratio, but it should still be safe to analyze the measurements qualitatively.

5.5 Discussion

In general, the dIrr galaxies tend to have higher AGB/RGB ratios than the dSph/dEll galaxies. This is a predictable result since dIrrs tend to show signs of recent and/or ongoing star formation (e.g. Mateo 1998; Tolstoy et al. 2009; Weisz et al. 2011). Most dIrr in the sample have observable main sequences (e.g. UGC8651, Figure 5.3), indicating that star formation has occurred within the last Gyr or so. A galaxy with young stars and a well-populated AGB would likely have had star formation during the recent few Gyr as well. In contrast, UGC8651 has an AGB/RGB ratio of

0.052 ± 0.004, which is towards the low end of what is observed among dIrrs. This situation is similar to what is observed in UGC4879 (Jacobs et al. 2011), where we concluded that the combination of the presence of young stars and relatively low AGB/RGB ratio indicated a recent uptick in star formation, following a long period where we see no evidence of star formation. In that paper, we speculated that the recent star formation might be caused by infalling gas, either primordial or re-accreted following an earlier episode of star formation. With the identification a more galaxies that share the characteristics of the CMD of UGC4879 it may be possible to test this hypothetical triggering from external gas.

Unlike the dIrr galaxies the early-type dwarfs tend not to show evidence for young stars. Complementary evidence from their low AGB/RGB ratios suggests that this lack of star formation extends back to intermediate times. However, some of the outlying cases merit further examination. F8D1 and ESO269-37 have AGB/RGB ratios higher than other dSphs, at 0.068 ± 0.004 and 0.067 ± 0.006, respectively. As seen in Figure 5.7 the CMD of F8D1 is fairly unremarkable and contains no young populations. The elevated ratio implies that star formation in F8D1 turned off more recently than what seems to be typical of other dSph. Presumably, as the AGB stars age its ratio will fall and it will more closely resemble other dSph galaxies. The CMD of ESO269-37 could yield a similar interpretation. Unfortunately, it suffers from foreground contamination (Figure 5.8) as the galaxy is located near the plane of the Milky Way. However, like F8D1, it does not appear that this galaxy contains young stars. Since the foreground stars skew the AGB/RGB ratio, we consider a CMD that is constructed from a clipped image containing only the main part of the galaxy. There are undoubtedly still interlopers so the ratio of 0.067 may be considered an upper limit. Thus, ESO269-37 could be a normal dSph, but there are hints that it contains stars that are younger than what is seen in most dSph/dE.

The discussion so far has focused on a qualitative interpretation of the AGB/RGB ratio observed among the nearby dwarfs. In order to be more quantitative in our analysis we need to consider the stellar metallicities. As described above, there are a number uncertainties in estimating metallicity from the color of the RGB that reduce accuracy. Hence, it would be problematic to read off an age estimate by matching the observed ratio to the ratio using simulated stars with the same metallicity. This remains the goal of this work, but it is necessary to validate these measurements by comparing them with age estimates that result from more detailed studies of the galaxies' SFHs. We made such a comparison using the SFH estimates from 60 nearby dwarf galaxies that were calculated by Weisz

et al. (2011). They calculate absolute as well as cumulative star formation rates. In order to apply the analysis across a range of luminosities we use the proportional rates in their cumulative star formation results in our comparison. We failed to find a clear correlation between their relative age estimates and our measurements of AGB/RGB ratio (even after dividing the sample into different subsets of similar metallicity). The difficulty in determining the metal content of the observed stars is likely to be a significant factor in obscuring the expected correlation. However, the Weisz et al. star formation rates are also quite uncertain, as seen in the large error envelopes around the cumulative star formation rate plots in their Figure 3. Thus, the lack of a correlation between the AGB/RGB ratio and their results does not necessarily indicate that the ratio's use as a probe of stellar ages cannot be quantitative. It may be as simple as calibrating the results based on comparison with galaxies with more precisely determined SFHs, i.e. those in the Local Group. Though this effort may also require a refinement of the metallicity estimates and star counts. Ideally this refinement in metallicity would still use the RGB color, because nearly all other methods are much more observationally expensive.

Despite the factors that reduce the reliability of the metallicity estimates, there does appear to be a trend versus the AGB/RGB ratio. There is substantial scatter, but generally speaking, the AGB/RGB ratio is higher in lower metallicity galaxies and vice versa. The early-type dwarfs are generally clustered at the higher metallicity/lower ratio end of the sequence, and there are some overlapping late-type dwarfs, but on the whole they tend to have lower metallicity/higher ratios. Nearly all galaxies that have had their SFHs studied show evidence for ancient stars (e.g. Tolstoy et al. 2009; Weisz et al. 2011). Therefore, this sequence would suggest a scenario where star formation in early type dwarfs was shorter lived than in late-types but the enrichment of their interstellar media was more efficient. F8D1, with it's high AGB/RGB ratio compared to other dSph, also has a redder RGB resulting in a metallicity estimate of [Fe/H]=-1.07. Under this scenario the more efficient enrichment may have lasted for longer periods than in other dSphs, accounting for both its higher ratio and metallicity. The other dSph with a metallicity comparable to F8D1 is KK197, with [Fe/H]=-1.09, see Figure 5.9. The source of this high value is a plume of stars extending to the red of the main part of the RGB, near its tip. This type of plume is seen in CMDs of massive galaxies, but not typically in dwarfs. KK197 is a satellite of Cen A, and halo observations of that galaxy do exhibit this plume feature, thus a likely explanation for the CMD of KK197 is that it contains some Cen A red giants. Finally, the galaxy with the highest metallicity in the sample is UGC5336,

with [Fe/H]=-0.82, it also has among the lowest ratios of late-type dwarfs at 0.029 ± 0.003. These attributes are suspect because UGC5336 is a tidal dwarf near NGC3077 in the M81 group and the RGB stars seen may not be associated with it. Meanwhile, the young stars likely formed from previously enriched gas stripped from one of these giants (Croxall et al. 2009), and as seen in its CMD in Figure 5.10 it appears to be dominated by young stars.

The general sequence seen in AGB/RGB ratio versus photometric metallicity, and segregation with morphology, along with the utility in identifying outlying cases holds promise for interpreting the ages and abundances of older stars in nearby dwarfs. Reliable estimates of ages will most likely require refinements in the measurement techniques, but should become possible with currently available data as well as with ongoing HST observations. Analyses of the stellar histories of galaxies that extend deeper than $\sim$1 Gyr into the past will have to depend on these techniques, since only a chosen few galaxies will be subject to more extensive observation campaigns. Thus, it behooves us to refine these techniques as much as possible.

References

Bertelli, G., Bressan, A., Chiosi, C., Fagotto, F., Nasi, E. 1994, AAPS, 106, 275

Croxall, K. V., van Zee, L., Lee, H., et al. 2009, ApJ, 705, 723

Da Costa, G. S., Armandroff, T. E. 1990, AJ, 100, 162

Dolphin, A. E. 2000, PASP, 112, 1383

Gallart, C., Zoccali, M., Aparicio, A. 2005, ARAA 43, 387

Girardi, L., Bressan, A., Bertelli, G., Chiosi, C. 2000, AAPS, 141, 371

Held, E. V., Gullieuszik, M., Rizzi, L., Girardi, L., Marigo, P., Saviane, I. 2010, MNRAS, 404, 1475

Jacobs, B. A., Rizzi, L., Tully, R. B., Shaya, E. J., Makarov, D. I., Makarova, L. 2009, AJ, 138, 332

Jacobs, B. A., Tully, R. B., Rizzi, L., Karachentsev, I. D., Chiboucas, K., Held, E. V. 2011, AJ, 141, 106

Karachentsev, I. D., Karachentseva, V. E., Huchtmeier, W. K., Makarov, D. I. 2004, AJ, 127, 2031

Kirby, E. N., Lanfranchi, G. A., Simon, J. D., Cohen, J. G., Guhathakurta, P. 2011, ApJ, 727, 78

Kirby, E. N., Cohen, J. G., Bellazzini, M. 2012, ApJ, 751, 46

Lemasle, B., Hill, V., Tolstoy, E., et al. 2012, A&A, 538, A100

Makarov, D., Makarova, L., Rizzi, L., Tully, R. B., Dolphin, A. E., Sakai, S., Shaya, E. J. 2006, AJ, 132, 2729

Mateo, M. L. 1998. ARA&A, 36, 435

Rizzi, L., Tully, R. B., Makarov, D., Makarova, L., Dolphin, A. E., Sakai, S., Shaya, E. J. 2007, ApJ, 661, 815

Salpeter, E. E. 1955, ApJ, 121, 161

Schlegel, D. J., Finkbeiner, D. P., Davis, M. 1998, ApJ, 500, 525

Sirianni, M., Jee, M. J., Benítez, N., et al. 2005, PASP, 117, 1049

Skrutskie, M. F., et al. 2006, AJ, 131, 1163

Tolstoy, E., Hill, V., Tosi, M. 2009, ARA&A, 47, 371

Tully, R. B., Pierce, M. J., Huang, J.-S., Saunders, W., Verheijen, M. A. W., Witchalls, P. L. 1998, AJ, 115, 2264

Tully, R. B., Rizzi, I., Shaya, E. J., Courtois, H. M., Makarov, D., Jacobs, B. A. 2009 AJ, 138, 323

Weisz, D. R. et al. 2011, ApJ, 739, 5

Williams, B. F. et al. 2011, ApJ, 734, L22

Table 5.1. Properties of Dwarf Galaxies

PGC	Name	HST #	Dist. (Mpc)	AGB/RGB	$\sigma_{A/R}$	[Fe/H]	Lum.$_{Ks}$ (10^6 $L_\odot$)	Type
143	DDO221	6813	0.98	0.051	0.009	-2.00	26.7	9
621	ESO349-031	9771	3.21	0.045	0.005	-2.10	5.63	10
1038	ESO410-005	10503	1.92	0.046	0.005	-2.30	3.18	-1
1641	ESO294-010	10503	2.03	0.039	0.004	-1.87	2.11	-3
2881	ESO540-030	10503	3.55	0.041	0.004	-2.02	0.812	-1
2933	ESO540-032	10503	3.61	0.024	0.003	-1.97	1.84	-3
3792	LGS3	6695	0.65	0.030	0.022	-1.79	0.0076	-1
6830	Phoenix	8706	0.43	0.021	0.011	-1.78	0.165	-1
21199	ESO059-01	9771	4.49	0.047	0.001	-1.8	46.0	9
21302	DDO44	8137	3.17	0.037	0.003	-1.66	2.06	-3
23521	M81DwA	10605	3.40	0.030	0.005	-2.16	0.936	10
24050	UGC4459	10605	3.66	0.053	0.003	-2.03	12.1	10
24213	UGC4483	8769	3.56	0.082	0.007	-2.25	5.09	10
26142	UGC4879	10584	1.36	0.032	0.004	-1.77	3.55	10
27605	UGC5139	10605	3.98	0.051	0.002	-2.14	55.9	10
28731	KDG61	9884	3.61	0.034	0.002	-1.71	7.02	-1
28757	UGC5336	10605	3.80	0.029	0.003	-0.82	18.0	10
28868	DDO69	8575	0.74	0.053	0.024	-1.96	0.787	10
28913	DDO70	8601	1.43	0.058	0.004	-2.43	27.0	10
29128	NGC3109	8601	1.33	0.065	0.003	-2.21	35.8	9
29194	Antlia	10210	1.35	0.054	0.010	-2.50	0.0875	10
29231	BK5N	5898	3.65	0.038	0.006	-1.62	0.250	-3
29257	DDO71	9884	3.56	0.037	0.002	-1.60	2.20	-3

Table 5.1—Continued

PGC	Name	HST #	Dist. (Mpc)	AGB/RGB	$\sigma_{A/R}$	[Fe/H]	Lum.$_{Ks}$ (10^6 $L_\odot$)	Type
29388	KDG64	9884	3.71	0.036	0.002	-1.66	4.68	-3
29653	DDO75	7496	1.43	0.075	0.007	-3.19	26.1	10
30997	DDO82	10915	3.90	0.040	0.001	-1.61	67.6	9
35286	UGC6456	6276	4.60	0.061	0.003	-1.97	29.6	10
35878	NGC3741	8601	3.21	0.043	0.003	-1.93	2.48	10
37050	DDO99	8601	2.64	0.054	0.003	-2.23	14.8	10
38881	NGC4163	9771	2.98	0.046	0.002	-2.17	30.5	10
39023	NGC4190	10905	2.82	0.075	0.003	-2.59	33.5	10
39058	UGC7242	9771	5.42	0.068	0.002	-1.86	17.7	10
39145	DDO113	8601	2.96	0.040	0.004	-1.82	1.20	10
39228	CGCG269-049	11986	4.59	0.035	0.004	-2.87	3.01	10
40665	UGCA281	10905	5.68	0.061	0.003	-2.62	19.0	10
40904	DDO125	8601	2.59	0.046	0.002	-1.89	35.7	10
41020	UGC7599	10905	4.70	0.074	0.004	-2.28	42.1	9
42275	UGCA292	10915	3.84	0.068	0.009	-2.55	0.858	10
42936	ESO381-018	9771	5.37	0.061	0.003	-2.18	14.1	10
43048	ESO381-20	10235	5.40	0.073	0.002	-2.62	56.7	10
43869	NGC4789A	10905	4.04	0.050	0.003	-2.48	30.2	10
43978	ESO443-09	10235	5.89	0.036	0.005	-2.49	1.87	10
44491	DDO155	5915	2.18	0.047	0.006	-1.98	0.621	10
45104	ESO269-37	11986	3.08	0.067	0.006	-1.70	1.34	-3
45506	UGC8215	9771	4.57	0.064	0.005	-1.83	4.30	10
45916	ESO269-66	10235	3.66	0.038	0.001	-1.48	36.8	-1

Table 5.1—Continued

PGC	Name	HST #	Dist. (Mpc)	AGB/RGB	$\sigma_{A/R}$	[Fe/H]	Lum.$_{Ks}$ (10^6 $L_\odot$)	Type
46127	UGC8331	10905	4.41	0.036	0.002	-2.20	27.9	10
46663	KK196	9771	3.89	0.049	0.004	-2.07	5.38	10
46680	KK197	9771	3.74	0.023	0.001	-1.09	3.74	-3
47073	IC4247	10235	5.11	0.089	0.003	-2.42	36.7	10
47495	UGC8508	8601	2.65	0.058	0.004	-2.09	7.14	10
48029	ESO444-78	10235	5.37	0.049	0.002	-2.14	24.8	10
48280	UGC8638	9771	4.29	0.044	0.002	-1.96	3.36	10
48332	UGC8651	10210	3.10	0.052	0.003	-2.38	7.06	10
48738	ESO325-11	11986	3.34	0.078	0.003	-2.40	33.1	10
49158	UGC8760	10210	3.30	0.052	0.003	-2.31	16.5	10
49452	UGC8833	10210	3.25	0.070	0.006	-2.44	2.03	10
49615	ESO384-016	10235	4.43	0.054	0.002	-1.97	19.6	10
50961	UGC9128	10210	2.29	0.083	0.007	-2.74	4.92	10
51472	DDO190	10915	2.83	0.043	0.002	-3.14	36.4	10
63287	ESO594-004	9820	1.05	0.092	0.013	-2.36	0.927	10
65367	DDO210	8601	0.97	0.039	0.012	-2.06	0.923	10
69519	Tucana	5423	0.92	0.024	0.008	-1.83	0.0391	-2
71431	UGCA438	8192	2.21	0.052	0.004	-1.70	6.75	10
71538	Pegasus	5915	0.95	0.049	0.006	-1.37	0.914	10
95597	KKH37	9771	3.39	0.041	0.004	-1.91	0.600	10
166065	KK17	10210	4.97	0.025	0.004	-1.83	0.840	10
166073	KK27	10210	4.13	0.041	0.005	-1.77	1.65	-3
166101	KK77	9884	3.72	0.035	0.002	-1.56	2.37	-3

Table 5.1—Continued

PGC	Name	HST #	Dist. (Mpc)	AGB/RGB	$\sigma_{A/R}$	[Fe/H]	Lum.$_{Ks}$ (10^6 L$_\odot$)	Type
166142	LEDA166142	10905	4.31	0.055	0.007	-2.33	0.970	10
166158	KK189	9771	4.15	0.028	0.004	-1.79	0.250	-3
166185	KK230	9771	2.19	0.069	0.017	-2.95	0.0171	10
2801026	KKR25	8601	1.91	0.035	0.010	-1.96	0.120	10
2807103	KKH6	9771	3.38	0.044	0.003	-2.11	3.31	10
2807150	KKH86	8601	2.59	0.057	0.009	-2.04	0.190	10
2807155	CasdSph	8192	0.79	0.022	0.005	-1.53	1.19	-3
2807157	KKH98	8601	2.52	0.058	0.007	-1.68	0.352	10
2815822	KKs55	10235	3.75	0.023	0.002	-1.87	0.120	-3
2815823	KKs57	9771	3.77	0.025	0.006	-1.81	0.150	-3
3097113	HIPASSJ1351-47	10235	5.57	0.075	0.006	-2.44	11.3	10
3097691	Cetus	8601	0.73	0.023	0.010	-2.26	0.157	-2
3097727	ScdE1	10503	4.27	0.036	0.004	-2.01	0.240	-3
3097827	F8D1	5898	3.66	0.068	0.004	-1.07	10.7	-3
3097828	FM1	9884	3.71	0.030	0.003	-1.80	0.300	-3
4614882	HIPASSJ1348-37	10235	5.57	0.059	0.006	-2.47	1.00	0
4689187	CenN	9771	3.57	0.033	0.004	-1.77	0.400	-3
4689195	IKN	9771	3.72	0.027	0.002	-1.54	5.62	-3
4689216	HS117	9771	3.87	0.033	0.004	-1.99	3.89	-3

Note. — Nearby dwarf galaxies observed with HST, the columns contain: PGC number, common name, HST program number, TRGB distance in Mpc, AGB/RGB ratio, uncertainty in the ratio, metallicity from the color of the RGB, K_s-band luminosity in 10^6L$_\odot$, and morphological type from Karachentsev et al. (2004).

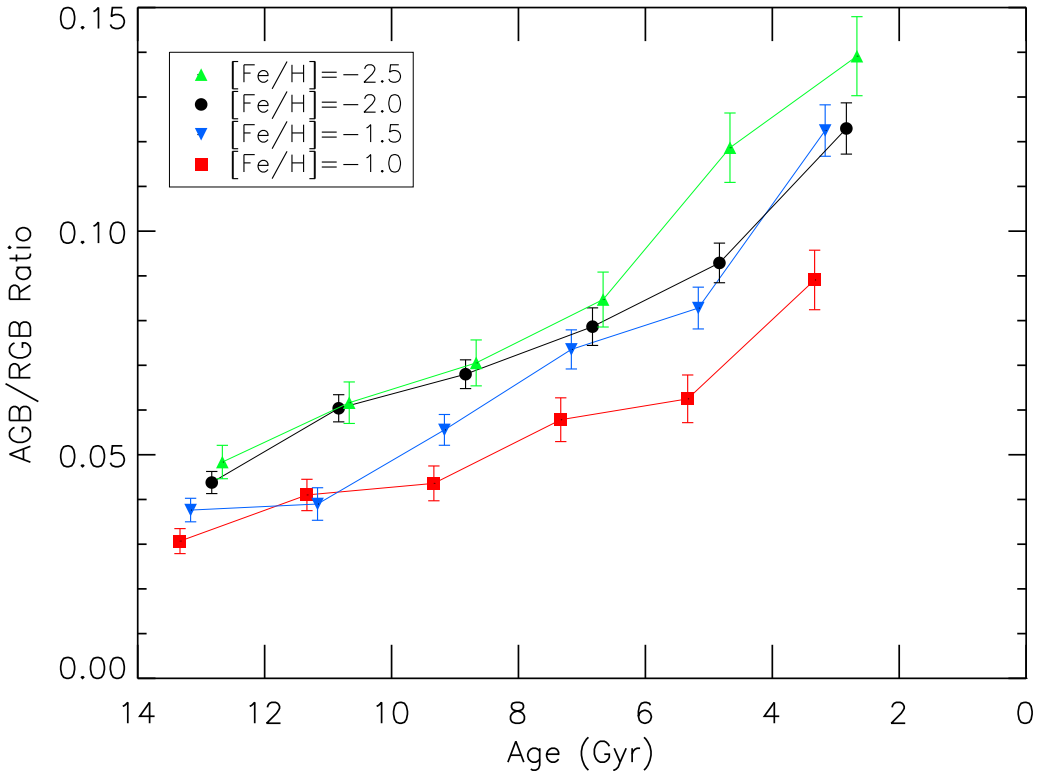

Figure 5.1 Ratio of the number of simulated AGB to RGB stars versus age in 2 Gyr bins (the horizontal offset of the symbols within bins is for clarity only). The green triangles, black circles, blue inverted triangles, and red squares, and triangles represent fixed metallicities at [Fe/H]= −2.5, −2.0, −1.5, and −1.0, respectively, with error bars calculated from Poisson statistics.

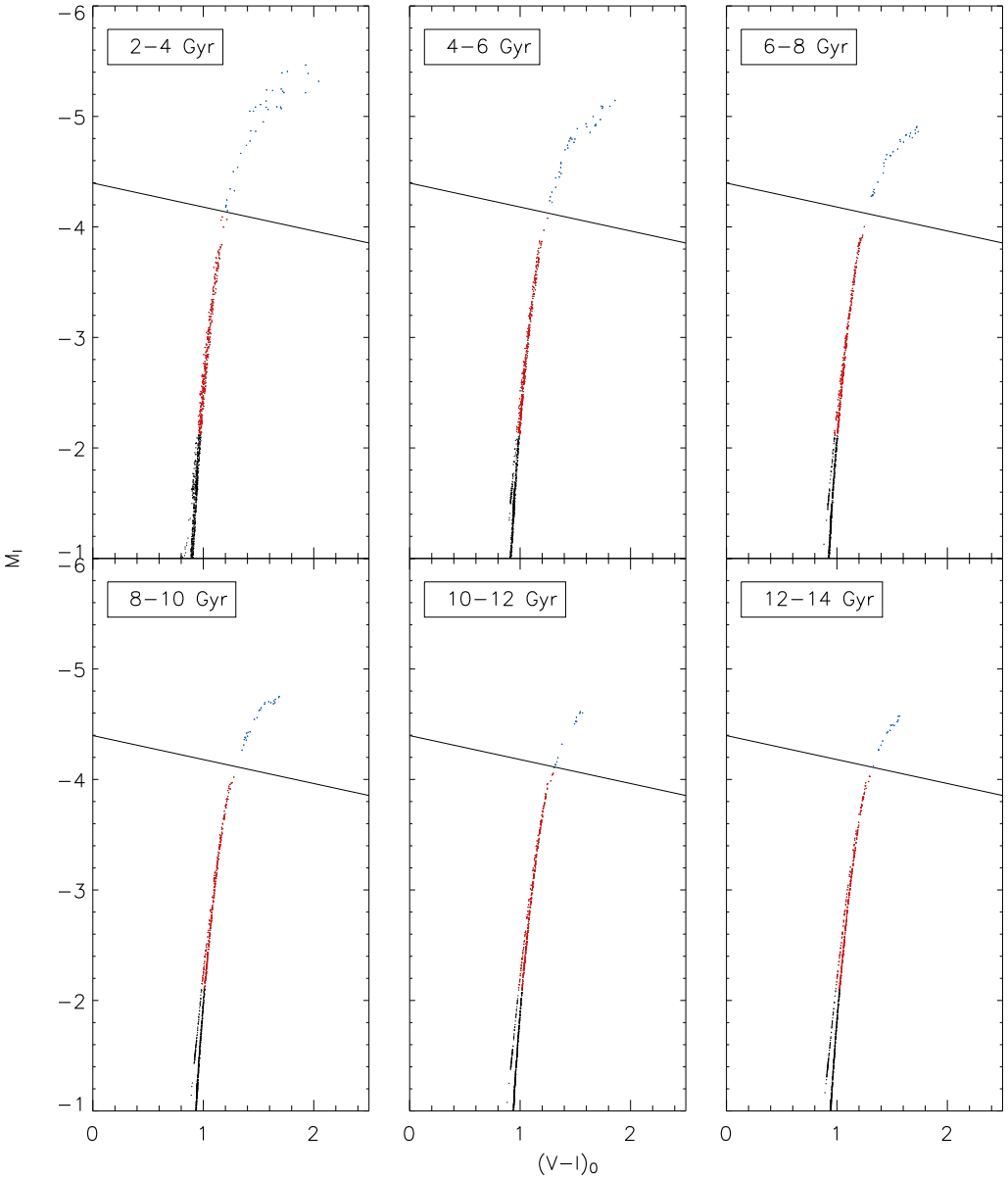

Figure 5.2 CMDs of simulated stars in $(V-I)_0$ versus M_I, where metallicity is fixed at [Fe/H]=-2.0 and the ages are shown in separate plots covering 2 Gyr bins from 2 to 14 Gyr. The diagonal line represents the zero-point calibration of the absolute magnitude of the TRGB from Rizzi et al. (2007) and is used to divide RGB stars from the AGB.

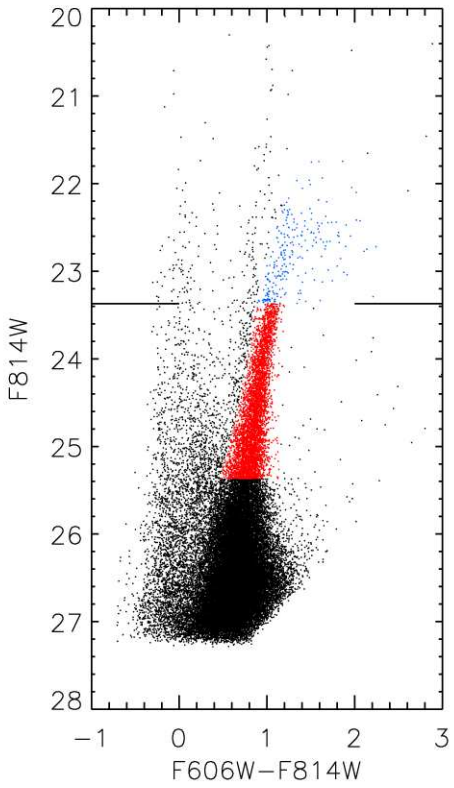

Figure 5.3 CMD of UGC8651 in $F606W - F814W$ vs. $F814W$ from observations with ACS, HST program 10210. The broken horizontal line at $F814W = 23.37$ marks the TRGB. Stars within 2 magnitudes of the TRGB that are identified as members of the RGB are colored red. Stars identified as members of the AGB are colored blue.

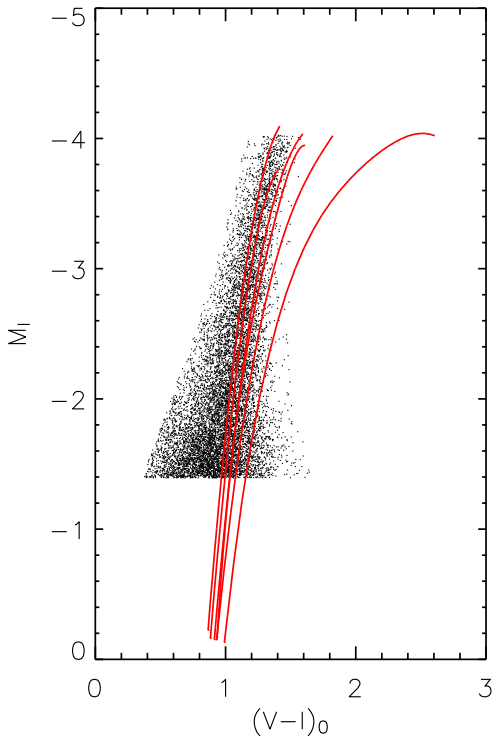

Figure 5.4 CMD of the RGB in UGC8651 in $(V-I)_0$ versus M_I selected to compare with the fiducial loci of the RGB of galactic globular clusters from Da Costa & Armandroff (1990), which are shown as red curves. The metallicities of the clusters used to produce these curves are, from left to right: [Fe/H]= −2.17, −1.91, −1.58, −1.54, −1.29, and −0.71.

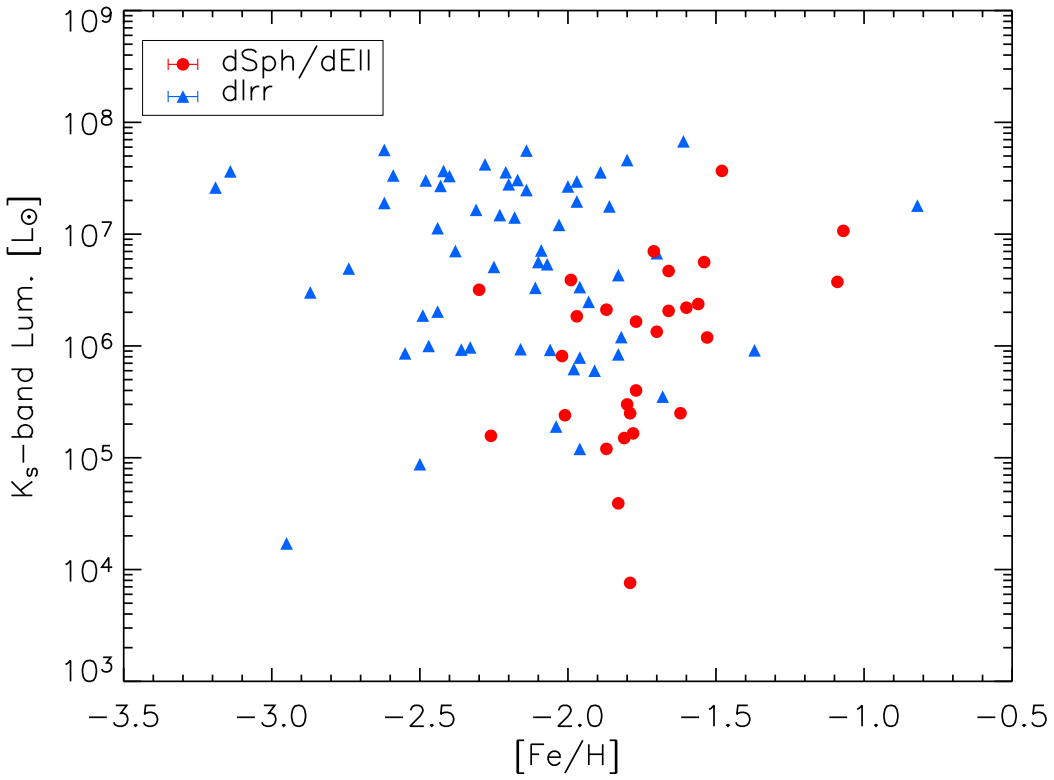

Figure 5.5 K_s-band luminosity vs. photometric metallicity from the color of the RGB of galaxies listed in Table 5.1. Galaxies with morphological type $T \geq 0$ are plotted as blue triangles, while those with $T < 0$ are shown as red circles. The RMS scatter of the metallicity fit is typically 0.05 and and error bars of this size are shown in the legend. However, there may be substantial systematic effects in the metallicity measurements that we do not attempt to display.

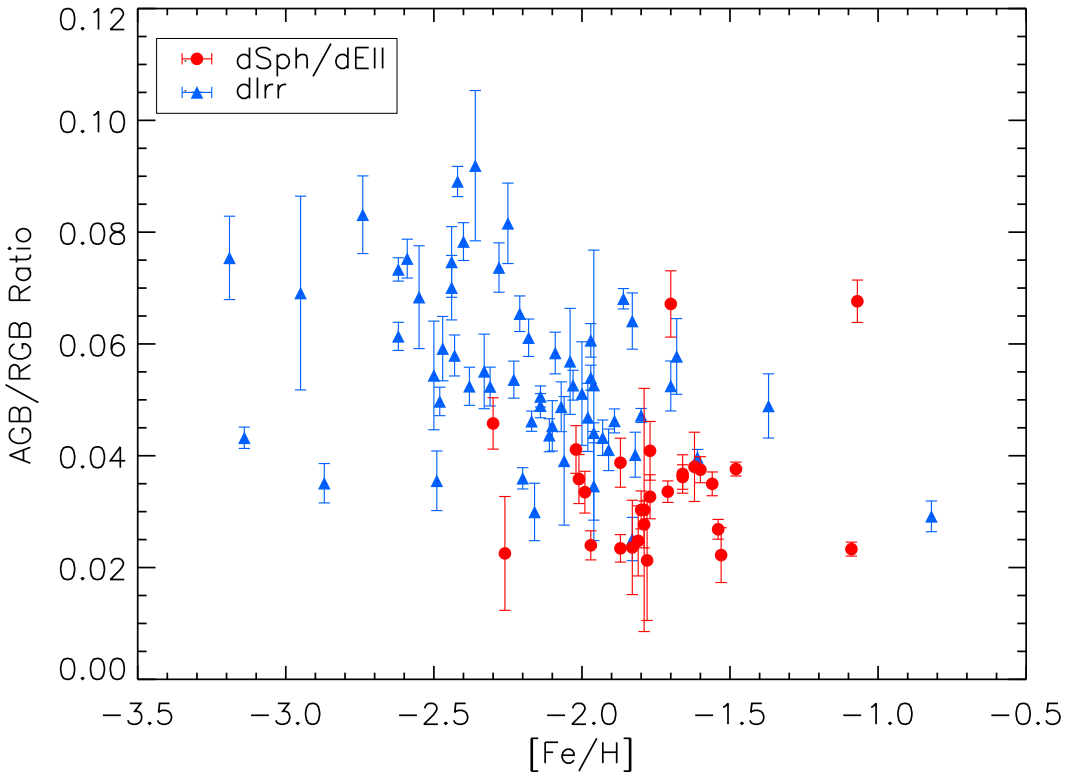

Figure 5.6 AGB/RGB ratios vs. photometric metallicity from the color of the RGB of galaxies listed in Table 5.1. Galaxies with morphological type $T \geq 0$ are plotted as blue triangles, while those with $T < 0$ are shown as red circles. Errors in the AGB/RGB ratio are based on Poisson statistics. The RMS scatter of the metallicity fit is typically 0.05 and and error bars of this size are shown in the legend. However, there may be substantial systematic effects in the metallicity measurements that we do not attempt to display.

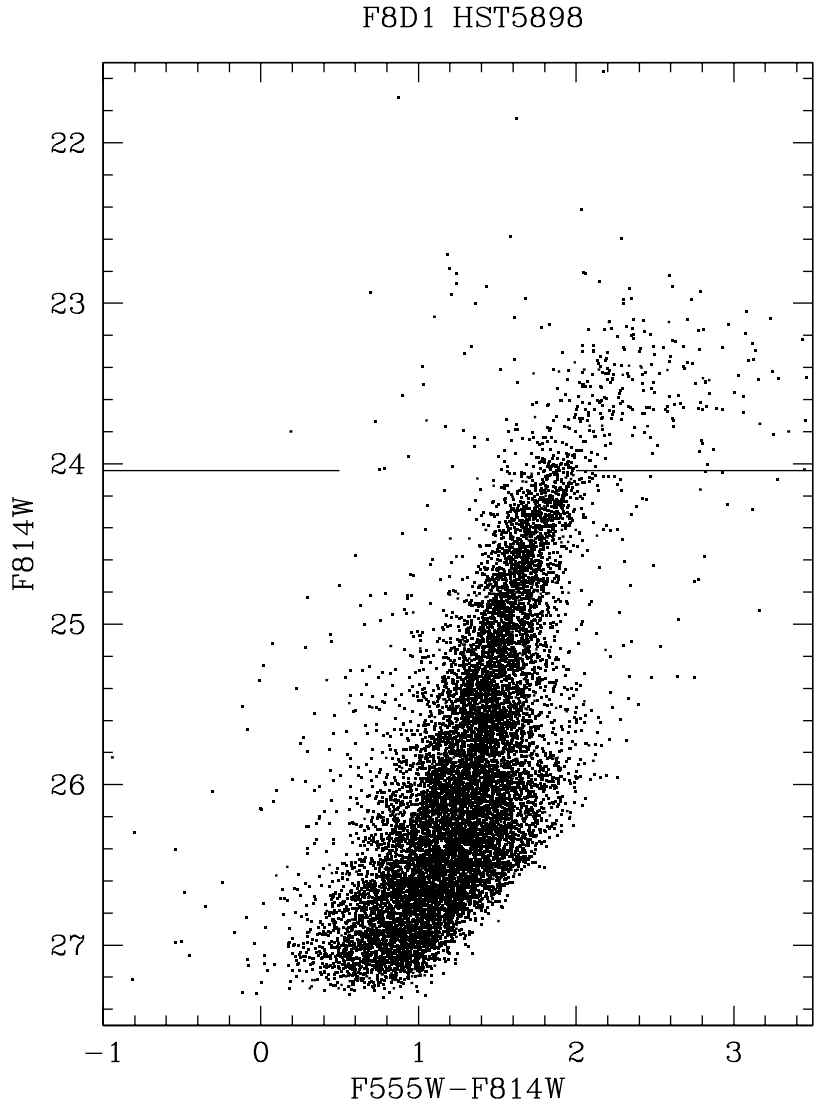

Figure 5.7 CMD of F8D1 in $F555W - F814W$ vs. $F814W$ from observations with WFPC2, HST program 5898. The broken horizontal line at $F814W = 24.04$ marks the TRGB.

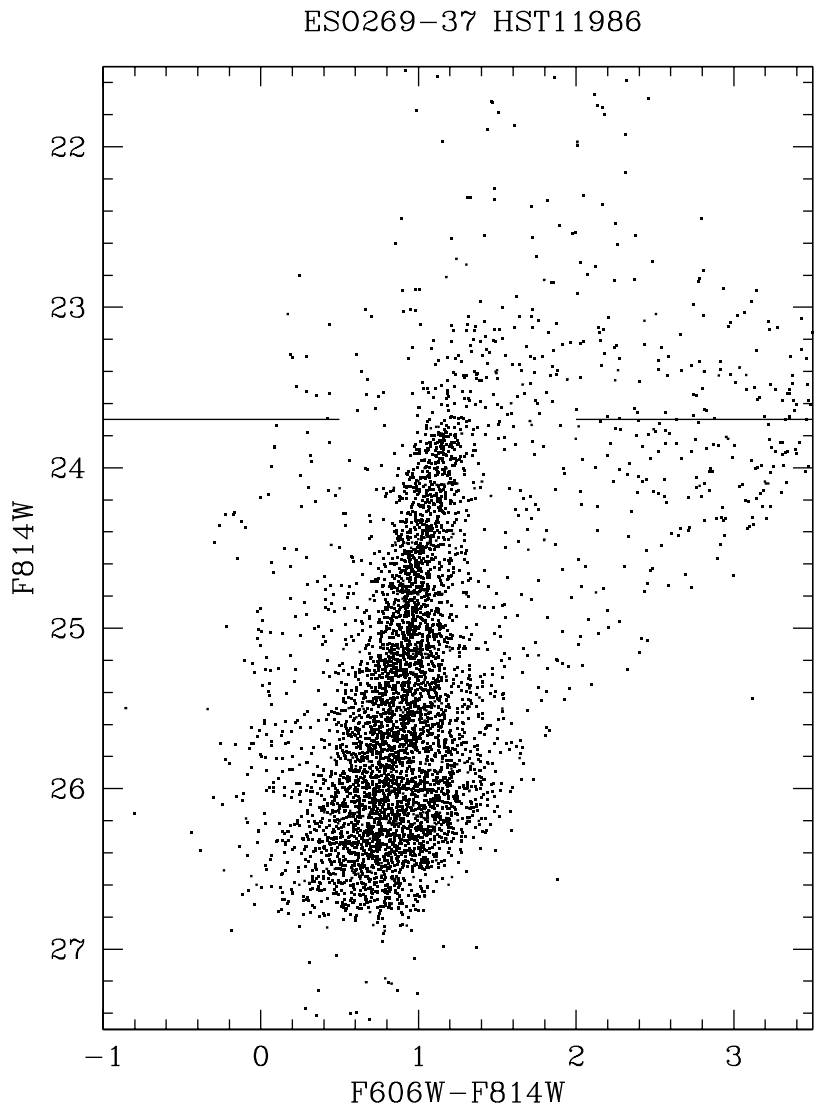

Figure 5.8 CMD of ESO269-37 in $F606W - F814W$ vs. $F814W$ from observations with WFPC2, HST program 11986. The broken horizontal line at $F814W = 23.7$ marks the TRGB.

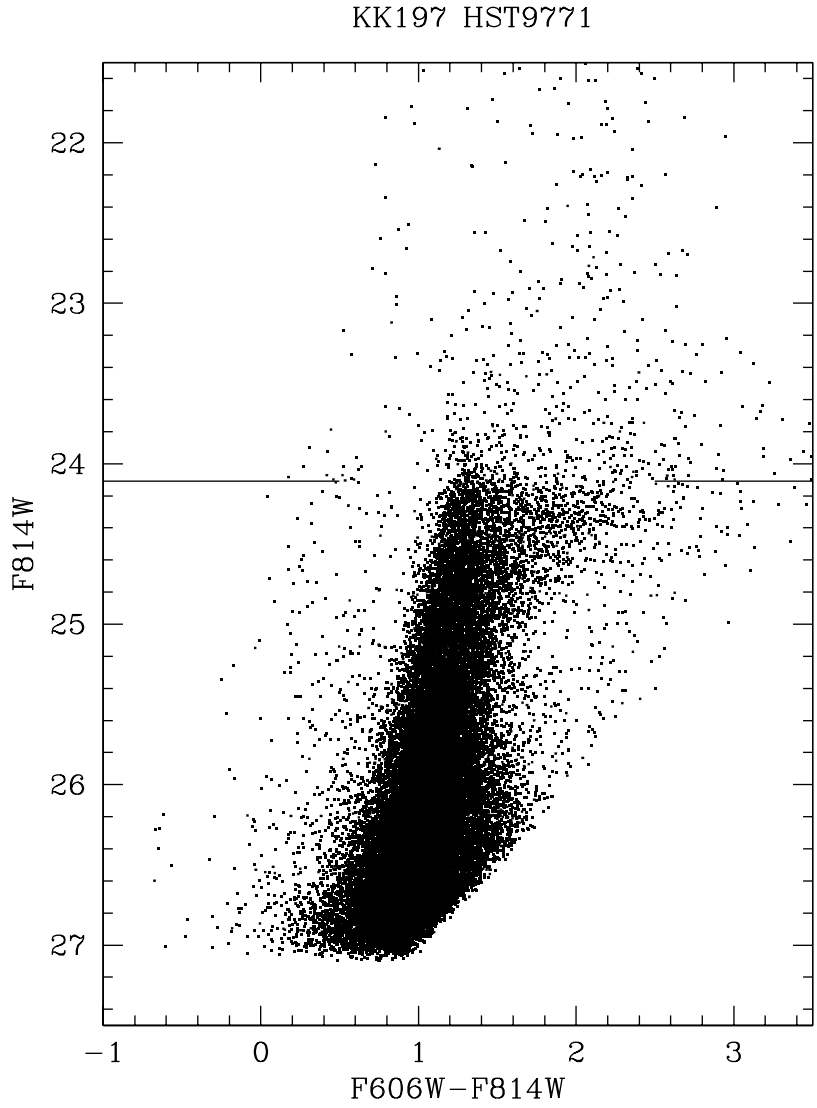

Figure 5.9 CMD of KK197 in $F606W - F814W$ vs. $F814W$ from observations with ACS, HST program 9771. The broken horizontal line at $F814W = 24.11$ marks the TRGB.

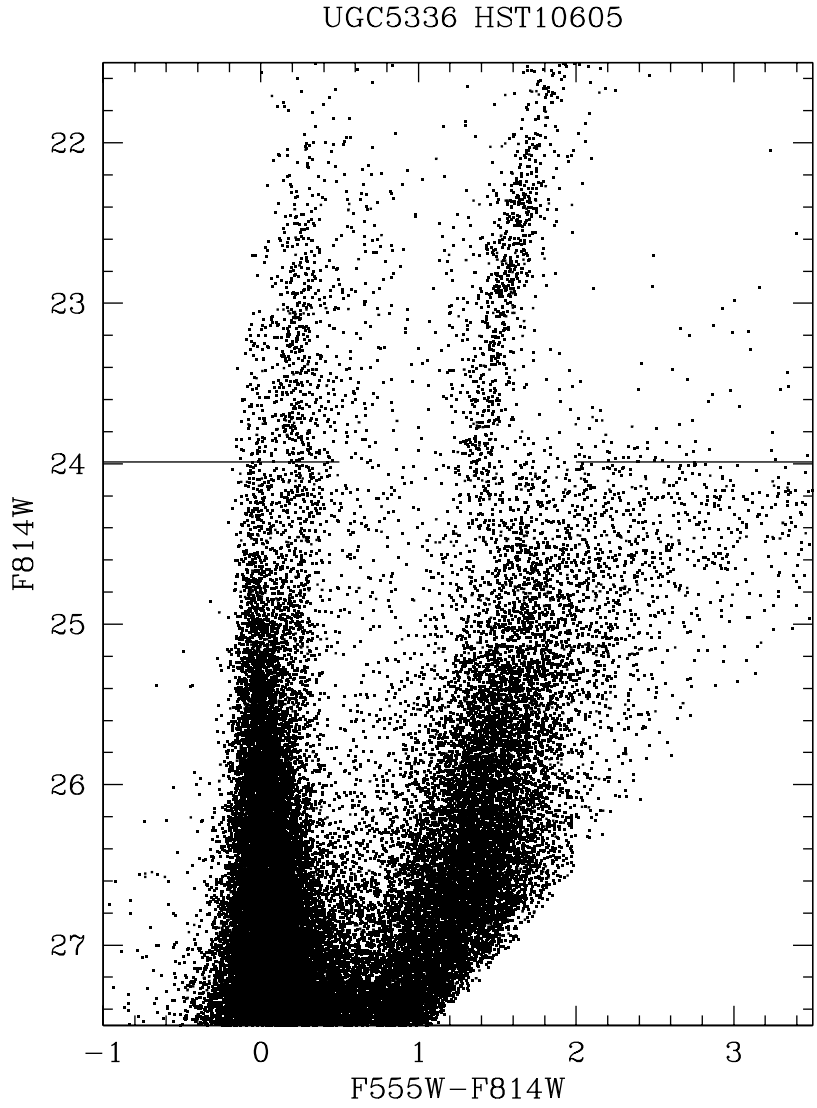

Figure 5.10 CMD of UGC5336 in $F555W - F814W$ vs. $F814W$ from observations with ACS, HST program 10605. The broken horizontal line at $F814W = 23.99$ marks the TRGB.

Chapter 6

Discussion and Summary

TRGB distances measured from CMDs that are built from HST imaging are the backbone of this dissertation. This is true, even when focusing on many populations of stars in addition to the RGB in order to interpret the stellar content of a galaxy, since an accurate distance is crucial in this context. In CMD synthesis, as seen in the case of UGC4879, a reproduction of the observed CMD depends on converting the absolute magnitudes of simulated stars to the apparent magnitudes of the observations. Furthermore, I adopt the apparent magnitude of the TRGB as the border between the AGB and RGB in my analysis of these stars in ∼90 nearby dwarfs. But TRGB distances are arguably most essential to my NAM study of the Local Volume. It is possible to run these simulations with a hodge-podge of galaxy distance estimates, and to a certain extent this is unavoidable, but the more eclectic the distance indicators the greater the risk for systematic biases becomes. Hence, in this study I focus on galaxies located within 4.5 Mpc of the Milky Way, where virtually all known galaxies have TRGB distances. This method is unique in that it is feasible to apply it to every galaxy in that volume. Other precise stellar distance indicators, such as Cepheids and RR Lyraes, are very rare compared to RGB stars, and consequently fewer galaxies have distance measurements of these types. Therefore, it was the goal of this dissertation to obtain HST observations for as many Local Volume galaxies as possible and thereby eventually extend the complete sample from 4.5 Mpc to 10 Mpc. Various factors, notably the 'hiatus' of ACS between 2007 and 2009, limited the number of new observations appropriate for a TRGB measurement that became available during this project. Nonetheless, as of 2012 a significant number of new ACS observations of galaxies with distances between 4.5 and 10 Mpc have recently become available. Moreover, several galaxies that had been previously observed with ACS have new infrared images from Wide-Field Camera 3, and

these demonstrate that this camera is also suitable for measuring TRGB distances out to around 10 Mpc. So the hope for a complete Local Volume sample remains.

The results from the NAM simulations depend on a sample of consistently measured distances, and studies of Local Group dynamics have met some success (e.g. Peebles 2009, 2010). With in-depth studies of the Local Group already underway at the start of this project, I focused my attention on the mass and dynamics on the M81 group. This shift presented some challenges for interpreting NAM. First the group is located about 3.6 Mpc from the Milky Way, and thus towards the edge of the complete volume. Naturally, the NAM catalog includes as many galaxies as possible outside this volume, but some inevitably have less accurate distances than those found closer to the Milky Way, and some of these happen to be relatively close to M81. Second, the radial velocities used as diagnostics of the quality of the NAM results are inevitably somewhat more correlated among the galaxies that are sensitive the M81 group mass than those that trace the Local Group. This is because the M81 tracers are located in the same area of the sky and their distances relative to the Milky Way are similar. Perhaps then, it should not be very surprising that the constraints to the mass of the M81 group identified in Chapter 3 are fairly weak. Similarly, while the general impression of the galaxy orbital paths predicted by NAM are generally stable over a range of masses, the more complex orbits in the central region of the group that need to be built up from the initial predictions are quite sensitive to the adopted mass-to-light ratio. The way forward may come from first modeling the interactions between M81 and M82 as an N-body problem and using this to guide the interpretation of the NAM trials. However, progress may also require filling in and replacing missing or inaccurate distance measurements for galaxies on the far side of M81 as new HST observations become available.

While the history of the dynamics of the M81 group remains uncertain, I was able to draw considerably stronger conclusions about the history of star formation in the nearby dwarf UGC4879. This galaxy is quite isolated compared to most other Local Group galaxies, so it is very unlikely that its SFH is influenced by environmental factors from interactions with other galaxies. It is therefore, noteworthy that both ancient and young stars are visible in its CMD. There is no evidence to suggest that star formation has been ongoing throughout its history, so one might ask what started the recent star formation. The offset between the HI gas and the centroid of the old stars in UGC4879 may point to gas flows as the trigger, though whether this is re-accreted gas or if it is from some other source is currently unknown. I base the conclusion that UGC4879 did not form very

many stars between roughly 1 and 9 Gyr ago on the relatively few AGB stars compared to RGB stars seen in its CMD. This test led to the analyses performed in Chapter 5, and in comparison with that sample the AGB/RGB ratio in UGC4879 is located towards the low end seen among dwarf irregulars. Interestingly, UGC4879 is sometimes classified as a dwarf transitional galaxy morphologically (Kopylov et al. 2008), and thus a middle case between early and late-type dwarfs. At the same time, its AGB/RGB ratio and RGB-color put it close to the region where the early-type dwarfs are concentrated in Figure 5.6.

The characteristics of the AGB and RGB stars in UGC4879 indicate that it shares some similarities with both early and late-type dwarfs. The tools of the AGB/RGB ratio and RGB-color measured from the HST CMDs of ∼90 local dwarfs show a fairly clean segregation by morphological type. In addition to being useful for identifying outlying cases, these measures show an apparent trend as the AGB/RGB ratio generally decreases with increasing metallicity. There is a lot of scatter on along this trend, as seen in Figure 5.6, but it nonetheless is suggestive of differences in the nature of the star formation that took place in the galaxies with high AGB/RGB and low metallicity and those with low ratios but more metals. Age-metallicity degeneracy is wrapped up in the interpretation of this diagram, but it is noteworthy that galaxies with more recent star formation seem to have been less enriched than those that have ceased forming stars. More work is needed to clarify these issues, and some progress is attainable simply by applying similar tests to the CMDs constructed for this dissertation. Recent star formation can be interpreted through counts of massive main sequence stars, as well as supergiants, and blue-loop stars.

The CMDs in my database contain a wealth of information about the target galaxies. I have focused mainly on the RGB stars, which reveal the galaxy distances and can be used as metallicity indicators. By studying the RGB and several other populations in UGC4879 it became clear that the AGB complements information derived from the RGB and I expanded the analysis from these stars to most of the dwarf galaxies in the database. The resource of the CMDs as tools for interpreting a galaxy's stellar content is not near exhaustion. Furthermore, new observations continue to be added to the HST archive and as always the first priority for measurement is a distance via the TRGB method, since a distance is necessary for all subsequent interpretations of the CMD. The combination of new ways to examine the stellar content of the sample and its increasing size means that further knowledge of galaxy evolution is waiting to be derived. The same holds true for dynamical studies that depend on accurate distance information, as TRGB distances continue to be the most widely

applicable technique for Local Volume galaxies. There is much still to be learned from resolved stars in nearby galaxies, including both from completed and future targets of HST observations.

References

Kopylov, A. I., Tikhonov, N. A., Fabrika, S., Drozdovsky, I., & Valeev, A. F. 2008, MNRAS, 387, L45

Peebles, P. J. E. 2009, arXiv:0907.5207

Peebles, P. J. E. 2010, arXiv:1009.0496

Appendix A

TRGB Measurement and Publication Procedures

A.1 Introduction

The process of adding observations to the CMD/TRGB section of the Extragalactic Distance Database involves five phases: obtaining images, measuring photometry and errors with the HSTPHOT (Dolphin 2000) and DOLPHOT software packages, identifying the magnitude of the TRGB with TRGBTOOL (Makarov et al. 2006), converting to a distance measurement, and collecting results and images to be published in the database. The details of the procedures vary depending on filters used ($F555W$ or $F606W$ for color discrimination against $F814W$), number of images to photometer, and camera used (ACS or WFPC2). These largely represent minor variations in calibrations, or a few additional steps, with the exception of differences in cameras in the photometry phase. The two photometry packages differ significantly in that DOLPHOT has a fair number of capabilities unavailable in HSTPHOT.

A.2 Identifying and Obtaining HST Images

The main repository for HST images can be accessed from the Archive Search Website[1], which allows searches based on a large number of parameters. A more graphical search option is available through the Hubble Legacy Archive (HLA)[2], which is used for obtaining HST footprint images and discussed further in the section on preparing additions to the database. The two sites are complementary and both allow downloads of images, but the photometry packages were written before HLA was

[1]See: http://archive.stsci.edu/hst/search.php
[2]See: http://hla.stsci.edu/

operational and they do not recognize the file formats there, so the older HST Search site is described here.

The results of the HST Search are presented in a large table that includes all the salient details of the images: file name, target, coordinates, exposure time, camera, filter, etc. In cases where similar observations have been made of several fields of a galaxy the HLA site becomes useful for a visual representation of, for example, which fields include the core or the halo of the galaxy. Once a set observations has been selected, these can be 'Marked' with checkbox in the leftmost column of the table and then requested by clicking "Submit marked data for retrieval from STDADS." There are a few options for downloading the data, I use the 'Stage' option that requires you to set up an account and retrieve the data from the HST FTP site. Detailed instructions about account setup and downloading are available from this retrieval website.

A.2.1 File Extensions

The retrieval website has a 'File Extensions Requested' section that lists the available file formats. For WFPC2 images click the *"Deliver WFPC2 datasets in Waivered FITS format"*, or for the same result select the 'C0F' and 'C1F' file extensions. After WFPC2 ended operations all images were reprocessed and released in multi-extension FITS format (MEF), which HSTPHOT does not recognize. The reformatted files that have extensions like 'C0M' and 'C1M' will not work with HSTPHOT.

Details of which extensions are used in HSTPHOT and DOLPHOT are given in their respective manuals. Briefly, for WFPC2 the requisite formats are 'C0F' (the data), and 'C1F' (data quality image). For ACS there is no equivalent data quality image, but the data can be photometered from either the 'FLT' (more common) or 'CRJ' extensions.

A.3 Photometry

A.3.1 Preprocessing

After downloading images from the HST FTP site and in preparation for running HSTPHOT/DOLPHOT it is useful to convert the filenames into a more convenient/readable format from the alphabet-soup versions used in the archive. It is good practice to keep the files downloaded

from the archives segregated from the photometered files because HSTPHOT/DOLPHOT *will alter the files it is given.* The way this has been done is by downloading files to a subdirectory called "raw" and then copying and renaming the files to a more readable format into another subdirectory called "reduced." These preprocessing steps, though similar between cameras, are described separately for WFPC2 and ACS below, since different filetypes and software are used.

A.3.2 WFPC2

The main extensions needed to measure photometry in WFPC2 images are "c0f" and "c1f", which are the main image, and image quality files respectively and are delivered in FITS format. Traditionally these files have been renamed (and copied into the "reduced" subdirectory) following the format e.g.: galaxy_propid_exptime_i1.fits, and galaxy_propid_c1f_i1.fits, with 'i1' denoting the first image taken in the $F814W$ filter. The galaxy name, proposal identification number, and exposure time are listed in the header of the FITS files. For completeness, commands for copying these files are included in the example script shown below.

The photometry steps using HSTPHOT described here are not meant to replace the HSTPHOT manual[3], but merely summarize the steps taken in preparing observations for inclusion in the TRGB database. The steps for a typical observation of a galaxy with one image each in a V and I equivalent filter might take the form:

```
cp ../raw/fitsbase1_c0f.fits galaxy_propid_exptime_v1.fits
cp ../raw/fitsbase1_c1f.fits galaxy_propid_c1f_v1.fits
cp ../raw/fitsbase2_c0f.fits galaxy_propid_exptime_i1.fits
cp ../raw/fitsbase2_c1f.fits galaxy_propid_c1f_i1.fits
mask galaxy_propid_exptime_v1.fits galaxy_propid_c1f_v1.fits
mask galaxy_propid_exptime_i1.fits galaxy_propid_c1f_i1.fits
getsky galaxy_propid_exptime_v1
getsky galaxy_propid_exptime_i1
crmask 1.0 3.0 0 galaxy_propid_exptime_v1 0 0 0 0 0
crmask 1.0 3.0 0 galaxy_propid_exptime_i1 0 0 0 0 0
hotpixels galaxy_propid_exptime_v1
hotpixels galaxy_propid_exptime_i1
```

[3]See: http://americano.dolphinsim.com/hstphot/

```
hstphot galaxy.phot 3.0 3.0 -1 0 0 0 0 64 galaxy_propid_exptime_v1 0 0
galaxy_propid_exptime_i1 0 0 "" V I 19 28 -0.5 2.5 0.5 0.5 0.5 0.5
```

The commands 'mask', 'getsky', and 'hotpixels' are simple because they have no parameters to adjust and the only differences would come in cases where there are multiple images per filter, in which case the additional images would be processed as above. The 'crmask' routine is used to find and mask cosmic rays on the images and works best when comparing two or more images in the same filter, though it can be used across multiple filters as well. When for example there are two images in $F814W$ where the second image has been dithered such that a star at (0, 0) pixels in the first image is at e.g. (2, 5) in the second then crmask would be:

```
crmask 1.0 3.0 0 galaxy_propid_exptime_i1 0 0 0 0 0 galaxy_propid_exptime_i2 0 0 0 2
5
```

where the last two of the five digits following the image fits bases define the change in x and y positions. The other three digits control the limits in the magnitudes accepted when accounting for differences in brightness when applying the routine between filters (and set to 0 0 0 when working with one filter), which can be useful for making color images where cosmic rays would be a distraction, but comparing across filters is generally not necessary for generating photometry. The parameters following 'crmask' are called the "reg factor", "σ threshold", and "use min value" and are generally kept at 1.0, 3.0 and 0 respectively.

The 'hstphot' command runs the actual photometry measurements and consequently has many input parameters. It is beyond the scope of this appendix to describe each of these and for the purpose of inclusion in the TRGB database the majority never need to be adjusted. However, we note the following: the 'galaxy.phot' term defines the name of the photometry file to be created, each image fits base is listed followed by two coordinates that describe the dither pattern that works the same way as with 'crmask', the empty quotes allow the specification a reference image for specifying the dither pattern and when left blank as above HSTPHOT takes the first image to be the reference image. After the quotes in the 'hstphot' command come the artificial star test parameters that define the grid of artificial stars to be implanted and measured. It is rare the these parameters would need to be adjusted, but the use of a different filter set or observations of a particularly nearby or more distant galaxy might necessitate changing them. In cases with more than one image

per filter 'hstphot' need only be referred to the new images and how they are dithered i.e.:

```
hstphot galaxy.phot 3.0 3.0 -1 0 0 0 0 64 galaxy_propid_exptime_v1 0 0
galaxy_propid_exptime_v2 0 0 galaxy_propid_exptime_i1 0 0 galaxy_propid_exptime_i2 0
0 "" V I 19 28 -0.5 2.5 0.5 0.5 0.5 0.5
```

where the images are grouped by filter and listed in order of increasing wavelength.

HSTPHOT Output

The results from running HSTPHOT include photometry files (i.e. 'galaxy.phot') and results from artificial star tests (e.g. 'galaxy.phot.fake'). Both outputs are used by the TRGBTOOL package for identifying the magnitude of the TRGB. The real and fake photometry tables are complex in that they contain one line for each star and each line includes a large number of columns. A description of the types of columns produced is given in the HSTPHOT manual and various of these are used by TRGBTOOL, but for the moment it suffices to mention that in a typical run the $F555W/F606W$, and $F814W$ magnitudes are listed in columns 12 and 22, respectively. This is true even if there are multiple images per filter, in which case the combined magnitude of the star across the images is listed for each filter, followed by the results for each individual image. These are the columns that are usually called in the photometry file when plotting the CMD, but HSTPHOT also outputs magnitudes in the Johnson-Cousins system that are listed in the column following the flight magnitudes (i.e. 13 and 23 for V and I).

A.3.3 ACS

As described above, the photometry on the ACS images is usually performed using those with the 'FLT' extension, though 'CRJ' format can also be used. An example script that can be used to run DOLPHOT is shown below; for details on the routines called, see the DOLPHOT manual[4]. In addition to the main DOLPHOT, there is a module that is specific to ACS that must be downloaded that uses point-spread function (PSF) information for specific filters, which are all available through the listed website. Many DOLPHOT routines print a lot of status updates, errors, etc. to the terminal so it is useful to send these to a file, e.g. 'galaxy.log'.

```
touch galaxy.log
```

[4]See: http://americano.dolphinsim.com/dolphot/

```
cp ../raw/fitsbase1_flt.fits galaxy_v1.fits
cp ../raw/fitsbase2_flt.fits galaxy_i1.fits
acsmask galaxy_v1.fits >> galaxy.log
acsmask galaxy_i1.fits >> galaxy.log
calcsky galaxy_v1 15 35 -128 2.25 2.00 >> galaxy.log
calcsky galaxy_i1 15 35 -128 2.25 2.00 >> galaxy.log
dolphot galaxy.phot -pphot.param >> galaxy.log
```

The 'dolphot' command includes a call to a parameter file called 'phot.param.' Many of the parameters included in this file are standard and will not need to be adjusted, but some depend on the particularities of the observations, these are:

```
Nimg = 2
img1_file = galaxy_v1
img1_apsky = 15 25
img1_shift = 0 0
img1_xform = 1.0 0 0
```

where 'Nimg' defines the number of images to photometer (minimum of 2 and almost always a total that is split evenly between two filters). For each image there are four parameters that must be listed: the file name (with '.fits' omitted), the annulus in pixels for measuring the sky background (I have never needed to change this from 15 and 25), the shift relative to the first image (or if specified a reference image) for dithering, and the transformation of the image relative to the reference in terms of magnification, rotation, and cubic distortion (unlikely that this will need to be changed from 1.0 0 0). Hence, beyond making sure that DOLPHOT is pointed to the correct image files, the parameter file also accounts for the dither pattern between images. It is possible to input a sophisticated model of how the images are dithered and distorted with respect to one another, in particular there is a routine called 'acsfitdistort' in the ACS module that takes the coordinates of a particular star (or set of stars) in a reference image and in a test image and calculates a shift, rotation, etc. In practice this has not been necessary, it has been sufficient to locate a star on the first image and measure its shift in all subsequent images and input the results into the 'img*_shift' parameters. For example, a common scenario would involve four images where a star at (0, 0) on

the first V and I images would be located at (5, 60) on the second images in each filter. In this case the shift parameters would be:

```
img1_shift = 0 0
img2_shift = 5 60
img3_shift = 0 0
img4_shift = 5 60
```

where the two V images are listed before the two I images.

DOLPHOT Output

DOLPHOT like HSTPHOT will perform artificial star tests on the images, but not concurrently with calculating the real photometry. Hence, DOLPHOT must be run a second time to get the fake photometry, but because this is by far the most time consuming step it is worth examining the real photometry before initiating this process to make sure it looks reasonable. The overall structure of the photometry file is similar to that from HSTPHOT, just with additional data types presented. For checking the CMD the key columns are usually 14 and 30 for Dolphot 1.0 reductions for the $F555W/F606W$ and $F814W$ magnitudes, with V and I in 15 and 31. Dolphot 2.0 has a new output feature called e.g. Galaxy.phot.columns that lists the data contained in each column, which eliminates the guesswork that had previously been needed to identify the key data (the flight filter magnitudes will almost always be in columns 16 and 29). This raw photometry file typically includes a large number of marginal/bad detections so it is useful to cull these using various parameters, such as by requiring that: $\chi \leq 2.5$, Sharpness$^2 \leq 0.09$, Type≤ 2, Signal-to-Noise≥ 5 in both filters, and the 'PSF C' parameter is 0 in both filters (DOLPHOT manual for details). In Dolphot 1.0 the columns of χ, Sharp, and Type are 5, 7, and 11 respectively, while S/N is in columns 18 and 34, and PSF C is listed in 26 and 42. For Dolphot 2.0 the PSF C parameter has been eliminated but the other parameters remain and can usually (check the .columns file to be sure) found in columns 5, 7, 11 for χ, Sharp, Type, and S/N in columns 20 and 33. If the CMD from the photometry file looks as expected then it is time to characterize the errors.

DOLPHOT Fake Photometry

After confirming that DOLPHOT measured the photometry as planned, it can be re-run to perform artificial star tests on the images. There a few ways to define the range of artificial stars to be used in testing, the method we use takes the photometry results as an input, which is a two step process, the result of which is fed to DOLPHOT 1.0 as follows:

```
awk '$5<=2.5 && $7*$7<=0.09 && $11<3 && $14<90 && $30<90 && $18>=5 && $34>=5
{print $1,$2,$3,$4,$14,$14-$30}' < galaxy.phot > galaxy.xy
acsfakelist galaxy.phot F606W F814W 20 30 1.0 2.0 -USEXY=galaxy.xy -NSTAR=100000 >
galaxy.fakein
dolphot galaxy.phot -pphot.param FakeStars=galaxy.fakein > galaxy.fakelog
```

where the 'awk' command rewrites the photometry file so it can be read by 'acsfakelist', and the limits are given so that only the well-detected stars are included (and described in the previous section). As mentioned in the previous section χ, Sharp, and Type are normally in the same columns between versions 1.0 and 2.0 of Dolphot, but the flight magnitudes change from 14 and 30 to 16 and 29, and the S/N columns switch from 18 and 34 to 20 and 33. Note that the 'acsfakelist' command is the only place where the filters being used is explicitly defined so it is easy to forget to update this when copying code between observations where the filters have switched. The end result of this process will be the production of a large file called e.g. 'galaxy.phot.fake,' which with some modification can be input into TRGBTOOL so that the photometric errors, completeness, and crowding can be characterized.

A.4 Identifying the TRGB

The TRGBTOOL software package takes the real and fake photometry measured by HSTPHOT and DOLPHOT and uses a maximum-likelihood fitting technique to determine the magnitude of the TRGB. Dimitry Makarov wrote the the software for use within Matlab, so while the photometry programs are freely available this software requires a Matlab license. This limits the availability of TRGBTOOL and I have only ever used it on the computer: opik.ifa.hawaii.edu.

A.4.1 Configuring TRGBTOOL

In addition to needing a copy of Matlab several parameter/path files need to be configured to run TRGBTOOL. These are: 'fakeread.m', 'hstphotdata.m', 'hstphotfake.m', 'pathdef.m', 'photread.m', and 'tblselect.m.' Though all these files are required to run TRGBTOOL, in practice only 'hstphotdata.m' and 'hstphotfake.m' need to be adjusted regularly, because these define which columns in the photometry files contain the required data. From the photometry file TRGBTOOL reads: the χ, sharpness, and type parameters, as well as the V-equivalent flight ($F555W$ or $F606W$) magnitude and error, and the I-equivalent flight magnitude and error. For WFPC2 data these are typically listed χ, sharp, type, $F606W$ magnitude, $F606W$ uncertainty, $F814W$ magnitude, and $F814W$ uncertainty in columns: 4, 6, 9, 12, 14, 22, and 24. It is of course possible to use other filters or ground-based magnitudes in TRGBTOOL, but the variables it looks for happen to be called 'F606' and 'F814.' Also there are some photometry files in the database that were made with an older version of HSTPHOT that did not give as many columns so it is sometimes necessary to adjust the column numbers called, for example one of the more common older versions has the $F814W$ magnitude and uncertainty in columns 21 and 23, with the other called columns remaining the same. For ACS results with DOLPHOT the most common configuration has χ, sharp, type, $F606W$ magnitude, $F606W$ uncertainty, $F814W$ magnitude, and $F814W$ uncertainty in columns: 5, 7, 11, 14, 16, 30, and 32 (5, 7, 11, 16, 18, 29, and 31 with Dolphot 2.0). However like with older versions of HSTPHOT there exist other possible sequences for where these terms are located in the photometry file. The 'hstphotfake.m' file calls the same data from the fake photometry file with the addition of the "initial" or true magnitude of the test star that is to be measured. With results from HSTPHOT the true $F606W$ magnitude, the true $F814W$ magnitude, χ, sharp, type, recovered $F606W$ magnitude, $F606W$ uncertainty, recovered $F814W$ magnitude, and $F814W$ uncertainty are usually listed in columns: 9, 10, 14, 16, 19, 22, 24, 32, 34.

For ACS fake photometry from DOLPHOT the process of feeding the results to TRGBTOOL is more complicated. This is because it was written with HSTPHOT in mind, and one thing that changed with DOLPHOT is how the results of the artificial star tests are presented. The DOLPHOT results give a true initial magnitude and a recovered magnitude and uncertainty for each image, while TRGBTOOL wants the combined recovered magnitude across all images in a filter. The work-around comes from converting the recovered raw counts in each image into an overall magnitude.

To complicate things further, this only works if the star is appropriately recovered as measured by e.g. the χ, sharpness, and type parameters, and the column number of these values varies depending on the number of images photometered. The solution to this problem that I use is to maintain separate scripts for application depending on whether the observations include 2, 4, 6, etc. images. An example for when the observations include four images with Dolphot 1.0 is given below:

```
awk '{dv=99.999; di=99.999} $17<=2.5 && $19*$19<=0.09 && $23<=2 && $30>=5 &&
$39==0 {dv=-2.5*log($24/($5+$7))/log(10)} $17<=2.5 && $19*$19<=0.09 && $23<=2 &&
$46>=5 && $55==0 {di=-2.5*log($40/($9+$11))/log(10)} {printf "%6.3f %6.3f %6.3f
%6.3f %6.3f %6.3f\ n",$6,$10,$26,dv,$42,di}' < galaxy.phot.fake >
galaxy.phot.fake2
```

With four images using Dolphot 2.0 this changes to:

```
awk '{dv=99.999; di=99.999} $17<=2.5 && $19*$19<=0.09 && $23<=2 && $32>=5 &&
$36==0 {dv=-2.5*log($24/($5+$7))/log(10)} $17<=2.5 && $19*$19<=0.09 && $23<=2 &&
$45>=5 && $49==0 {di=-2.5*log($37/($9+$11))/log(10)} {printf "%6.3f %6.3f %6.3f
%6.3f %6.3f %6.3f\ n",$6,$10,$28,dv,$41,di}' < galaxy.phot.fake >
galaxy.phot.fake2
```

This script pulls the true magnitudes and the recovered magnitudes and uncertainty into a six column file that can be read by TRGBTOOL by calling columns 1 through 6 in the 'hstphotfake.m' file.

A.4.2 Running TRGBTOOL

With the Matlab files properly configured to read the photometric output TRGBTOOL can be run as a GUI within Matlab to measure the magnitude of the TRGB. Once TRGBTOOL has been launched it displays various buttons parameters and plot fields. The photometry files can be loaded into the program by clicking the load button. The real photometry file is loaded first, then the fake photometry. Note that by default the load window is set to filter by extension and list only ones with extensions that it thinks are appropriate ('.phot', '.phot2', '.fake', '.mat') so if the files have different extensions this option will have to be turned off. Once loaded, the data will be displayed in a CMD, with a plotting range that can be adjusted by clicking the plot. The axes are set to refer to $F606W$ and $F814W$ regardless of which filters have been fed to the program (though this can be adjusted using the configuration files). To the right of the CMD, up to four plots are shown: a number count

luminosity function, the luminosity function in log-space, a completeness function, and a plot of the bias. All of these are plotted against the magnitude of the longer wavelength input filter, usually $F814W$ (which is what the x-axis reads in any case). The display of these plots can be turned on or off with the small buttons in the upper-right corner of the TRGBTOOL window. In addition to the luminosity function, shown in blue, its derivative is shown in green. The rapid increase in the density of stars at the onset of the RGB thus appears as a peak in the derivative of the luminosity function. The range of magnitudes plotted in the right-hand plots can be adjusted by dragging the horizontal dashed-lines in cyan on the CMD up and down. There is also a blue limit to the data shown in these plots displayed by a vertical dashed-line, that is set to $F606W - F814W = 0.6$ by default, but can be dragged left or right to change this limit.

Following setting the plot ranges to appropriate values the range of data to which the broken power-law will be fit to the luminosity function needs to be defined. This is done by clicking the luminosity function near the magnitude of the TRGB. This will be shown as a set of red vertical lines on the luminosity function and the stars within the range to be considered will be turned red on the CMD. On the left of the window the 'Parameters' box lists the magnitude of this initial guess at the TRGB, as well as the slopes of and break in the power law 'a', 'b', and 'c' (see: Makarov et al. 2006), and the range to be fit. Clicking the 'Fit' button will take these parameters and perform a maximum likelihood fit to the luminosity function. The results from the fit are displayed in the box below the parameters, given as a best estimate followed by lower and upper bounds given in parentheses. All the values displayed can be useful in evaluating the quality of the fit and the resulting power-law is plotted on the luminosity function window in cyan.

In easy cases it will be possible to generate an acceptable fit to determine the magnitude and color of the TRGB in one iteration. When the TRGB is less obvious there are a few techniques that can be used to get an acceptable fit. One option is to fix the 'a', and/or 'c' parameters that define the slope of the power law at magnitudes fainter and brighter than the TRGB respectively. These slopes are expected to equal 0.3 (Makarov et al. 2006). Another adjustment can be made by changing the range in $F814W$ to which the fit is applied. For example, the fit is a power law so the plot of the log of the luminosity function should resemble straight lines on either side of the break at the TRGB. If either of these regions appears strongly nonlinear in this plot then it might be useful to exclude this part from the fit. Once a good fit has been found the results can be saved as a '.mat' file using the 'Save' button.

A.4.3 Spatial Masking to Identify the TRGB

Some galaxies have large amounts of recent star formation, which increases the number of non-RGB stars located near the tip on the CMD. These tend to be large galaxies where there may be several HST observations available in the archive, and if so then the TRGB will be more identifiable in those fields targeting the galaxies' stellar halos. However, when the TRGB is still obscure it can be useful to apply this principle within the HST observation itself, i.e. exclude the areas that have the highest density of stars. At the opposite end of the spectrum, the less massive galaxies sometimes have their TRGB obscured not by other stars in these galaxies but by Milky Way stars. Here the tip can be made more obvious by excluding the areas of low stellar density and focusing on the core of the target galaxy. The procedures for picking out either the cores or the halos of the target galaxies are essentially the same.

This technique does not alter how the photometry is run but merely chooses to include or exclude stars based on their X, Y-positions in the image as measured by HSTPHOT/DOLPHOT. I have written an IDL program that starts by displaying a scatter plot of these positions, along with the CMD. The region on the scatter plot to be included can be defined in a number of ways, but most commonly (and simply) I define a box based on maximum and minimum pixel positions in X and Y, and then use this range to re-plot the CMD. This re-plotting is repeated until a satisfactory balance is struck between maintaining a well-populated RGB and excluding as many non-RGB stars as possible. Once the optimal region is defined, I write out a photometry file for input into TRGBTool. While TRGBTool will work with this new photometry file and the original fake photometry file, it is best to trim the fake file to match the region used in the new photometry file. This is particularly true for the large galaxies where there may be significant crowding in areas of the image that have now been excluded from consideration.

A.5 Measuring a TRGB Distance

The measurements of the color and magnitude of the TRGB taken with TRGBTOOL can be used to estimate its distance modulus using the zero-point calibrations of Rizzi et al. (2007). The calibration depends on the filters and cameras used. We use their calibration of the absolute magnitude and correct for foreground extinction using values derived from the dust maps by Schlegel et al. (1998)

to produce a distance modulus using the following equations:

$$DM = m_{TRGB} - A_I + 4.05 - 0.217[(V-I) - (A_V - A_I) - 1.6] \tag{A.1}$$

$$DM = F814^{WFPC2}_{TRGB} - A_{814} + 4.01 - 0.18[(F555 - F814) - (A_{555} - A_{814}) - 1.58] \tag{A.2}$$

$$DM = F814^{WFPC2}_{TRGB} - A_{814} + 4.01 - 0.15[(F606 - F814) - (A_{606} - A_{814}) - 1.12] \tag{A.3}$$

$$DM = F814^{ACS}_{TRGB} - A_{814} + 4.06 - 0.15[(F555 - F814) - (A_{555} - A_{814}) - 1.74] \tag{A.4}$$

$$DM = F814^{ACS}_{TRGB} - A_{814} + 4.06 - 0.2[(F606 - F814) - (A_{606} - A_{814}) - 1.23] \tag{A.5}$$

where in the first equation m_{TRGB} is the apparent magnitude of the TRGB in Cousins I-band, $(V-I)$ is the color of the TRGB, and A_V and A_I are the respective foreground extinction terms, all these values are repeated in the following equations but adjusted for their respective filters and cameras. The usual procedure for estimating the foreground extinction is to use the IPAC DUST interface[5] that is based on Schlegel et al. (1998) to get a measurement of $E(B-V)$ at the coordinates of the observations (the reported mean value). To convert the extinction values to the appropriate filter Schlegel et al. (1998) reports the following normalization factors:

$$A_V/E(B-V) = 3.315 \tag{A.6}$$

$$A_I/E(B-V) = 1.940 \tag{A.7}$$

$$A_{555}/E(B-V) = 3.252 \tag{A.8}$$

$$A_{606}/E(B-V) = 2.889 \tag{A.9}$$

$$A_{814}/E(B-V) = 1.948 \tag{A.10}$$

When plugging in values from TRGBTOOL remember that the RGB gets redder at brighter magnitudes so when calculating the error range the lower (brighter) value for the apparent magnitude of the TRGB should be paired with the higher (redder) estimate of the color and vice versa.

[5]See: http://irsa.ipac.caltech.edu/applications/DUST/

A.5.1 Reddening Estimates from Main Sequence

In some cases where there are large amounts of reddening, such as with IC10 (PGC 1305), it is useful to estimate reddening directly from Main Sequence on the CMD. This can be done by finding a comparison galaxy with similar populations and presumably similar internal reddening that has a low amount of foreground reddening and is observed in the same filters as the test galaxy. The relative offsets in the color of the Main Sequence between the two galaxies can be used to estimate the reddening of the test galaxies. Most galaxies are located behind only a small amount of foreground dust, so this technique has so far only been applied in a few cases.

To determine the color of the Main Sequences of the heavily and minimally reddened galaxies, we focus on the blue edge or Zero-Age Main Sequence. In order to sample the similar populations we define a slice of the CMD that is between the TRGB and 1 magnitude brighter and a plot a histogram of the color of these stars. The bluest sharp increase in the population is taken as the color of the Main Sequence. The minimally reddened comparison galaxies should have observations in the same camera and filters as the target. For ACS and F606W-F814W we use IC1959 (Program 10210), which has a blue edge at $F606W-F814W$=-0.225 (using 0.025 mag bins), the Schlegel et al. (1998) foreground reddening for this galaxy is $E(B-V)$=0.011 so using the above equations, take the de-reddened color to be -0.235. Similarly, for ACS with $F555W-F814W$ using UGC4305 from Program 10605, has a zero-age color at about $F555W-F814W$=-0.300, with $E(B-V)$=0.0316, then its de-reddened color is -0.341. The difference between these colors and that of a more obscured galaxy is e.g. $(A_{606}-A_{814})_{Target}$. For example, if the blue edge of UGCA86 is F606W-F814W=0.65 then $(A_{606}-A_{814})_{UA86}$=0.885, which can be converted to get $E(B-V)_{UA86}$=0.941. In this case, the estimate is close to the Schlegel et al. (1998) value of $E(B-V)$=0.933, indicating that the reddening is dominated by the foreground, rather than being internal to UGCA86.

A.6 Presenting Resulting Distances

The CMD/TRGB database consists of two levels, the top level is built from a table file that lists all the values relevant to the distance measurement, and the second level consists of many webpages that contain information on individual galaxies, including their CMD, photometry file, observation footprint image, and a pseudo-color image of the galaxy. Thus the process of adding a new galaxy

to the database splits into parts: the addition of an entry to the data table, and the construction of a galaxy webpage.

A.6.1 The Database File

The database bar file that is used to build the table on the website consists of 27 fixed width columns. These are listed in Table A.1. The galaxy PGC number is the key identifier for each galaxy as it is the index used to cross reference galaxies between the various sections in EDD. In the Name column we list the galaxies' common names, this is usually, but not always, the name chosen by the observers from the original HST program listed in column 4. Currently the cameras used are either WFPC2 or ACS, though data from WFC3 could be added in the future (which would necessitate adding a number of new columns to the table). Columns that are listed in blocks of three contain a best estimate, a lower bound, and upper bound listed in that order and are based on the output of TRGBTOOL. Galaxies observed in $F606W$ tend not to be observed in $F555W$ so each galaxy will have entries in columns 9-11 and blanks in 12-14 or vice versa. To aid comparisons with other studies we convert the TRGB results from the HST flight filters to Johnson-Cousins V and I using the prescriptions from Dolphin (2000) and Holtzman et al. (1995) for WFPC2, and Sirianni et al. (2005) for ACS. These conversion are done before reddening is taken into account, and are in VEGA magnitudes:

$$\text{WFPC2}, I = F814W - 0.062 \times (V-I) + 0.025 \times (V-I)^2 \tag{A.11}$$

$$\text{WFPC2}, V = F555W - 0.052 \times (V-I) + 0.027 \times (V-I)^2 \tag{A.12}$$

$$\text{WFPC2}, V = F606W + 0.254 \times (V-I) + 0.012 \times (V-I)^2, \text{where}\,(V-I) < 2.0 \tag{A.13}$$

$$\text{WFPC2}, V = F606W - 0.247 \times (V-I) + 0.065 \times (V-I)^2, \text{where}\,(V-I) > 2.0 \tag{A.14}$$

$$\text{ACS}, I = F814W - 0.005 - 0.014 \times (V-I) + 0.015 \times (V-I)^2, \text{where}\,(V-I) > 0.1 \tag{A.15}$$

$$\text{ACS}, V = F606W - 0.067 + 0.34 \times (V-I) - 0.038 \times (V-I)^2, \text{where}\,(V-I) > 0.4 \tag{A.16}$$

$$\text{ACS}, V = F555W + 0.011 - 0.106 \times (V-I) + 0.013 \times (V-I)^2, \text{where}\,(V-I) > 0.4 \tag{A.17}$$

These equations can be solved iteratively, in pairs where the initial value used in the $(V-I)$ terms is taken to be the color of the TRGB in the flight filters and then updated for the second iteration

Table A.1. TRGB Table Columns

1	PGC
2	1=Public/0=Private
3	Name
4	Alternate Source (e.g. ANGST)
5	Distance in Mpc
6	HST Program No.
7	Camera
8-10	$F814W_{TRGB}$
11-13	$(F606W - F814W)_{TRGB}$
14-16	$(F555W - F814W)_{TRGB}$
17-19	I_{TRGB}
20-22	$(V - I)_{TRGB}$
21	$E(B-V)^1$
22	$E(B-V)^2$
23	A_{814}
24	M_{TRGB}
25-27	Distance Modulus

using the resulting V and I outputs. Within the limited color range from which a galaxy's TRGB is observed a solution should converge in at most ten iterations.

Following the Johnson-Cousins magnitudes in the table are reddening and extinction values, most of which are based on the maps by Schlegel et al. (1998). But as described above, in some cases where reddening is high, it is estimated based on the observed color of Main Sequence stars. Those galaxies that have a Main Sequence based estimate will have an additional E(B-V) value listed in column 22, which will be taken as the preferred value for calculating the distance modulus. Columns after the E(B-V) entries, will include these in their calculations, these are: A_{814}, M_{TRGB} and distance moduli, which are all calculated using the equations listed in previous sections.

A.6.2 The Galaxy Webpages

Each entry in the database table links to a webpage that contains images and data relevant to the distance measurement, these are: CMDs, a link to the HSTPHOT/DOLPHOT photometry file, an image showing the HST footprint of the observations, and a pseudo-color image made from the HST images themselves. The process for creating each of these components is described here. We have implemented a naming convention of appending ".WEB" as a suffix to the files

when they are ready to be published and these should follow the format: Galaxy_cmd.gif.WEB, Galaxy.phot.WEB, Galaxy.jpeg.WEB, Galaxy_color.jpg.WEB, and Galaxy_color600.jpg.WEB for the CMD, photometry, footprint, full-size color image, and preview-size color image, respectively.

Photometry File and CMD

After appending the suffix to the photometry file no further action is needed to prepare it for publication. The CMDs that are created using these files are made using Supermongo. This software package is well-documented so suffice it to describe the main attributes of the CMDs on EDD. These plot $F555W-F814W$ or $F606W-F814W$ vs $F814W$. The magnitudes are always listed in order of increasing wavelength in the HSTPHOT/DOLPHOT output, and with the flight magnitudes in the column preceding the Johnson-Cousins magnitudes, usually the filght magnitudes will be columns 12 and 22 from HSTPHOT and 14 and 30 from DOLPHOT. The CMDs in EDD all use the flight magnitudes and the axes are labeled as such. Recall that DOLPHOT includes a large number of marginal detections in its output so it may be useful to cull these using the parameters described in the 'DOLPHOT Output' section above. The title of the CMD is given as "Galaxy HSTXXXX" where 'XXXX' is the observation program number. The standard axes limits run from -1 to 3.5 on the horizontal axis and the vertical axis range varies depending on the distance of the galaxy but encloses six magnitudes and often runs from $F814W$=21.5 to 27.5. A plot with 4.5 mags on the horizontal axis and 6 mags on the vertical axis will have even spacing by using the standard Supermongo vertical plotting range of 3500 to 31000 and the horizontal plotting area from 7250 to 27517. The magnitude of the TRGB is noted on the diagram by plotting two horizontal line segments at that location, one running from -1 to 0.5 and the other from 2 to 3.5. A macro for saving a postscript file of the CMD of UGC4879 observed in program 11584 and photometered with DOLPHOT 1.0, with the TRGB at $F814W$=21.63 might be:

```
#plot UGC4879


plot
   data ‘‘UGC4879_11584.phot’’
   read v 14
   read i 30
   set vi=v-i
```

```
set tip=21.63
set left=-1 0.5
set right=2 3.5
dev postencap UGC4879_cmd.ps
lweight 1
limits -1 3.5 27.5 21.5
ticksize 0.2 1 0.2 1
window 1 1 1 1
location 7250 27517 3500 31000
ptype 4 3 expand 0.4
connect left tip
connect right tip
points vi i
lweight 2
expand 1.2
box
xlabel F606W-F814W
ylabel F814W
toplabel UGC4879 HST11584
dev x11
```

This macro saves a postscript file of the CMD which is useful for many purposes, but not for the web, where the preferred filetype for this type of image is as a 'gif.' The easiest way to convert the file is from the command line as e.g.:

```
convert UGC4879_cmd.ps gif:UGC4879_cmd.gif.WEB
```

Footprint Images

Images showing the location and orientation of the HST observations on a digital sky survey image are available through the Hubble Legacy Archive[6]. Searching by galaxy name often works well, but in cases where many observations of a particular galaxy have been taken it can be useful to search by the coordinates of the observations. The advanced search feature allows the user to restrict which

[6]See: http://hla.stsci.edu/

camera footprint to display, and the footprints on EDD only show those from the camera used in the observations in question. Additionally, the radius of the image can be set and the standard scale used in EDD is 0.2 degrees. Once the image and footprints are properly displayed, clicking on the footprint of the observations used will turn that footprint yellow, at which point the image will be ready for downloading and inclusion in EDD. When there is some question about which footprint is the correct one it can be useful to browse the list of observations under the 'Inventory' tab, clicking on the correct one in this list will also turn its footprint yellow.

A software update implemented for HLA website in 2011 uses a version of Flash that prevents the footprint images from being downloaded from the browser. It is possible to work around this by using an external "Print Screen" or screen capture program, but this is unfortunately a non-ideal solution for the long term.

Pseudo-Color Images

Color images are made from the HST observations by creating a file in Photoshop that combines inputs from a V image, an I image and a combination that takes the mean between the two and assigns these to the blue, red and green channels, respectively. The best files to use to create these images from ACS observations are the drizzled, cosmic ray-cleaned images available through the HST archives in the 'DRZ' format. For WFPC2 images the process is more involved. HSTPHOT is needed to prepare the images. Most of them will need to be cleaned of cosmic rays using the 'crmask' procedure. When there is only one image per filter then this process is complicated by the need to specify an acceptable color range. Details about this are given in the HSTPHOT manual. After masking the cosmic rays the images need to be adjusted so that they display all four of WFPC2's chips concurrently, this is achieved with the 'hstmosaic' procedure, again see the HSTPHOT manual. Once they have been cleaned and mosaiced, the WFPC2 images are ready for Photoshop.

Photoshop does not normally work with FITS images, so it must have an extension called FITS Liberator, developed by the European Space Agency[7]. The ESA also gives step-by-step instructions for creating color images from HST images[8], and these are the procedures that we follow for inclusion in EDD. These instructions include a Photoshop "Action" that can be downloaded and used to automate several of the colorizing steps. The only deviation from these procedures comes

[7]Available at: http://www.spacetelescope.org/projects/fits_liberator/
[8]See: http://www.spacetelescope.org/projects/fits_liberator/stepbystep/

from creating a mean image to stand in for the green channel. After following ESA's steps 1-3 to assemble the two images as separate layers in a single file a third layer can be created by using Photoshop's 'Image Calculations' module available in the menu: Image>Calculations. In the Calculations window, select the V image layer as Source 1, and the I image layer as Source 2. In the 'Blending' sub-menu, select 'Add' and set the Scale to 2. In the 'Result' sub-menu select 'New Document,' then hit 'OK'. This will create a new file that contains an image where each pixel has the mean value between the V and I images. This new file can be copied into the file that contains the V and I layers. After putting the layers of this file into the order V, Mean, and I they are ready to be colorized using ESA's Colour Composite automated "action." The myriad other image adjustment procedures in Photoshop can be used to optimize the results from this, but usually the most important step is at the beginning when the file is loaded into Photoshop with FITS Liberator. The brightness controls in FITS Liberator are sensitive and it is important that the adjustments made to the images are applied evenly across both the V and I images. If they are not adjusted properly the image will end up looking either too red or too blue. It may be necessary to go through the entire process of loading the images and creating the composite several times before finding an acceptable result.

When an acceptable color image has been found the results should be saved in 'JPEG' format. This option can be accessed through the File menu with"Save for Web...". This pulls up a window that shows a preview image as well as several options. Select 'JPEG' for the file format and 'Maximum' for the quality, and save the result, and if ready for publication the name should be e.g. Galaxy_color.jpg.WEB. This will save a very large image ($\sim 4000 \times 4000$ pixels for ACS) that is cumbersome for normal web browsing. Therefore, it is useful to save a smaller preview version that is 600 pixels on a side and that will displayed by default on the galaxy's webpage and that will link to the full-size version. There is an image resizing option in the "Save for Web..." window, or it is possible to use 'convert -resize' from the command line. The preview image should be named, e.g. Galaxy_color600.jpg.WEB.

X-Y Plots

On occasion it can be useful to examine how the HSTPHOT/DOLPHOT detections are distributed spatially on the camera chip. Some reasons for this were given in Section A.4.3. These include masking out crowded regions in massive galaxies, and at the low-mass end excluding field stars that

may cause confusion in the CMD. This process can be taken a step farther for these sparse galaxies by encoding color information on the X-Y plots. It is simple to write a script that plots the pixel coordinates of detections that have colors e.g.: 1.0< $F606W - F814W$ <1.5. In extreme cases where the density of detections within a dwarf galaxy is only marginally higher than the background/field then focusing on stars that have, for example, RGB-like colors can help isolate the galaxy. This technique has only been necessary in a few limited cases, notably the WFPC2 survey of M81 dwarfs (Prog. 11126, PI: Chiboucas), but when it is, we include a plot of red dots in signfying detections in this color range over black points representing the other detections.

References

Dolphin, A. E. 2000, PASP, 112, 1397

Holtzman, J. A., Burrows, C. J., Casertano, S., Hester, J. J., Trauger, J. T., Watson, A. M., Worthey, G. 1995, PASP, 107, 1065

Makarov, D., Makarova, L., Rizzi, L., Tully, R. B., Dolphin, A. E., Sakai, S., Shaya, E. J. 2006, AJ, 132, 2729

Rizzi, L., Tully, R. B., Makarov, D., Makarova, L., Dolphin, A. E., Sakai, S., Shaya, E. J. 2007, ApJ, 661, 815

Schlegel, D. J., Finkbeiner, D. P., Davis, M. 1998, ApJ, 500, 525

Sirianni, M. et al. 2005, PASP, 117, 1049